

# Ion Acceleration in the Laser Transparency Regime

vorgelegt von  
Dipl.-Phys. Sven Steinke

Von der Fakultät II - Mathematik und Naturwissenschaften -  
der Technischen Universität Berlin  
zur Erlangung des akademischen Grades

Doktor der Naturwissenschaften  
- Dr. rer. nat. -

genehmigte Dissertation

Promotionsausschuss:

Vorsitzende: Prof. Dr. B. Kanngießer

Berichter: Prof. Dr. W. Sandner

Berichter: Prof. Dr. O. Willi

Tag der wissenschaftlichen Aussprache: 06.12.2010

Berlin 2010

D 83

For Kassian.

# Abstract

In this work novel, approved approaches for the acceleration of ions by short, intense laser pulse are investigated and characterized. The applied laser pulses with relativistic intensities and ultra-high temporal contrast enabled the application of foil targets with thicknesses below the collisionless skin depth of the laser ( nm) and hence the first experiments in the laser transparency regime.

In contrast to opaque, thick foils these targets allow the participation of all electrons in the focal volume in the acceleration and a group velocity matching of laser field, electrons and ions. The presented results expand the known picture of Target Normal Sheath Acceleration (TNSA) where the energy of the laser pulse is transferred to kinetic energy of plasma electrons at front side of an opaque, solid target. These "hot electrons" expand throughout the target and induce a quasi-static electric field at the rear side that in turn accelerates the ions. The conversion efficiency of this process is very low due to the high reflectivity of the laser and the lateral spreading of the electrons - typically 1%. Additionally, the spectral shape of the accelerated ions exhibits an exponential slope.

With the help of a Double-Plasma-Mirror (DPM) the temporal contrast of the laser pulse could be enhanced by approximately 4 orders of magnitude, without any distortion of the wave front. In the first place, the DPM allowed the deployment of nm-thin foils. An energy throughput of the system of 60 – 65 % was obtained. Diamond-like-Carbon (DLC) foils with thicknesses down to 2nm were used as targets. They were illuminated with linear polarized laser pulses at normal incidence and an optimum thickness for ion acceleration of 5.3 nm was demonstrated. At this optimum thickness, the proton energy was enhanced by a factor of two (13 MeV) and in case of carbon ions by a factor of 20 (71 MeV) compared to experiments with similar laser parameters, accompanied by a significant enhancement of the conversion efficiency up to values of about 10 %.

The existence of such an optimum is attributed to a pressure unbalance of the ponderomotive force of the laser and the restoring electrostatic force raised by the ions remaining at rest. If the ponderomotive exceeds the electrostatic force, the electrons are expelled from the sphere of influence of the ions and hence the ion acceleration is less effective. In case of thicker targets, the ponderomotive force

is not sufficient to exert the maximum polarization between electrons and ions. However the spectral shape of the ions was still exponential as in imprint of the exponential distribution of the hot electrons.

Consequently, in the following circular polarization was used to suppress  $(v \times B)$  - heating as the dominant laser absorption process. According to that, the plasma electrons are compressed and can be regarded as a mirror that gains more energy in favor of less momentum if accelerated. Then the ion acceleration occurs in a co-moving electrical field and intrinsically leads to a mono-energetic spectrum. This dominant acceleration by the laser radiation pressure could be experimentally demonstrated for the first time. The number and energy of accelerated electrons could be reduced and a distinct peak in the carbon spectrum was obtained centered around 30 MeV.

Furthermore, the harmonic radiation of the incident laser was measured giving a detailed insight into the plasma dynamics during the acceleration. This allowed the determination of the instantaneous plasma density by the spectral cut-off the harmonics which could be ascribed to one dimensional plasma expansion.

# List of Publications

Parts of this work have been published in the following references:

- P. V. Nickles, M. Schnuerer, **S. Steinke**, T. Sokollik, S. Ter-Avetisyan, W. Sandner, T. Nakamura, M. Mima, and A. Andreev. Prospects for ultrafast lasers in ion-radiography. *AIP Conference Proceedings*, **1024**, 183 (2008).
- A. A. Andreev, **S. Steinke**, T. Sokollik, M. Schnuerer, S. Ter Avetsiyan, K. Y. Platonov, and P. V. Nickles. Optimal ion acceleration from ultrathin foils irradiated by a profiled laser pulse of relativistic intensity. *Physics of Plasmas*, **16**, 013103 (2009).
- T. Sokollik, M. Schnuerer, S. Ter-Avetisyan, **S. Steinke**, P. V. Nickles, W. Sandner, M. Amin, T. Toncian, O. Willi, and A. A. Andreev. Proton imaging of laser irradiated foils and mass-limited targets. *AIP Conference Proceedings*, **1153**, 364 (2009).
- T. Sokollik, M. Schnuerer, **S. Steinke**, P. V. Nickles, W. Sandner, M. Amin, T. Toncian, O. Willi, and A. A. Andreev. Directional laser-driven ion acceleration from microspheres. *Physical Review Letters*, **103**, 135003 (2009).
- A. Henig, **S. Steinke**, M. Schnuerer, T. Sokollik, R. Hoerlein, D. Kiefer, D. Jung, J. Schreiber, B. M. Hegelich, X. Q. Yan, J. Meyer-ter Vehn, T. Tajima, P. V. Nickles, W. Sandner, and D. Habs. Radiation-pressure acceleration of ion beams driven by circularly polarized laser pulses. *Physical Review Letters*, **103**, 245003 (2009).
- P. V. Nickles, M. Schnuerer, **S. Steinke**, T. Sokollik, S. Ter-Avetisyan, A. Andreev, and W. Sandner. Generation and manipulation of proton beams by ultra-short laser pulses. *AIP Conference Proceedings*, **1153**, 140 (2009).
- S. Ter-Avetisyan, B. Ramakrishna, D. Doria, G. Sarri, M. Zepf, M. Borghesi, L. Ehrentraut, H. Stiel, **S. Steinke**, G. Priebe, M. Schnuerer, P. V. Nickles,

and W. Sandner. Complementary ion and extreme ultra-violet spectrometer for laser-plasma diagnosis. *Review of Scientific Instruments*, **80**, 103302 (2009).

- **S. Steinke**, A. Henig, M. Schnuerer, T. Sokollik, P. V. Nickles, D. Jung, D. Kiefer, R. Hoerlein, J. Schreiber, T. Tajima, X. Q. Yan, M. Hegelich, J. Meyer-ter Vehn, W. Sandner, and D. Habs. Efficient ion acceleration by collective laser-driven electron dynamics with ultra-thin foil targets. *Laser and Particle Beams*, **28**, 215 (2010).
- S. Pfotenhauer, O. Jaeckel, J. Polz, **S. Steinke**, H. P. Schlenvoigt, J. Heymann, A. P. L. Robinson, and M. Kaluza. A cascaded laser acceleration scheme for the generation of spectrally controlled proton beams. *New Journal of Physics*, 12(10):103009, 2010.
- M. Schnuerer, T. Sokollik, **S. Steinke**, P. V. Nickles, W. Sandner, T. Toncian, M. Amin, O. Willi, and A. A. Andreev. Influence of ambient plasmas to the field dynamics of laser driven mass-limited targets. *AIP Conference Proceedings*, **1209**, 111 (2010).
- B. Ramakrishna, M. Murakami, M. Borghesi, L. Ehrentraut, P. V. Nickles, M. Schnurer, **S. Steinke**, J. Psikal, V. Tikhonchuk, and S. Ter-Avetisyan. Laser-driven quasimonoenergetic proton burst from water spray target. *Physics of Plasmas*, **17**, 083113 (2010).
- B. Ramakrishna, A. Andreev, M. Borghesi, D. Doria, G. Sarri, L. Ehrentraut, P. V. Nickles, W. Sandner, M. Schnurer, **S. Steinke**, and S. Ter-Avetisyan. Observation of quasi mono-energetic protons in laser spray-target interaction. *AIP Conference Proceedings*, **1209**, 99 (2010).
- T. Sokollik, T. Paasch-Colberg, K. Gorling, U. Eichmann, M. Schnuerer, **S. Steinke**, P. V. Nickles, A. A. Andreev, and W. Sandner. Laser-driven ion acceleration using isolated mass-limited spheres. *New Journal of Physics*, **12**, 113013, (2010).
- A. A. Andreev, **S. Steinke**, M. Schnuerer, A. Henig, P. V. Nickles, K. Platonov, T. Sokollik, and W. Sandner. Hybrid ion acceleration with ultra-thin composite foils irradiated by high intensity circularly-polarized laser light. *Physics of Plasmas*, **17**, 123111 (2010).
- R. Hoerlein, **S. Steinke**, A. Henig, S. Rykovanov, M. Schnuerer, T. Sokollik, D. Kiefer, D. Jung, T. Tajima, J. Schreiber, B. M. Hegelich, P. V. Nickles,

M. Zepf, G. D. Tsakiris, W. Sandner, and D. Habs. Dynamics of nanometer-scale foil targets irradiated with relativistically intense laser pulses. *submitted*.

- M. Schnuerer, A. A. Andreev, **S. Steinke**, T. Sokollik, T. Paasch-Colberg, P. V. Nickles, A. Henig, D. Kiefer, D. Jung, R. Hoerlein, J. Schreiber, T. Tajima, D. Habs and W. Sandner. Optimization of electron density distribution for laser driven ion acceleration. *submitted*.
- S. Ter-Avetisyan, B. Ramakrishna, M. Borghesi, D. Doria, L. Ehrentraut, A. A. Andreev, P. V. Nickles, G. Priebe, **S. Steinke**, M. Schnuerer, W. Sandner, and V. Tikhonchuk. Negative ion laser accelerator. *submitted*.
- **S. Steinke**, M. Schnuerer, T. Sokollik, A. A. Andreev, P. V. Nickles, A. Henig, R. Hoerlein, D. Kiefer, D. Jung, J. Schreiber, T. Tajima, B. M. Hegelich, D. Habs, and W. Sandner. Optimization of laser-generated ion beams. *submitted*.





# Contents

<b>Introduction</b>	<b>1</b>
<b>I Basics</b>	<b>5</b>
<b>1 Interaction of Relativistic Laser Pulses with a Free Electron</b>	<b>7</b>
<b>2 Laser Plasma Interactions</b>	<b>11</b>
2.1 Light Propagation in Plasma . . . . .	11
2.2 Ponderomotive Force . . . . .	12
2.3 Laser Absorption in a Plasma . . . . .	14
2.3.1 Resonance Absorption . . . . .	15
2.3.2 Brunel Absorption . . . . .	16
2.3.3 Hole Boring . . . . .	16
2.3.4 Relativistic $j \times B$ Heating . . . . .	17
<b>3 Laser-Driven Ion Acceleration</b>	<b>19</b>
3.1 Target Normal Sheath Acceleration (TNSA) . . . . .	20
3.2 Radiation Pressure Ion Acceleration . . . . .	22
3.2.1 Initial Stage . . . . .	23
3.2.2 Light Sail Stage . . . . .	26
<b>4 Surface High Harmonic Generation by Coherent Wake Emission</b>	<b>31</b>
<b>II Hardware</b>	<b>33</b>
<b>5 Laser System</b>	<b>35</b>
5.1 Ti:Sapphire High-Field Laser . . . . .	36
5.2 Laser Pulse Characterization . . . . .	37
5.2.1 Spectral Phase Interferometry for Direct Electric-Field Re- construction . . . . .	37

5.2.2	Scanning 3rd order Cross-Correlation . . . . .	40
5.3	Double Plasma Mirror . . . . .	42
<b>6</b>	<b>Diagnostics</b>	<b>47</b>
6.1	Thomson Spectrometer . . . . .	48
6.2	XUV-Spectrometer . . . . .	50
<b>III</b>	<b>Experiments</b>	<b>53</b>
<b>7</b>	<b>Ion Acceleration with linearly polarized Laser Pulses</b>	<b>55</b>
7.1	Experimental Setup . . . . .	55
7.2	Transition from TNSA to Enhanced TNSA . . . . .	57
7.3	Nonlinear Laser Pulse Transmission of a Thin Plasma Layer . . . . .	58
7.4	Maximum Ion Energies and Spectral Shape . . . . .	59
7.5	Conversion Efficiency . . . . .	61
7.6	Simulation . . . . .	62
7.7	Summary and Discussion . . . . .	64
<b>8</b>	<b>Ion Acceleration in the Radiation Pressure Dominated Regime</b>	<b>67</b>
8.1	Experimental Setup . . . . .	67
8.2	Maximum Ion Energies and Spectral Shape . . . . .	68
8.3	Simulations . . . . .	69
8.4	Summary and Discussion . . . . .	71
<b>9</b>	<b>High-Harmonic Generation in Ultra-Thin Foils</b>	<b>73</b>
9.1	Experimental Setup . . . . .	74
9.2	Dynamics of Nanometer-Scale Foil Targets . . . . .	74
9.3	Simulations . . . . .	77
9.4	Summary and Discussion . . . . .	78
	<b>Summary and Outlook</b>	<b>81</b>
	<b>List of Figures</b>	<b>86</b>
	<b>Bibliography</b>	<b>99</b>
	<b>Acknowledgments</b>	<b>101</b>

# Introduction

Beginning with the first experimental realization of the laser in 1960 [1] an enormous scientific activity with the intention of enhancing the power of the laser was initialized. Particularly the approach of *Chirped Pulse Amplification* in 1985 [2] has led to a continuous raise of the laser peak intensity. In a singular case values for the intensity of  $10^{22}$  W/cm<sup>2</sup> have been published [3]. At the same time, the laser pulse duration has been decreased to a few femtoseconds. The interaction of such laser pulses with matter immediately creates hot-dense plasmas which at intensities above  $10^{18}$  W/cm<sup>2</sup> are characterized by relativistic velocities of the plasma electrons accelerated in the laser field.

In contrast to conventional accelerators where the accelerating electric fields are limited to few tens of MeV/m which constrains the highest energy achievable to  $\sim 1$  PeV when the acceleration length is given by the equator circumference, plasma acceleration does not suffer from this confinement. Already in 1956, the use of *collective fields* [4,5] provided by temporary electron-ion separation in longitudinal plasma waves [6] has been suggested. These fields can principally exceed those of conventional accelerators by four orders of magnitude. The possibility to excite such plasma waves efficiently with high intensity laser pulses has led to the proposal of the *Laser Electron Accelerator* in 1976 [7]. Experimentally, quasi-monoenergetic electron bunches with energies of  $\sim 1$  GeV have been demonstrated in 2006 [8] with an effective acceleration length on the order of cm.

The current laser-induced acceleration of ions, on the other hand is a secondary process since the required intensity for a direct acceleration of protons in the laser field ( $5 \times 10^{24}$  W/cm<sup>2</sup>) exceeds the ones currently available. Thus, electrons, directly accelerated by the laser field in a plasma are charge separated from the ions and cause strong electrical fields which in turn accelerate the ions. These fields reach field strengths of  $\sim 10^{12}$  V/m which is on the same order as the electric field of the laser itself. The resulting ion spectra exhibit a Maxwellian shape and a sharp cut-off with energies up to 58 MeV [9] where a laser intensity of  $\sim 10^{20}$  W/cm<sup>2</sup> and an acceleration length of only a few  $\mu$ m were used.

These beams have intrinsic qualities that distinguish them from beams produced by conventional accelerators, as there are very high laminarity ( $\sim 0.003$  mm

mrads), an ultra-short duration (ps) when they are emitted and a high particle number per bunch ( $\sim 10^{11}$ ).

The unique qualities of the laser induced particle beams offer a high potential for future applications: time and space resolved radiography of dense matter, injection into conventional accelerators, medical applications (e.g. cancer therapy), ion beam physics, spallation or transmutation. Moreover, they can be combined with other laser generated radiation sources (e.g. electrons or high-order harmonics) to realize pump-probe experiments.

In fact, the ion beam parameters are up to now deviant from those required for the mentioned applications and thus, further investigations are needed to increase the maximum energy and at the same time to narrow the energy spectrum to a monoenergetic shape. In principal, two approaches are conceivable: To vary the laser parameters and/or to change the target. These changes are then aiming at changes of the principal acceleration process itself.

In this thesis novel, improved ion acceleration schemes are explored by combining an advanced concept of laser contrast enhancement - the Plasma Mirror with a target system consisting of free-standing *Diamond-Like-Carbon* (DLC) foils with thicknesses below the skin depth of the laser, i.e. a few nanometers, developed by collaboration partners within the Transregio SFB TR18 at the Ludwig-Maximilians-Universität München (LMU). This combination denotes the first experimental demonstration of *Ion Acceleration in the Laser Transparency Regime* for macroscopic extended targets.

The thesis is structured as follows:

- Chapter 1 introduces the most important properties of relativistic laser pulses and gives a description of their interaction with a free electron.
- Chapter 2 gives an overview of the physics being relevant for laser-plasma interaction at relativistic intensities. Based on the description of the propagation of the laser pulses in a plasma, several mechanisms of laser energy transfer to plasma electrons are presented.
- Chapter 3 provides a detailed description of several ion acceleration scenarios being relevant for this thesis.
- Chapter 4 presents the basics of high harmonic generation from solid density targets.
- Chapter 5 introduces the MBI High-Field Laser that was used for the experiments. Here, the laser pulse is characterized in terms of pulse length and temporal contrast. Additionally, the Double-Plasma Mirror System developed within this thesis for contrast enhancement is introduced and characterized.

- Chapter 6 deals with the main diagnostics used to characterize the accelerated ion beams and the high harmonic radiation.
- Chapter 7 presents different interaction experiments of ultra-high contrast laser pulses with DLC and Titanium foils of thicknesses ranging from 2.9 nm to 5  $\mu\text{m}$ . The main focus lies on the ion acceleration, where the main property of the transition from TNSA to enhanced TNSA as the dominant acceleration mechanism, namely the symmetric acceleration to both sides of the foil was revealed for the first time and finally, first signatures of a direct participation of the laser radiation pressure were found. Furthermore, the transmittance of the DLC foils was quantified and the spectral properties of the transmitted laser pulse were analyzed. Parts of the results presented in this chapter have been published in [10].
- Chapter 8 presents experimental results on ion acceleration where the influence of the laser radiation pressure was emphasized by changing the laser polarization from linear to circular. Thereby, the distribution function of the electron is modified due to the absence of the longitudinally oscillating component of the Lorentz force (for simplicity in the following referred to as suppression of electron heating) what results in an ballistic acceleration of the whole target foil in the focal volume as a quasi-neutral plasma bunch if target thickness and density were chosen such that the radiation pressure on the plasma electrons equals the restoring force given by the charge separation. Two-dimensional particle-in-cell simulations (by X. Q. Yan<sup>1,2</sup>) revealed that the carbon ions are for the first time dominantly accelerated by the laser radiation pressure. The results have been published in [11].
- Chapter 9 presents experimental results of high harmonic radiation generated at the DLC targets under normal incidence. The measured harmonic spectra allow the extraction of the target density in the same scenario which was used for the ion acceleration in Chapters 7+8. With the help of two-dimensional particle-in-cell simulations the first experimental observation of predominantly odd-numbered harmonics could be addressed to a relativistic generation by the longitudinally oscillating component of the Lorentz force. Parts of these results have been submitted for publication [12].
- Chapter 10 summarizes this work and gives perspectives for future experiments on the basis of the findings of this work.

---

<sup>1</sup>Max-Planck-Institut für Quantenoptik, 85748 Garching, Germany

<sup>2</sup>State Key Lab of Nuclear Physics and Technology, Peking University, 100871 Beijing, China



Part I

Basics





# Chapter 1

## Interaction of Relativistic Laser Pulses with a Free Electron

The electric and magnetic fields  $\mathbf{E}$  and  $\mathbf{B}$  of electromagnetic waves can be derived from Maxwells equations and written using a vector potential  $\mathbf{A}$  [13] as:

$$\mathbf{E} = -\frac{\partial}{\partial t}\mathbf{A}, \quad (1.1)$$

$$\mathbf{B} = \nabla \times \mathbf{A}. \quad (1.2)$$

An elliptically polarized plane wave in vacuum propagating along the x-direction can then be expressed by:

$$\mathbf{A} = (0, \delta A_0 \cos(\phi), (1 - \delta^2)^{1/2} A_0 \sin(\phi)), \quad (1.3)$$

where  $\phi = \omega t - kx$  with the frequency  $\omega$ , the wave number  $k$  and  $\delta$ , a polarization parameter such as  $\delta = \{\pm 1, 0\}$  for linear and  $\delta = \pm 1/\sqrt{2}$  for circular polarization. Then, the electric field can be calculated immediately for linear and respectively circular polarization:

$$\mathbf{E}_{lin} = \omega E_0 \sin(\omega t - kx) \mathbf{e}_y, \quad (1.4)$$

$$\mathbf{E}_{circ} = \frac{\omega E_0}{\sqrt{2}} (\sin(\omega t - kx) \mathbf{e}_y - \cos(\omega t - kx) \mathbf{e}_z). \quad (1.5)$$

The relation of the amplitudes  $A_0$  and  $E_0$  can be obtained from Eq. 1.1 and 1.2 and is  $A_0 \omega = E_0$ . The vacuum intensity  $I$  of a monochromatic wave is given by the cycle-averaged magnitude of the Poynting Vector  $\mathbf{S}$  and is identical for linear and circular polarization:

$$I = \overline{|\mathbf{S}|} = \frac{c}{4\pi} |\mathbf{E}|^2 = \frac{1}{2} \epsilon_0 c E_0^2, \quad (1.6)$$

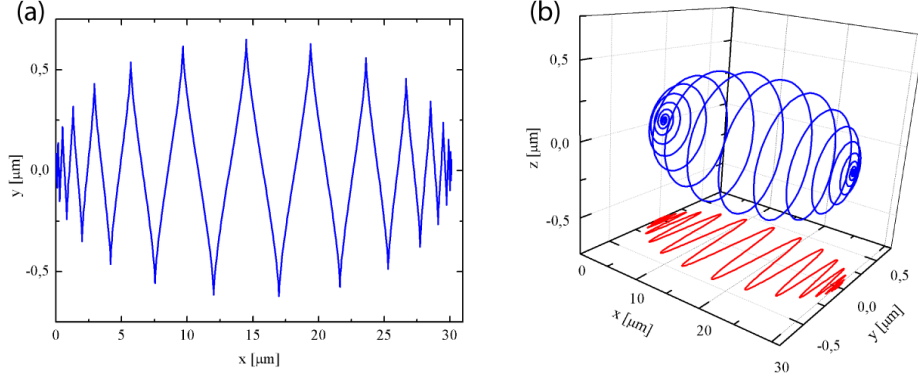


Figure 1.1: *Electron trajectory in case of (a) linear and (b) circular polarization of the incident laser pulse, propagating in  $x$ -direction with a pulse duration of  $\tau = 15fs$  and  $a_0 = 5$ . The net energy gain of the electron is zero in both cases, it is only displaced in laser pulse propagation direction.*

with the vacuum permittivity  $\epsilon_0$  and the speed of light in vacuum  $c$ .

In the following, the interaction of an electromagnetic plane wave with a single electron is discussed. It is assumed that:

1. the laser field is in vacuum with no walls or boundaries present,
2. no static electric or magnetic fields are present,
3. the transversal region of interaction is infinite.

The motion of a single electron in an electromagnetic field is described by the Lorentz equation [14]:

$$\frac{d\mathbf{p}}{dt} = \frac{d(\gamma m_e \mathbf{v})}{dt} = -e(\mathbf{E} + \mathbf{v} \times \mathbf{B}), \quad (1.7)$$

with the relativistic factor

$$\gamma = \frac{1}{1 - v^2/c^2} = \sqrt{\frac{1 + p^2}{m^2 c^2}}. \quad (1.8)$$

For non-relativistic electrons ( $v/c \ll 1$ ) the  $(\mathbf{v} \times \mathbf{B})$ -term can be neglected and the maximum oscillation velocity of the electron  $v_0$  is used to define the normalized amplitude  $a_0$ :

$$a_0 = \frac{v_0}{c} = \frac{eE_0}{m_e \omega c} \quad (1.9)$$

which can be rewritten using Eq. 1.6 as

$$I\lambda^2 = 2\pi^2 a_0^2 \frac{\epsilon_0 m_e^2 c^5}{e^2} \approx a_0^2 \cdot 1.37 \times 10^{18} \quad [\text{W}/\text{cm}^2 \cdot \mu\text{m}^2]. \quad (1.10)$$

The fully relativistic equation of motion of the electron can now be obtained by substituting Eq. (1.1) and (1.2) in Eq. (1.7):

$$\frac{d\mathbf{p}}{dt} = e \left( \frac{\partial \mathbf{A}}{\partial t} - \mathbf{v} \times (\nabla \times \mathbf{A}) \right). \quad (1.11)$$

Following the derivation of [14] the trajectories in the laboratory frame are:

$$\begin{aligned} x &= \frac{ca_0^2}{4\omega} \left( \phi + \frac{2\delta^2 - 1}{2} \sin(2\phi) \right), \\ y &= \frac{\delta ca_0}{\omega} \sin(\phi), \\ z &= \frac{-(1 - \delta^2)^{1/2} ca_0}{\omega} \cos(\phi). \end{aligned} \quad (1.12)$$

It has to be denoted that the longitudinal (x) component has (i) a quadratic dependence on  $a_0$  compared to the transversal (y, z) which only shows a linear dependence and (ii) regardless of polarization, a component which will force the electron to drift with an laser-cycle-averaged velocity:

$$v_D = \frac{\bar{x}}{t} = \frac{a_0^2}{4 + a_0^2}, \quad (1.13)$$

where  $\bar{x}$  is the cycle-average of  $x$  (Eq. 1.12). In Fig. 1.1 trajectories for an electron being initially at rest are plotted in case of an interaction with a laser pulse of finite duration and a Gaussian envelope. Since the electron is at rest again after the interaction, its net energy gain by interaction with the electromagnetic field is zero, it has only been displaced in direction of laser pulse propagation.

However, most significant for the experiments described in this thesis is the fact that in case of circular polarization the electron does not exhibit an oscillating motion in longitudinal direction as it does for linear polarization.

In order to directly accelerate an electron by an electromagnetic wave at least one of the assumption (1-3) has to be violated. This violation is given in the present experiments since the radius of the focal plane is in the order of the electrons transversal deflection (Ch. 2.2 and Fig. 1.1).



# Chapter 2

## Laser Plasma Interactions

In this chapter the interaction of laser light with a plasma is described. In contrast to Chapter 1.1 where the interaction with a single electron was discussed, the collisionless plasma consisting of a cold electron gas ( $T_e = 0$ ) with a stationary ion background is described based on a hydrodynamic theory without inherent magnetic fields.

### 2.1 Light Propagation in Plasma

If a laser pulse interacts with such a plasma, electrons will be slightly displaced while the ions rest. This charge separation creates an uniform electric field and causes a restoring force. The resonance frequency of the resulting oscillation is known as the plasma frequency  $\omega_p$ :

$$\omega_p = \sqrt{\frac{n_e e^2}{\epsilon_0 \bar{\gamma} m_e}}, \quad (2.1)$$

where  $\bar{\gamma}$  represents the cycle averaged mass increase of the electron [15]:

$$\bar{\gamma} = \sqrt{1 + \frac{a_0^2}{2}}. \quad (2.2)$$

With the help of the dispersion relation for electromagnetic waves in plasma [16]:

$$\omega^2 = \omega_p^2 + c^2 k^2, \quad k^2 = \frac{\omega^2 \epsilon}{c^2}, \quad (2.3)$$

where the dielectric function of the plasma  $\epsilon$  is related to the complex refraction index by  $n_R = \sqrt{\epsilon}$ , it becomes obvious that  $\omega_p$  divides the properties of the plasma into transparent (underdense) if  $\omega < \omega_p$  and opaque (overdense) if  $\omega > \omega_p$ : The wave vector  $k$  becomes imaginary if  $\omega/\omega_p < 1$  and hence electric- and magnetic

field decay exponentially. An evanescent component will anyhow penetrate into the overdense region up to a characteristic length, the collisionless skin depth  $l_s$ :

$$l_s = \frac{c}{\omega_p}. \quad (2.4)$$

For the transition between dispersion and absorption where  $\omega = \omega_p$ , the critical density  $n_c$  can be defined. Using Eq. (2.1) and Eq. (2.3) this critical density is given by

$$n_c = \frac{\bar{\gamma}\epsilon_0 m_e \omega^2}{e^2} \approx 1.1 \times \bar{\gamma} \times 10^{21} \left[ \frac{\lambda_L}{\mu m} \right]^{-2} \text{ cm}^{-3}. \quad (2.5)$$

By using this definition the intensity (Eq. 1.10) can be further simplified to:

$$I = \frac{1}{2} m_e a_0^2 c^3 n_c. \quad (2.6)$$

Finally, the refraction index can be calculated:

$$n_R = \sqrt{1 - \frac{\omega_p^2}{\omega^2}} = \sqrt{1 - \frac{n_e}{n_c}}. \quad (2.7)$$

The value for the critical density is  $\approx 2.5$ -orders of magnitude below the typical solid density. Therefore, it is possible that the incident laser radiation will be reflected from such an overdense (overcritical) plasma surface. It is important that an incident laser pulse with a temporal profile (e.g. Gaussian) will not be reflected totally. Since the target will be ionized and the plasma begins to expand into vacuum, the main part of the laser pulse will interact with a partly underdense plasma density gradient where different interaction/ absorption mechanisms take place Ch. 2.3.

But since the plasma frequency in the relativistic case ( $\bar{\gamma} > 1$ ) is becoming dependent on the laser intensity and a focal plane of the laser with a Gaussian intensity distribution is assumed, the reflection index exhibits a spatial dependency which acts as a focussing optic. The effect is called *Relativistic Self Focussing* [17].

In fact, the principal of the laser reflection at an overdense surface is the key principal of the Plasma Mirror [18–21] as used for all the experiments presented in this thesis (Ch. 7-9) and of the generation of relativistic Harmonics [22–24].

## 2.2 Ponderomotive Force

The pressure of electromagnetic radiation incident on a sharp boundary (surface) is given by the radiation pressure  $p_L$ :

$$p_L = \frac{I}{c}(1 + n_R), \quad (2.8)$$

where  $n_R$  is the reflection coefficient and  $c$  the speed of light in vacuum. The ponderomotive force per unit volume is related to the gradient of the radiation pressure but Eq. 2.8 becomes meaningless in case of a laser propagating in an inhomogeneous plasma, since the electromagnetic field cannot be calculated only from the knowledge of  $I$  and therefore the light pressure is not known [16]. The electromagnetic fields in the plasma have to be known in order to calculate the ponderomotive force.

In case of an electron moving with non-relativistic velocity the  $\mathbf{v} \times \mathbf{B}$ -term in Eq. (1.7) is smaller compared to the  $\mathbf{E}$  term, the electron oscillates parallel to  $\mathbf{E}(\mathbf{r})$ . In first order at  $\mathbf{r} = \mathbf{r}_0$  this yields:

$$m_e \frac{d\mathbf{r}_1}{dt} + e\mathbf{E}(\mathbf{r}_0) \cos \phi = 0, \quad (2.9)$$

then the solution is the displacement of the electron

$$\mathbf{r}_1 = \frac{e\mathbf{E}(\mathbf{r}_0) \cos \phi}{m_e \omega^2}. \quad (2.10)$$

For the second order has to be considered that

$$\mathbf{E}(\mathbf{r}) = \mathbf{E}(\mathbf{r}_0) + (\mathbf{r}_1 \cdot \nabla) \mathbf{E}(\mathbf{r}_0), \quad (2.11)$$

and for the velocity  $d\mathbf{r}/dt = \mathbf{v} = \mathbf{v}_1 + \mathbf{v}_2$  and the magnetic field  $\mathbf{B}(\mathbf{r}) = \mathbf{B}(\mathbf{r}_0)$ . Substituting Eq. (2.9) and Eq. (2.11) into Eq. (1.7) results in the second order equation of motion:

$$m_e \frac{d\mathbf{v}_2}{dt} = -e \left[ (\mathbf{r}_1 \cdot \nabla) \mathbf{E}(\mathbf{r}_0) \cos \phi + \frac{\mathbf{v}_1 \times \mathbf{B}(\mathbf{r}_0) \sin \phi}{c} \right]. \quad (2.12)$$

Using Eq. (1.7), (2.10) into (2.12) and averaging the corresponding force over one laser cycle leads to the ponderomotive force:

$$\begin{aligned} \mathbf{f}_P &= -\frac{e^2}{2m_e \omega^2} [(\mathbf{E}(\mathbf{r}) \times \nabla) \mathbf{E}(\mathbf{r}) + \mathbf{E}(\mathbf{r}) \times (\nabla \times \mathbf{E}(\mathbf{r}))] \\ &\stackrel{1}{=} -\frac{e^2}{4m_e \omega^2} \nabla E^2(\mathbf{r}). \end{aligned} \quad (2.13)$$

---

<sup>1</sup>using:  $\mathbf{E} \times (\nabla \times \mathbf{E}) = (\nabla \mathbf{E}) \cdot \mathbf{E} - (\mathbf{E} \cdot \nabla) \mathbf{E} = \frac{1}{2} \nabla \cdot \mathbf{E}^2 - (\mathbf{E} \cdot \nabla) \mathbf{E}$

Thus, the ponderomotive force in the non-relativistic case is proportional to the gradient of  $E^2$  and electrons will be pushed out of the region with higher intensities. The fully relativistic description delivers an additional factor  $(1/\gamma)$  [25]:

$$\mathbf{f}_{P,rel} = -\frac{e^2}{4m_e\bar{\gamma}\omega^2}\nabla E^2(\mathbf{r}). \quad (2.14)$$

The ejection angle  $\theta$  of the electron from the focus with respect to the laser propagation axis is determined by the ratio of longitudinal and transversal momentum:

$$\tan \theta = \frac{p_y}{p_x} = \sqrt{\frac{2}{\gamma - 1}} \quad (2.15)$$

For free electrons in the laser focus the laser acts as an accelerator and a spectrometer, a fact which has been exploited experimentally at laser intensities of  $I = 10^{18} \text{ W/cm}^2$  [26].

## 2.3 Laser Absorption in a Plasma

As it has been discussed in Section 2.1 an intense laser pulse incident on an overdense plasma will be partly absorbed. At moderate laser intensities the electron absorbs a photon while colliding with an ion or another electron. The process is called *Collisional* or *Inverse Bremsstrahlung Absorption*.

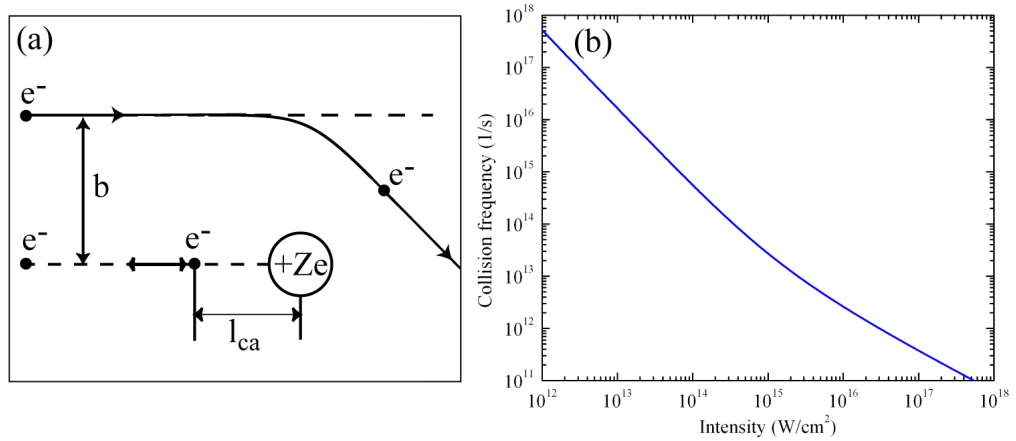


Figure 2.1: (a) *Classical Rutherford scattering of an electron colliding with an positive ion charge  $Ze$ .  $b$  is the impact parameter and  $l_{ca}$  is the closest approach for  $b = 0$ . In (b) Eq. 2.16 is plotted*



The electron-ion collision frequency  $\nu_{ei}$  is given by [27],

$$\nu_{ei} = \frac{4}{3} \frac{(2\pi)^{1/2} Z_i^2 e^4 n_i \ln(\Lambda)}{(k_B T_e)^{3/2} m_e^{1/2}} \simeq 2.91 \times 10^{-6} \frac{Z_i^2 n_i \ln(\Lambda)}{T_e (\text{eV})^{3/2}} [\text{s}^{-1}], \quad (2.16)$$

with the ion density  $n_i$ , the degree of ionization  $Z_i$ , the electron temperature  $T_e$  and the Coulomb logarithm  $\ln(\Lambda) = b_{\max}/b_{\min}$ , where  $b_{\max}$  and  $b_{\min}$  are the maximum, respectively minimum of the impact parameter  $b$ . In Fig. 2.1a the scattering process for a single electron is sketched. In case of a plasma, the very distant interactions are screened by the surrounding charged particles, so that there is a finite value for the interaction range  $b_{\max} = \lambda_D$ . The minimum distance  $b_{\min}$  is given by the classical distance of closest approach  $b_{\min} = l_{ca}$  (Fig. 2.1b), so that

$$\Lambda = \frac{\lambda_D}{l_{ca}} = \frac{9N_D}{Z_i}, \quad (2.17)$$

where  $N_D = (4\pi\lambda_D^3 n_e)/3$  is the number of particles in a Debye sphere.

Since the mean electron temperature is given by the Ponderomotive potential (Eq. 3.1) the collision frequency can be expressed as a function of the laser intensity (Fig. 2.1b). If the effective time between electron-ion collisions  $\tau_{ei}$  is longer than the laser pulse duration  $t_p$

$$\tau_{ei} = 1/\nu_{ei} > t_p, \quad (2.18)$$

the interaction can be treated collisionless, because (i) collisions become increasingly ineffective for rising electron temperatures (Eq. 2.16) and (ii) the electron quiver velocity exceeds their thermal velocity and hence the collective motions are dominating the plasma kinematics [14]. This condition is fulfilled if a laser pulse with a duration of 45 fs and an intensity  $> 10^{15} \text{ W/cm}^2$  is interacting with solid density ( $n_i = 10^{23} \text{ cm}^{-3}$ ) plasma (Fig. 2.1b) and hence for all the experiments presented in this thesis.

For this reason the main collisionless absorption mechanism shall be sketched in the following sections.

### 2.3.1 Resonance Absorption

In case of a p-polarized laser pulse obliquely incident onto a plasma gradient, it is reflected at a density lower than the critical density:

$$n_e = n_c \cos^2 \theta, \quad (2.19)$$

where  $\theta$  is the angle of incidence. The electric field perpendicular to the target surface tunnels through the point of reflection to the critical density surface and

resonantly drives an electron plasma wave. The energy distribution of the accelerated electrons corresponds to the Boltzmann-distribution [28].

### 2.3.2 Brunel Absorption

If the amplitude of the oscillating electrons  $x_p$  which oscillate along the density gradient exceeds the plasma density scale length  $L$  the resonance breaks down. The amplitude of the oscillations is approximated by

$$x_p \simeq \frac{eE_0}{m_e\omega^2} = \frac{v_0}{\omega} \quad (2.20)$$

and abrogates if  $v_0/\omega > L$ . However, the electrons in the vicinity of a sharp vacuum-plasma interface can be accelerated into the vacuum during one laser half cycle and back when the field reverses. They cross the critical density surface and propagate into the overdense plasma, where they are out of the sphere of influence of the electric field and thus, gain energy [29].

### 2.3.3 Hole Boring

The surface of the critical density will be modulated by the Ponderomotive Force as discussed in Ch. 2.2. In case of a sharp plasma boundary the pressure of the incident electromagnetic radiation is given by the radiation pressure (Eq. 2.8), which causes *Hole Boring* into the overdense plasma surface. This results primarily from a pressure imbalance of the momentum flux of the ion flow into the target with the radiation pressure  $p_e \ll p_L$  [30], leading to the formation of an electrostatic shock wave travelling into the target with a constant velocity. The velocity can be estimated by the pressure balance:

$$n_i m_i v_i^2 = \frac{I}{c} (1 + n_R), \quad (2.21)$$

where  $n_i$ ,  $m_i$  and  $v_i$  are the ion number density, mass and velocity. Using momentum and number conservation [30] the velocity can be obtained by substituting the intensity according to Eq. 2.6:

$$\frac{v_i}{c} = \sqrt{\frac{Z m_e n_c (1 + n_R)}{2 m_i n_e}} a_0, \quad (2.22)$$

with the ion charge state  $Z$ . In case of the laser with  $a_0 = 5$  impinging on a target with  $n_e/n_c = 500$  this results in a velocity of  $0.02c$  and thus moving 244 nm in 45 fs. This effect was observed experimentally by the Doppler-shift of the reflected laser pulse [31].

### 2.3.4 Relativistic $j \times B$ Heating

Another mechanism whereby electrons are directly accelerated by the a laser field incident on a step-like density profile is called *Relativistic  $j \times B$  Heating*- originally pointed out by Kruer and Estabrook [32]. The main difference to *Brunel Absorption* is the driving term which is the  $\mathbf{v} \times \mathbf{B}$  component of the Lorentz force (Eq. 1.7) in this case. It oscillates longitudinally at twice the laser frequency  $\omega$ . A linearly polarized wave of the form of Eq. 1.4 gives rise to the longitudinal force:

$$F_x = -\frac{m}{4} \frac{\partial v_0^2(x)}{\partial x} (1 - \cos 2\omega t). \quad (2.23)$$

With the help of Eq. 1.9 the first term can be identified as the x-component of the Ponderomotive Force (Ch. 2.2) which pushes the electrons inwards the plasma density gradient (Ch. 2.3.3). The second component leads to heating of the electrons. This works for any polarization except for circular and is most effective for normal incidence together with relativistic quiver velocities of the electron, i.e.  $a_0 > 1$ .



## Chapter 3

# Laser-Driven Ion Acceleration

In this chapter the mechanisms of laser-driven ion acceleration which are relevant for this thesis will be discussed.

A direct acceleration of ions in a field of currently available laser systems is impossible due to their high mass. The average kinetic energy a charged particle with mass  $m$  can gain, is defined by the Ponderomotive Potential  $\Phi_p$  [14, 30]:

$$\Phi_p = mc^2(\gamma - 1) = mc^2 \left( \sqrt{1 + \frac{a_0^2}{1836^2}} - 1 \right). \quad (3.1)$$

This yields in case of protons  $\Phi_p \approx 3.5 \text{ keV}$  if  $a_0 = 5$  what is neglectable in context of multi- $\text{MeV}$  ion acceleration. At laser intensities of  $5 \times 10^{24} \text{ W/cm}^2$  ( $a_0 = 1836$ ) the ions finally reach relativistic velocities within one laser cycle and the acceleration process enters the so-called Piston Regime [33].

But the laser energy can be efficiently transferred to the plasma electrons by various mechanisms leading to different ion acceleration scenarios, depending on the experimental parameters e.g. intensity and temporal contrast of the laser pulse as well as target properties. Several mechanisms will be sketched in the following sections. An empirical scaling law has been obtained by Esirkepov *et al.* [34] in case of laser pulses with an ultra-high temporal contrast (i.e. a Gaussian pulse). They found by multiparametric PIC simulations that the maximum ion energy for a given laser intensity is reduced to a dependence on the normalized areal density  $\sigma$ :

$$\sigma = \pi \frac{n_e}{n_c} \frac{D}{\lambda_L}, \quad (3.2)$$

where  $D$  is the target thickness and  $\lambda_L$  the laser wave length. Then, the highest ion energy occurs at the optimum areal density  $\sigma_{opt}$ :

$$\sigma_{opt} \stackrel{!}{\approx} 3 + 0.4 \times a_0. \quad (3.3)$$

Besides the Piston Regime a radiation pressure dominated regime can be achieved at much lower intensities when the electron heating is suppressed (Ch. 2.3), e. g. by changing the polarization to circular and using normal incidence on the target [35]. Here, the maximum ion energy becomes proportional to the laser intensity. This regime is up to now the optimum achievable with the current laser systems in terms of the maximum ion energy, efficiency and the most promising one with regard to the scalability with the laser intensity.

Except those optimum conditions laser-driven ion acceleration is possible for a vast set of parameters. Here, the route towards the outlined optimum will be sketched, beginning with laser and target parameters deviant from those given in 3.3, the co-called *Target Normal Sheath Acceleration* (TNSA) up to a dominant Radiation Pressure Acceleration *RPA*.

### 3.1 Target Normal Sheath Acceleration (TNSA)

As well as other laser ion acceleration scenarios discussed here, TNSA is an indirect mechanism. The laser energy is transferred to kinetic energy of plasma electrons which in turn accelerate the ions.

Based on the TNSA scheme, firstly suggested by Wilks *et al.* [36] scaling laws were developed which describe the acceleration process as an isothermal expansion of an collisionless plasma [37, 38] and cover a broad range of parameters [39, 40]. Basically, the TNSA regime is distinguished from *Enhanced TNSA* (Ch. 3.1) by the temporal laser pulse contrast ratio, i. e. the relation between the intensity of the peak of the main pulse and the intensity of the pedestal 5.2.2. Since the inherent mechanism in TNSA is the laser pulse absorption in an underdense (below the critical density) plasma, the pedestal of the focussed laser pulse has to be intense enough ( $> 10^{12} \text{W/cm}^2$ ) to ionize the atoms at the front surface of the target and on the other hand weak enough to not destroy the target before the arrival of the main pulse. This confines the possible values of the contrast ratio to  $10^{-5} - 10^{-9}$  dependent on the peak intensity of the used laser system.

At the front side of the target, the pedestal of the laser pulse creates an underdense plasma and the main laser pulse then interacts with this pre-plasma which has an exponential density profile. The characteristic scale length in which the density drops from solid- to critical density is:  $L = c_s \tau_p$ , where  $c_s$  is the plasma sound speed and  $\tau_p$  the laser pulse duration.  $L$  is in the order of a few  $\mu\text{m}$ . The amount of laser energy transferred to the kinetic energy of the electrons  $\eta$  is estimated by an empirical scaling law:

$$\eta \approx a(I_L \lambda^2)^{3/4} \approx 1.68 \times 10^{-15} \times I_L^{3/4} \quad [\text{W}/\text{cm}^2], \quad (3.4)$$

and attains 10-50 % [9, 41–43].

The electrons are accelerated in direction of the density gradient of the pre-plasma while the ions are initially stationary. On their way through the target, the hot electrons are scattered at the cold target electrons or nuclei resulting in an opening angle of  $\theta \approx 1.3 \text{ sr}$  [43]. When leaving the target at the rear side, most of the electron are forced to turn around and re-enter the foil since their energy is not sufficient to escape their self-induced field. This leads to an equilibrium situation with a constant number of electrons outside of the foil.

$$\lambda_D = \sqrt{\frac{\epsilon_0 k_B T_e}{e^2 n_e}}, \quad (3.5)$$

with the hot electron temperature  $T_e$  which is usually estimated by the Ponderomotive Potential (Eq. 3.1). The electron density behind the target  $n_e$  can be estimated by the number of hot electrons given by the efficiency (Eq. 3.4) and the volume they occupy i.e. a cylinder spanned by Eq. 3.5 and the opening angle of the electron bunch. Then, the field strength is

$$F_0 \approx \frac{k_B T_e}{e \lambda_D}, \quad (3.6)$$

which is in the order of TV/m for a laser with an intensity in the order of  $10^{19} \text{ W}/\text{cm}^2$  and sufficient to immediately field ionize the atoms in the vicinity of the target rear side.

The actual ion acceleration process is modeled as isothermal expansion of the *capacitor system* sketched above, resulting in a spectrum with a Maxwellian shape and a sharp cut-off energy [37]

$$E_{max} \approx 2Zk_B T_e \left( \ln \frac{2\omega_{pi} t}{\sqrt{2e_E}} \right)^2, \quad (3.7)$$

with Euler's number  $e_E$  and the ion plasma frequency  $\omega_{pi} = \sqrt{Zn_{e0}e^2/\epsilon_0 m_i}$  where  $Zn_e$  is the initial ion density and  $m_i$  the ion mass. The acceleration time  $t$  is in the order of the laser pulse duration  $\tau_L$ . Fuchs *et al.* [39] found the best fit to the experimental data, with  $t \approx 1.3\tau_L$ .

The first experimental demonstrations [9, 44–46] were followed by detailed studies of the ion beam properties: The origin of the protons in the ion spectra is attributed to a water/ hydrocarbon contamination layer on the foil surfaces [47], the source size is in the order of  $\approx 100 \mu\text{m}$  and the emittance is 10 – 100 times lower compared to conventional accelerators [48–51]. The conversion efficiency from laser- to the kinetic energy of the ions is  $\leq 1\%$  [39].

Furthermore the dominant acceleration of target ions heavier than protons can be achieved by removing the contamination layer of the targets [52–54]. In order to generate quasi-monoenergetic proton/ ion spectra with energy spreads  $< 20\%$  the target geometry has to be changed. This is realized by (i) using spherical, electrically isolated targets with diameters smaller than the source size to reduce the transversal hot electron spread at the rear side [55–57] or by applying a small hydrogen-rich dot on the back surface of a foil target to enhance the proton yield in the central part [58, 59].

### Enhanced TNSA

As discussed above, the TNSA model is restricted to a certain range of the laser contrast and is described by an isothermal expansion of a quasineutral plasma on a time scale of the laser pulse duration [38, 40]. In case of an ultra-high contrast ( $< 10^{-11}$ ) and target thicknesses on the order of a few 100 nm this description is not well fitted anymore, since the main stage of ion acceleration in the expanding plasma begins after the end of the laser pulse and the plasma scale length is in the order of the Debye length. A more suitable description of an adiabatic expansion was found to account for this [21, 60, 61]. The electrons are (re-)circulating between the target and two Debye sheaths, one at the laser irradiated target front and the other at the target rear [62]. If a constant number of hot electrons permanently outside of the target (as in TNSA) is assumed, this results in a dependence of the maximum ion energy on the target thickness.

The ion acceleration in a thin target continues after the end of the laser pulse almost symmetrically from both sides of the foil and drops down after the adiabatic cooling of fast electrons. The aspects of symmetric acceleration and the appearance of an optimum thickness as an indication for this regime as further discussed in scope the of experiments in Ch. 7.2.

## 3.2 Radiation Pressure Ion Acceleration

During the last few years a novel mechanism of laser driven ion acceleration has gained a lot of interest [35, 63–69], where the particles are directly accelerated by the laser radiation pressure.

The basic principle of this idea was at first proposed in 1966 by Marx [70]. He raised the idea of a laser-driven vehicle by means of interstellar travel. The photons reflected from the moving vehicle/ sail will be red-shifted in the rest frame of the laser and thereby transfer a smaller fraction of momentum but a larger fraction of their energy to the sail. The efficiency approaches 100% as the vehicle reaches the speed of light. Hence, a 10GW laser powered over 10 years would accelerate a



vehicle of 30kg to relativistic velocities, neglecting the inherent divergence of the laser beam. Marx was indeed very optimistic since from his point of view, the main difficulty was the deceleration from relativistic speed at the final destination.

This idea was transferred to a thin foil target being accelerated entirely as soon as short pulsed high-power laser were available. It was shown that at intensities of  $10^{24}$  W/cm<sup>2</sup> the RPA is dominating other accelerations schemes and that ions could reach relativistic velocities within one laser cycle [33].

Later Macchi *et al.* [35] found that RPA can be revealed at much lower intensities by using circular polarization and normal incidence. In this case the generation of *hot* electrons (necessary in TNSA) is suppressed since the longitudinally oscillating component of the Lorentz force vanishes (cf. Ch. 1.1). Resonance- and Brunel Absorption are also disbanded due to the normal incidence of the laser (cf. Ch. 2.3).

In fact the so-called RPA-concept consists of two stages: (i) the initial stage, where the electrons are piled up to an equilibrium since the target ions are still immobile in that early stage and create a restoring electrical field. Later, the ions are set into motion layer-by-layer. And (ii) the light sail stage, where the target ions begin to move ballistically due to the electrical field created by the displaced and compressed electron layer which acts as an accelerated plasma mirror. During a few laser pulse cycles a quasi-stationary state is established and the plasma cloud expands with its center of mass moving at an almost constant velocity.

### 3.2.1 Initial Stage

As discussed above, an intense, circularly polarized laser pulse normally incident (along the x-axis) on targets with thicknesses below the collisionless skin depth (cf. Eq. 2.4) and with an ion density of  $n_i = n_0$  (Fig. 3.1a) will ionize the the whole target volume immediately.

The electrons are pushed inside the target by the ponderomotive force (cf. Ch. 1 and 2.2), while the ions are still immobile due to their high mass. The electrons are piled up to densities  $n_e = n_p$  and leave behind a charge depletion layer of thickness  $d$ . This gives rise to an restoring electrical field  $E_x$ . They quickly reach an equilibrium position where  $E_x$  balances the ponderomotive force (cf. Fig. 3.1a). As soon as the electron density exceeds the critical density, the condition of a sharp boundary is given and the pressure imposed on the electron layer might be described by the radiation pressure (cf. Ch. 2.2). Then, the balance condition with the electrostatic pressure can be formulated [64]:

$$\frac{\epsilon_0 E_0^2}{2} = \frac{I}{c}(1 + n_R). \quad (3.8)$$

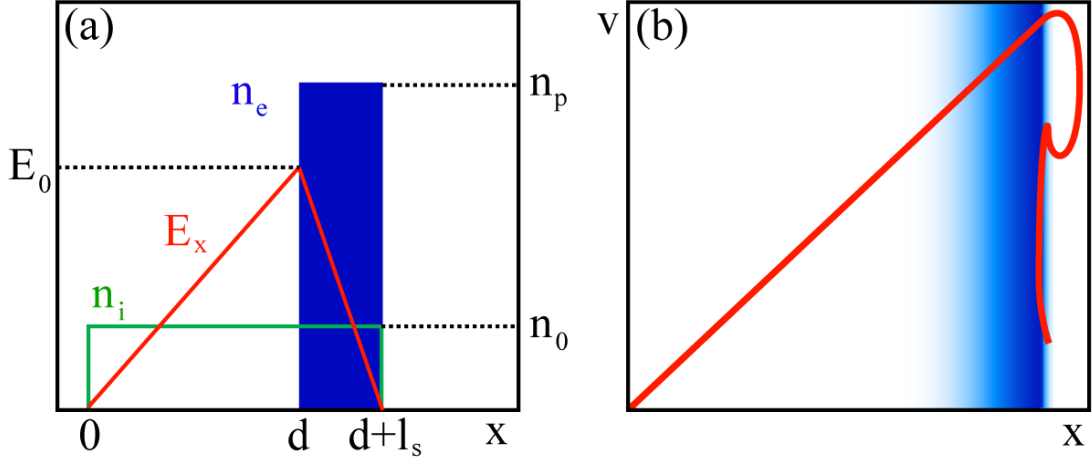


Figure 3.1: (a) Schema of the initial stage, where the electrons are in equilibrium and the ions still stationary, with the ion density (green line), the electron density (blue rectangle) and the electrical field (red line) [35]. (b) Ion phase space exhibiting characteristic loops when entering the unperturbed plasma region [64]

Assuming that all electrons are removed from the foil, the amplitude  $E_0$  of the electrical field  $E_x$  is given by the Poisson equation:

$$E_0 = \frac{en_0d}{\epsilon_0}. \quad (3.9)$$

By combining Eq.3.8 and Eq.3.9, the depth of the depletion layer is estimated:

$$d = \sqrt{\frac{2I\epsilon_0(1+n_R)}{cn_0^2e^2}}. \quad (3.10)$$

An expression for the optimum condition is found by introducing Eq.2.6 into Eq.3.10:

$$a_0\sqrt{1+n_R} = 2\pi \frac{n_e d}{n_c \lambda_L} \quad (3.11)$$

Introducing the laser and target parameter given in Ch. 7.1 and assuming total reflectivity ( $n_R = 1$ ) results in  $d \approx 2\text{nm}$ . In case of a target with an initial thickness below  $d$  the compressed electron layer will be expelled from the ions [71].

If the target thickness  $D$  meets the condition  $D \geq d$ , the foil remains in its initial shape while the ions respond to the strong electrostatic field  $E_x$ . Then the

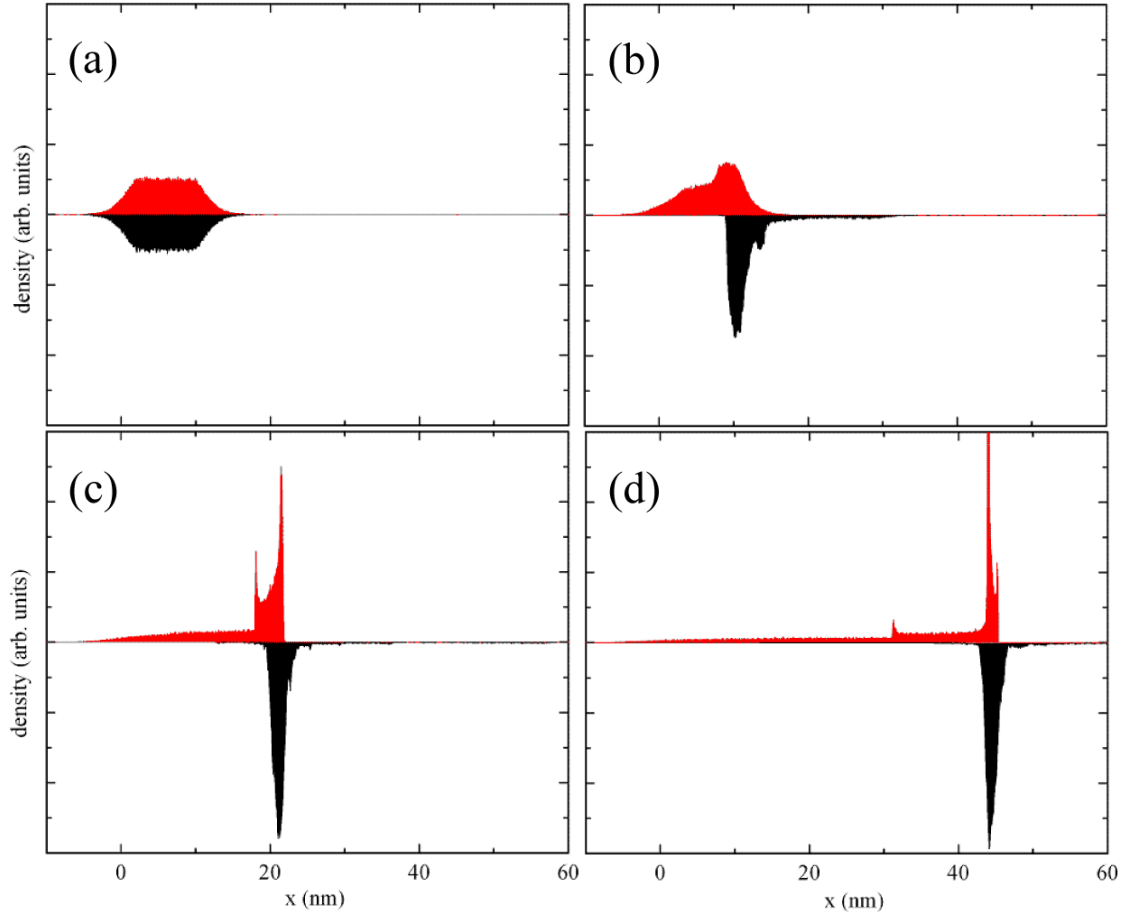


Figure 3.2: *Evolution of the electron density (black) and the ion density (red) from PIC simulation by A.A. Andreev<sup>1, 2</sup> at (a) 2.8fs (b) 5.6fs (c) 8.4fs and (d) 10.2fs after arrival of the trapezoidal pulse with a duration of 33fs and an intensity of  $2 \times 10^{19} \text{ W/cm}^2$ . The electron temperature in (a) has been set to 3keV to account for expansion, since the simulation here starts at an laser intensity of  $10^{17} \text{ W/cm}^2$ . The main features of the acceleration process described in the text are reproduced here: The compression of the electron layer in (b), the development of the left peak in the ions density (c) attributed to Coulomb explosion and the ballistic acceleration of the whole target in (d).*

optimum condition can be written as:

<sup>1</sup>Max Born Institute, 12489 Berlin, Germany

<sup>2</sup>Vavilov State Optical Institute, Sankt Petersburg, Russia

$$\sigma_{opt} \geq a_0/\sqrt{2}, \quad (3.12)$$

which is close to the empirical expression (Eq. 3.3) found by PIC simulations.

The ions initially in the depletion layer ( $0 < x < d$ ) will be accelerated by Coulomb explosion. This feature is also observed in the the PIC simulation (cf. Fig. 3.2).

The balance condition Eq. 3.8 is fulfilled for ions being initially in the compression layer ( $d < x < d + l_s$ ) for all times since  $E_x$  is a linear function of  $x$ . All these ions reach the point  $(d + l_s)$  at the same time with the same velocity. Then they cross the electron layer (indicated by blue-shaded area in Fig. 3.1b) and travel inside the target until they encounter the next layer of stationary ions. And since the inertia of the electrons is much lower than that of the ions, the compressed electron layer adjusts its positions immediately due to the light pressure. Now, the next stationary layer of ions experiences the electrostatic field and is accelerated itself. Thus, the acceleration proceeds layer by layer resulting in the characteristic loops in the phase-space as depicted in Fig. 3.1b. This cyclic acceleration continues until the target rear side is reached. Now, all ions have the same velocity and undergo the Light Sail Acceleration described in Ch. 3.2.2.

### 3.2.2 Light Sail Stage

Marx vision raised a lot of controversy and six month later Nature published a letter by Redding [72] that identifies a mistake in one of Marx's equations but introduces again statements concerning the efficiency which turned out to be wrong. Since this claim was still quoted in the literature, Simmons and McInnes published a paper 26 years later [73], where this topic was discussed finally. They conclude: *But whatever his mistakes, at least Marx was more right than his critics!*

Howsoever, applying this simple model of an accelerated mirror to the *optimum* parameters (Eq. 3.11) it turns out to be very predictive to estimate the ion energies. To obtain the equation of motion and an expression for the efficiency, the retarded time  $w = t - x/c$  is introduced to be aware of the delay between photon emission and the moment they reach the target. With  $dx/dt = w/c = \beta$ , the target velocity in the laser frame, it follows that

$$\frac{dt}{dw} = \frac{1}{1 - \beta}. \quad (3.13)$$

The light pressure  $p$  on the target between two events  $Q_1(x, t)$  and  $Q_2(t+dt, x+dx)$ , in the rest frame of the laser is

$$dp = \frac{(1 + n_R)I}{c} dw. \quad (3.14)$$

The Lorentz transformation to the instantaneous rest frame of the target introduces the Doppler shift

$$dp = \frac{(1 + n_R)I}{c} dw \sqrt{\frac{1 - \beta}{1 + \beta}} = \frac{(1 + n_R)I}{c} dw \gamma (1 - \beta), \quad (3.15)$$

with  $\gamma = (1 - \beta^2)^{-1/2}$ . The *proper time interval* between  $Q_1$  and  $Q_2$  is  $d\tau = dt/\gamma = dw/\gamma(1 - \beta)$  and hence,

$$dp = \frac{(1 + n_R)I}{c} \left( \frac{1 - \beta}{1 + \beta} \right) d\tau. \quad (3.16)$$

By transforming back to the laser frame and interpreting the light pressure as hydrostatic pressure by applying Pascal's law one obtains the equation of motion:

$$\frac{d}{d\tau}(\gamma\beta) = \frac{(1 + n_R)I}{\rho D c^2} \left( \frac{1 - \beta}{1 + \beta} \right), \quad (3.17)$$

where  $\rho$  and  $D$  are the target density and thickness. The final velocity of the foil  $\beta_f$  can be found in case of ( $n_R = 1$ ) as a function of the pulse fluence by using Eq. 2.6

$$\mathcal{F} = \int_0^w I dw \simeq \frac{2\pi I t}{\omega} = \frac{2\pi a_0^2 m_e n_c c^3 t}{\omega}, \quad (3.18)$$

where  $t$  is the laser pulse duration in laser cycles and finally by integrating Eq. 3.17:

$$\beta_f = \frac{(1 + E)^2 - 1}{(1 + E)^2 + 1}, \quad (3.19)$$

where  $E$  is the total energy output of the laser

$$E = \frac{2\mathcal{F}}{\rho D c^2} = 2\pi \frac{Z m_e a_0^2 t}{A m_i \sigma}, \quad (3.20)$$

with  $m_i$ ,  $A$  and  $Z$  being the ion mass, ion mass- and charge number.

The kinetic ion energy then calculates to

$$T = (\gamma - 1) m_i c^2. \quad (3.21)$$

### Nonlinear reflectivity

To include the effects of partial reflectivity and relativistic Self-Induced-Transparency into the Light Sail model, an analytical expression for the reflectivity of an over-dense plasma is introduced. According to Vshivkov *et al.* [74] the reflectivity of a

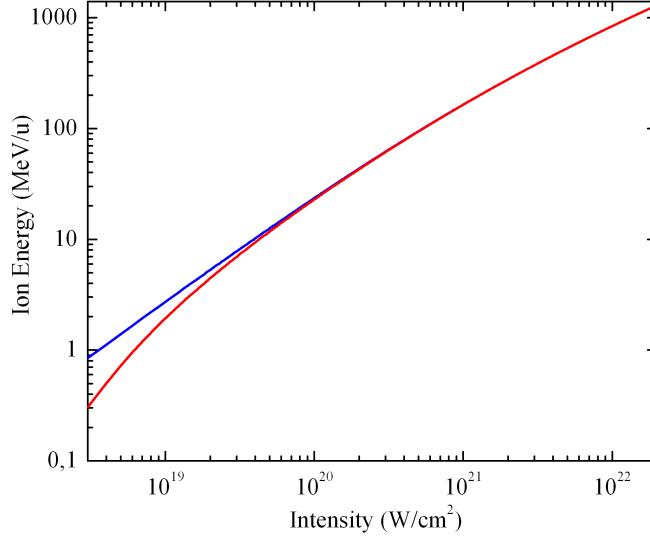


Figure 3.3: *Maximum ion energy as a function of the incident laser intensity for a reflectivity of  $n_R = 1$  (blue line) and  $n_R$  given by Eq. 3.22 (red line) at the particular optimum areal density  $\sigma_{opt} = a_0/\sqrt{2}$  and a pulse duration of  $t = 15$  laser cycles.*

plasma density profile with a delta-functional shape is well approximated by the normalized areal density  $\sigma$  (Eq. 3.2) and is given in the restframe of the foil by,

$$n_R = \frac{\sigma^2}{1 + \sigma^2}. \quad (3.22)$$

Using this expression of  $n_R$  in Eq. 3.17 gives rise to the following expression of the final velocity [69]:

$$\beta_{n_R}(w) = \frac{(1 + E(w) - \sigma^{-2})^2 \left( 1 + \sqrt{1 + 4\sigma^{-2} (1 + E(w) - \sigma^{-2})^{-2}} \right) + 2\sigma^{-2} - 2}{(1 + E(w) - \sigma^{-2})^2 \left( 1 + \sqrt{1 + 4\sigma^{-2} (1 + E(w) - \sigma^{-2})^{-2}} \right) + 2\sigma^{-2} + 2} \quad (3.23)$$

In case of a *flat-top* temporal laser profile, i.e. a constant intensity,  $E(w)$  can be written as a function of time

$$E(t_p) = 2\pi \frac{Zm_e a_0^2 t_p}{Am_i \sigma T}, \quad (3.24)$$

where  $t_p$  and  $T$  are the durations of the laser pulse and the laser period.

In Fig. 3.3 the kinetic ion energy is plotted as a function of the laser intensity for a laser pulse duration of  $t_P = 45$  fs ( $t = 15$  and  $T = 2.8$  fs). Here, the two cases  $n_R = 1$  and  $n_R$  given by Eq. 3.22 are compared and the areal density was matched to the particular optimum condition (Eq. 3.12). In the limit  $\sigma \rightarrow \infty$ , i.e.  $n_R \rightarrow 1$ , Eq. 3.20 is recovered.

The resulting ion spectra are intrinsically monoenergetic and an ion energy of 1 GeV might be obtained with a laser intensity of  $\sim 2 \times 10^{22}$  W/cm<sup>2</sup>.

### Efficiency of the Light Sail Acceleration

The efficiency  $\eta$ , defined as the ratio between the kinetic energy of the accelerated target over the electromagnetic energy of the laser pulse can be obtained by the conservation of the photon number  $N$  reflected by the moving target. The total energy of the incident photons is  $N\hbar\omega$  and the reflected photons is  $N\hbar\omega_r$  respectively. The frequency of the reflected photons  $\omega_r$  is given by the Lorentz-Transformation (Doppler-shift) from the rest frame of the laser to the mirror and back and thus:

$$\omega_r = \frac{1 - \beta}{1 + \beta} \omega. \quad (3.25)$$

Hence the energy transferred to the target is

$$\Delta E = N\hbar\omega - N\hbar\omega_r = \underbrace{\frac{2\beta}{1 + \beta}}_{=\eta} N\hbar\omega. \quad (3.26)$$

It follows that  $\eta \rightarrow 1$  as  $\beta \rightarrow 1$  and that the velocity of the target depends only on how much energy has been pumped and not how.





## Chapter 4

# Surface High Harmonic Generation by Coherent Wake Emission

High-order harmonic generation (HHG) due to reflection of an intense laser beam from a steep, overdense plasma gradient has been observed since the 1970s [75–77]. In contrast to this early measurements, the generation process in case of femtosecond laser pulses has been found recently [78, 79].

The generation of high harmonic radiation from a solid density bulk [23, 24, 79–84] as well as foil targets [78, 85, 86] has been studied extensively in the last years and is mainly motivated by the possibility to generate energetic short-wavelength light pulses. Simultaneously, HHGs give a detailed insight into the laser plasma dynamics as they allow the probing of the plasma density [12, 79], magnetic fields [87], surface dynamics [82, 88] and electron heating [85]. Properties which are highly interesting e.g. for the understanding of ion acceleration processes from thin foils as done in Ch. 9.

The mechanism of Coherent Wake Emission (CWE) is based on a phase matching of the laser field with plasma oscillations inside an overdense plasma gradient which leads to the emission of harmonics up to the plasma frequency.

To achieve this regime a p-polarized, intense laser pulse has to obliquely incident onto a plasma with a finite scale length. If the assumptions of Brunel absorption (Ch. 2.3.2) are fulfilled, electrons in the vicinity of the sharp plasma density profile are accelerated into the vacuum during one half laser cycle and back into the plasma when the field reverses. They pass the critical density surface into the overdense region, where the laser field is no longer able to act on them. On their way, the electrons excite plasma waves in their wake field. Under certain conditions these plasma waves can undergo linear mode conversion and radiate electromagnetic waves - in principal due to inverse resonance absorption [89, 90]. The periodic repetition of this process, every laser cycle, leads to a spectrum of harmonics of the incident laser frequency [79].

The unique properties of the high harmonics generated by CWE clearly distinguishes them from relativistic harmonics generated in the regime of the *Relativistic Oscillating Mirror (ROM)* [24, 80]:

(i) CWE harmonics can be generated at sub-relativistic intensities ( $a_0 \ll 1$ ) as low as  $10^{16} \text{W/cm}^2$  [79].

(ii) CWE exhibit a cut-off in the harmonic spectrum which does not depend on the laser intensity but on the density of the target material itself, since CWE harmonics are generated by the mode conversion of the plasma waves as described above. The wavelength of the emitted harmonic is given by the frequency of the plasma wave which is a function of the local electron density. Therefore each harmonic is created in a certain depth of the plasma gradient and the cut-off harmonic number  $q_{co}$  is determined by the maximum electron density:

$$q_{co} = \sqrt{\frac{n_e}{n_c}}. \quad (4.1)$$

This dependence has been shown experimentally [91, 92] with a typical value for  $q_{co}$  of 20 for fused silica or 14 for Polymethylmetacrylate.

(iii) CWE harmonics show two kinds of chirps: the harmonic-chirp inside each harmonic and the atto-chirp between the individual harmonics. The harmonic-chirp is attributed to the fact that a fs laser pulse changes its intensity during the pulse and therefore, the Brunel electrons being pulled in the vacuum spend a different amount of time there before being re-injected into the plasma [79]. This time spacing increases linearly during the laser pulse and is analogous to what happens during the generation of gas harmonics [93].

The atto-chirp on the other hand is related to the fact that each harmonic is created at a specific depth in the plasma gradient. Because, the resonance condition of the created plasma wave is dependant on the local electron density, which is higher for higher frequencies. Therefore, higher order harmonics have to travel a longer distance to the plasma surface than lower order harmonics.

The atto-chirp has been quantified by means of XUV-autocorrelation [84].

# Part II

## Hardware



# Chapter 5

## Laser System

The fundamental study of laser-plasma interactions (e.g. laser-ion acceleration) in the relativistic regime requires electromagnetic fields at ultra-high intensities ( $I_L > 10^{18} \text{ W/cm}^2$ ). To reach this intensity, e.g. a laser pulse energy of a few hundred millijoule with pulse duration of a few femtoseconds are needed. Delivering such pulses is the primary purpose of the High-Field Laser System at the Max-Born Institute.

In Ch. 5.1 a short overview of the TW-Ti:sapph system is given. The key to achieve such high intensities and avoid damage of elements in the amplified chain at the same time, is a technique called *Chirped Pulse Amplification* (CPA) [2]. With this technique an amplification up to the petawatt level becomes possible.

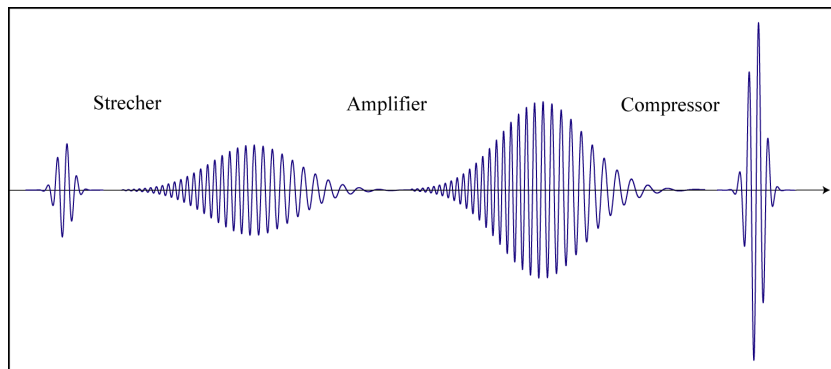


Figure 5.1: *Principle of Chirped Pulse Amplification (CPA)*

Before the invention of CPA the amplification of femtosecond laser pulse was limited to a few millijoule because a laser pulse at intensities of  $\sim \text{GW/cm}^2$  causes damage to the amplifier crystals through non-linear effects such as self-focussing. Additionally, it is not advising to allow its propagation in air since the laser pulse

would immediately self-focus or cause filament propagation which would ruin the original pulses qualities. However it is anyhow possible to allow propagation in air if the beam diameter is expanded and hence, self-focussing and filamentation are suppressed. But at some point the intersection to the vacuum has to be realized in order to conduct laser matter interaction experiments. In order to minimize any nonlinearities at the transmittance through a window into the vacuum, the intensity should be as low as possible.

In order to keep the intensity of the laser pulse below the threshold of the nonlinear effects, in CPA, the femtosecond pulse is first stretched in time, then amplified and finally re-compressed in vacuum (Fig. 5.1).

In chapter 5.2 it is described how the laser pulse was characterized by means of (i) *Spectral Phase Interferometry for Direct Electric-field Reconstruction* (SPIDER) [94] and (ii) *scanning 3rd order cross-correlation* similar to [95]. These techniques allow the (i) reconstruction of the temporal shape of the main pulse by spectral shearing interferometry on a femtosecond time-scale and (ii) high precision measurements of the *Amplified Spontaneous Emission* (ASE) background level on a nanosecond time-scale. The duration of the ASE pedestal is usually several orders of magnitude longer than the main pulse but still carries a fraction of the total pulse energy, resulting in intensities well above the ionization threshold of any target in the laser focus.

Chapter 5.3 illustrates one possibility to enhance the temporal intensity contrast between laser pulse peak and ASE pedestal. To improve this contrast by 4-5 orders of magnitude combined with a steep rising edge, the use of a *Double-Plasma Mirror* [19, 21, 96] is required. In fact, the plasma mirror is the key technology to access the transparency regime of laser-ion acceleration.

## 5.1 Ti:Sapphire High-Field Laser

The High-Field Laser at MBI is a >30TW-Ti:sapph based on the CPA technique. A schematic setup is shown in FIG. 5.2.

The primary femtosecond (17 fs) pulses with an average power of 300 mW are generated by a commercially available Kerr-lens mode-locked oscillator [97] with a repetition rate of 81.5 MHz. In the stretcher a linear frequency chirp is introduced onto the pulse by the use of an all-reflective Oeffnertriplet telescope [98]. Due to the combination of two spherical concentric mirrors (the first concave, the second convex) with a single grating, the stretcher is completely characterized by symmetry and hence, symmetrical aberration and astigmatism are disbanded. Chromatic aberrations are per se excluded, because all the optical elements are mirrors. The result is a stretched laser pulse with a duration of  $\approx 700$  ps. Afterwards the pulse is amplified in three consecutive multi-pass stages up to 4 J. Between those ampli-

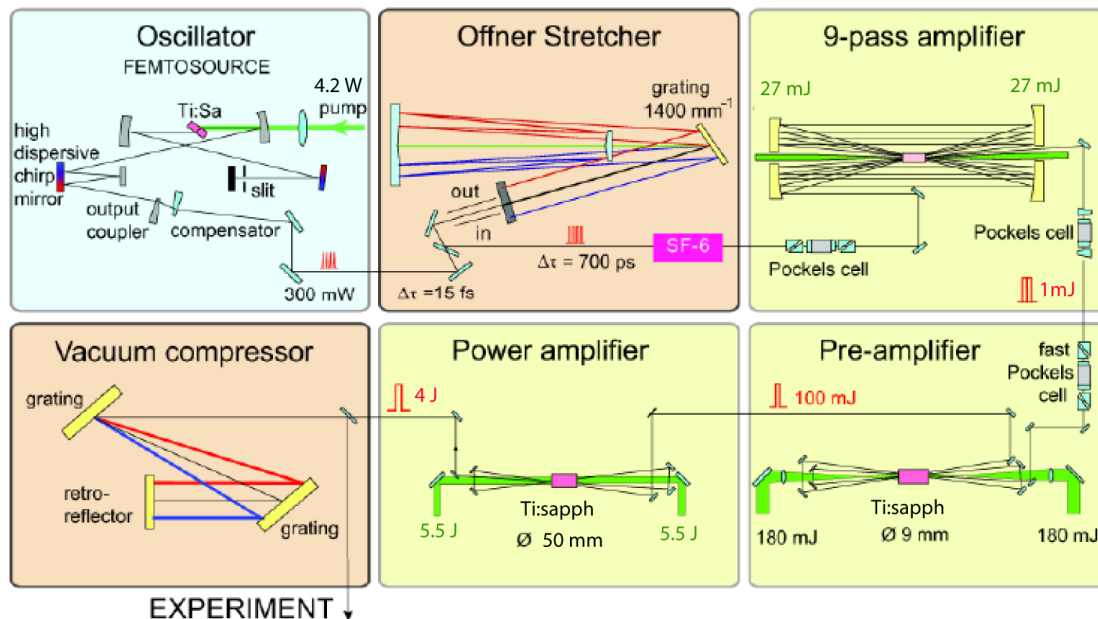


Figure 5.2: *Schematic drawing of the MBI TW Ti:sapp laser.*

fier stages the beam diameter has to be extended -to avoid damage of the amplifier crystals- up to  $\sim 100$  mm for a reasonable flux on the compressor grating. Finally, the laser pulse is directed in a vacuum chamber where the compression takes place. The compressor basically consists of two parallel grating and an vertical roof mirror retro-reflector. Motorized stages serve for alignment of the grating in vacuum. Online compensation of (high-order) phase dispersion becomes possible due to the measurement of the spectral phase with a SPIDER as described in chapter (5.2). The final pulse lengths is in the range of 40 – 50 fs.

## 5.2 Laser Pulse Characterization

### 5.2.1 Spectral Phase Interferometry for Direct Electric-Field Reconstruction

Spectral Interferometry is a method to measure the phase difference, of two laser pulses travelling along different optical paths, in the frequency domain. The experimental setup only consists of an interferometer (e.g. Michelson) and a spectrometer to detect the spectral intensity of the two recombined laser pulses. The resulting spectral interferogram exhibits a strong intensity modulation along the frequency axis with and -in case of two identical pulses- a constant modulation

period length  $\omega$  which decodes the temporal separation of the pulses  $\tau = 2\pi/\omega$ .

In spectral shearing interferometry -such as SPIDER is- the frequencies of the two identical replicas of the input pulse are shifted by a small amount  $\Omega$  with respect to each other. The measured spectral interferogram yields

$$S(\omega_c) = |\tilde{E}(\omega_c)|^2 + |\tilde{E}(\omega_c + \Omega)|^2 + 2|\tilde{E}(\omega_c)\tilde{E}(\omega_c + \Omega)| \times \cos[\phi_w(\omega_c + \Omega) - \phi_w(\omega_c) + \omega_c\tau], \quad (5.1)$$

where  $\tilde{E}(\omega_c)$  is the electric field in frequency representation of the variable center frequency of the spectrometer  $\omega_c$ .  $S(\omega_c)$  consists of three summands. The first and the seconds represent the sum of the two spectra which do not contain any phase information. The third is the result of interference and carries all of the phase information in terms of the phase difference.

A simulated interferogram is shown in Fig. 5.3a.

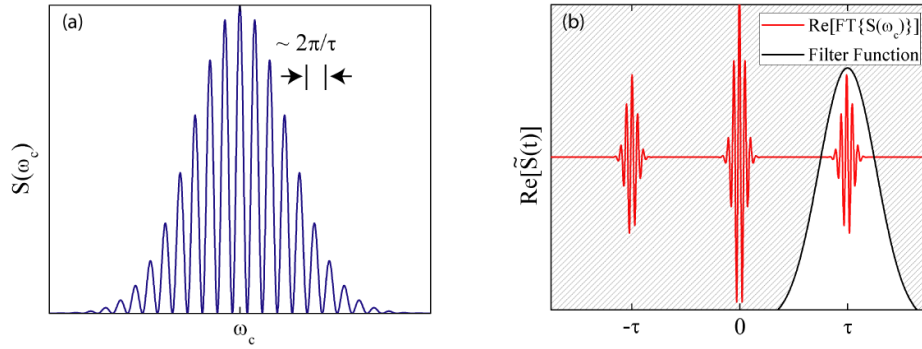


Figure 5.3: *Simulated Interferogram (a) and its Fourier Transform including a 4th order super Gaussian filter function (b).*

The procedure of reconstructing the phase shall be sketched in the following: At first the Fourier transform of  $S(\omega_c)$  is calculated and one of the oscillating terms is isolated by a filter function. This time series reveals three components at  $t = \pm\tau$  and at  $t = 0$  (cf. Fig. 5.3b). The Filter function is typically a fourth order super Gaussian of full width  $\tau$ . The filtered time series is inverse fourier-transformed afterwards. Secondly, the linear phase term  $\omega_c\tau$  has to be removed. For this purpose a spectral interferogram is recorded without adding a spectral shear. Since the two pulses are identical now, the only phase contribution is  $\omega_c\tau$ . If this linear part is subtracted, the phase difference is



$$\Theta(\omega_c) \equiv \phi_w(\omega_c) - \phi_w(\omega_c - \Omega). \quad (5.2)$$

If the shear is relatively small compared to the structure of the spectral phase,  $\Theta(\omega_c)$  may be approximated with

$$\Theta(\omega_c) \approx \Omega \frac{d\phi_w(\omega_c)}{d\omega_c}. \quad (5.3)$$

With the help of this approximation, the spectral phase can be reconstructed by integration

$$\phi_w(\omega_c) = \frac{1}{\Omega} \int d\omega_c \Theta(\omega_c). \quad (5.4)$$

Finally the spectral amplitude  $|\tilde{E}(\omega_c)|$  has to be determined. This is realized by a separate measurement of the laser pulse spectrum.

The approach of the SPIDER as introduced in 1998 by C. Iaconic and I. A. Walmsley [94] uses two replicas of the original pulse which are delayed with respect to each other with an interferometer. A third one is stretched in time and strongly chirped. Afterwards they are recombined in a thin nonlinear crystal by Sum Frequency Generation (SFG). By doing so each of the two replicas is up-converted with a different monochromatic frequency component of the third pulse. Thus, both pulses are frequency shifted to the second harmonic frequency range by a slight different amount resulting in the necessary frequency shear (cf. Fig. 5.4).

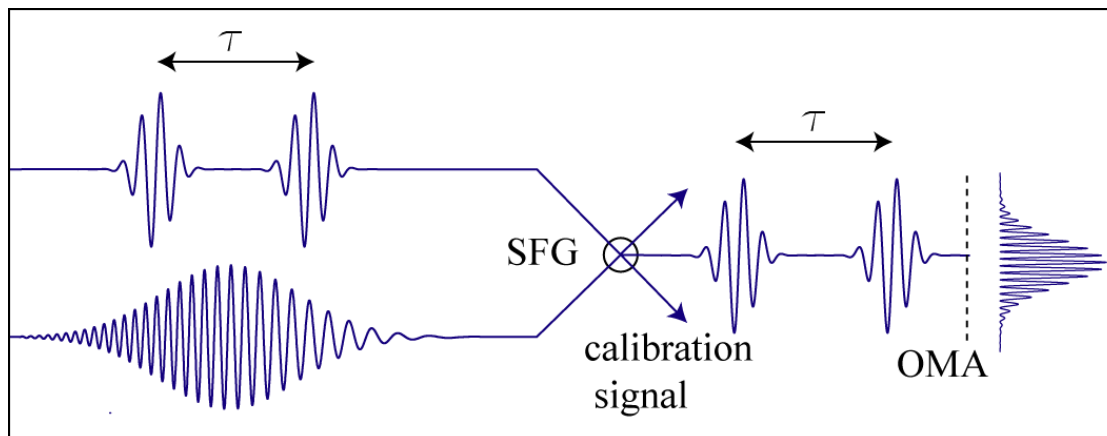


Figure 5.4: *Principle of the SPIDER setup*

The resulting interferogram differs from Eq. (5.1) by only a frequency shift. Thus, the pulse may be reconstructed as described above using only algebraic operations on the interferogram.

Fig. 5.5a shows the interferogram recorded with the Spider setup as described above of the Ti:Sapph Laser System at 500 mJ. In Fig. 5.5b the reconstructed laser pulse in the time-domain is plotted along with the reconstructed spectral phase. A Gaussian Fit of the temporal profile yields to a laser pulse duration of  $(45 \pm 1)$  fs. A constant phase would describe a fourier limited pulse and therefore an optimum compressor alignment. The every day performance of the Ti:Sapph laser deviates from this optimum, but the characteristics of the spectral phase reveal the potential of optimizing the compressor alignment. Hence, laser pulse durations in the region of 30 – 35 fs are accessible with this laser system.

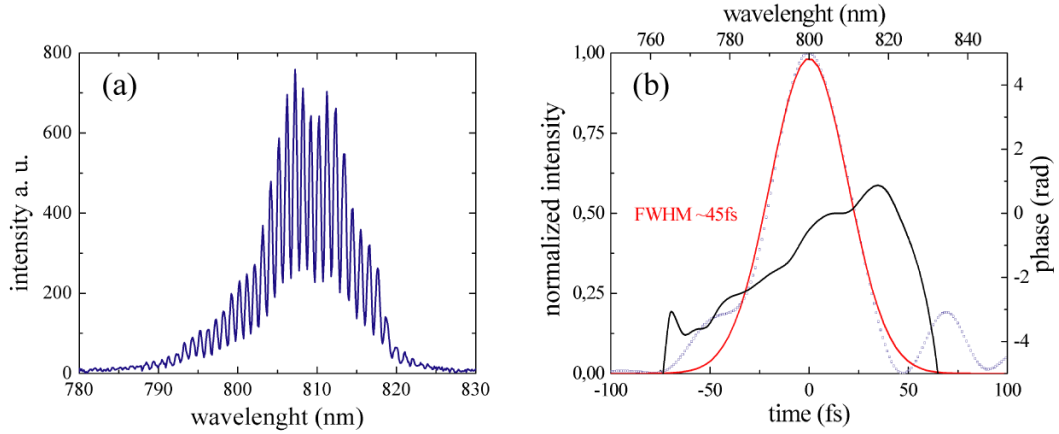


Figure 5.5: (a) The interferogram as recorded with the SPIDER setup. (b) The reconstructed laser pulse in the time domain (blue squares) and its Gaussian Fit (red line), yielding to a laser pulse duration of  $(45 \pm 1)$  fs (FWHM). The reconstructed phase is plotted as black line

### 5.2.2 Scanning 3rd order Cross-Correlation

In addition to the characterization of the laser main pulse on a fs time scale the knowledge of the pulse pedestals intensity on a ns time-scale is crucial for the experiments described in this thesis. The level of the pedestal is described by the relation between the intensity of the peak of the main pulse and the intensity of the pedestal itself i. e. the temporal intensity contrast. Since the pedestal carries a significant fraction of the total pulse energy, its intensity is sufficient to ionize or even destroy any material in the laser focus before the arrival of the main pulse.

The challenge of the temporal characterization of a femtosecond laser pulse is to measure the actual profile of the pulse, e.g. to distinguish between pulse front and tail on a ns-time scale with a fs-resolution and a dynamic range of  $> 10$  orders

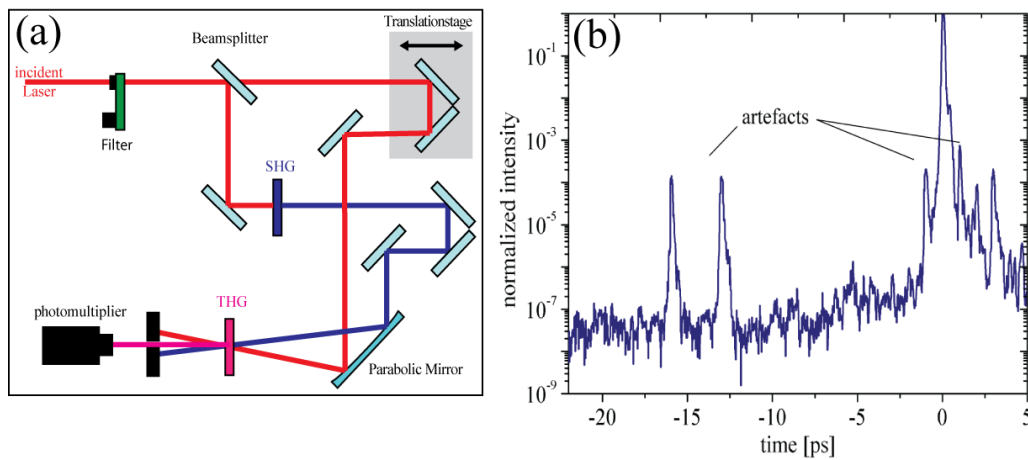


Figure 5.6: (a) Principle setup of the 3rd order cross Correlator. (b) Measured temporal profile of the MBI high-field Ti:sapph. The artefacts occur due to reflections in the correlator setup.

of magnitude. The use of an 3rd order non-linear process is one possibility to fulfill these requirements.

In a 3rd order cross-correlator (Fig. 5.6(a)) a laser pulse with frequency  $\omega$  is split into two identical pulses by the use of a beamsplitter. One pulse is frequency doubled by Second Harmonic Generation (SHG) in a non-linear crystal and focussed into a second crystal together with the delayed second pulse. By sum-frequency-generation the third harmonic ( $2\omega + \omega$ ) of the original laser pulse is generated. The linear superposition principal of electric fields is not valid in non-linear crystals, the electric fields here superimpose multiplicative. The used setup is a scanning alignment (multi-shot) with a translation stage to delay the two pulses with respect to each other from 20 fs up to 1 ns. A photomultiplier is used for the detection of the  $3\omega$  pulse. The dynamic range (10 orders of magnitude) is realized by adjusting the photomultiplier voltage, e.g. the amplification. In addition a set of calibrated filters is used in the original beam path.

In Fig. 5.6b a typical example for the obtained temporal pulse profile of the MBI Ti:Sapph laser (Ch. 5) is shown. Thus, the initial temporal contrast 30ps before the arrival of the main pulse is in the order of  $\approx 5 \times 10^{-7}$ , originating mainly from amplified spontaneous emission (ASE) in the amplifier crystals. It additionally consists of two ramps, one beginning  $\approx 5$  ps before the main pulse where the contrast linearly increases up to  $\approx 10^{-7}$  at 1 ps before the main pulse and the second beginning  $< 1$  ps before the main pulse reaching up the main pulse where

the contrast reaches values of  $\approx 10^{-5}$ . This is owing to imperfect compression of the laser pulse and are hence only erasable after the final compressor, e.g. by means of an Plasma Mirror which is described in the next chapter (Ch. 5.3). The pulse profile does not own any real pre-pulses, since they were originating from a leakage in a regenerative amplifier which is not applied in the current setup (Ch. 5.1)

### 5.3 Double Plasma Mirror

Essential for the generation of high energetic ion beams and high harmonics from the interaction of a high intensity laser pulse with a solid target with nanometer thickness is the improvement of the intrinsic contrast (Ch. 5.2.2) of the Ti:sapph laser system (Ch. 5.1) by 4 – 5 orders of magnitude. Thereby it can be assured that the main pulse not only interacts with an intact target but also with a steep plasma gradient.

Hence, the research in the field of contrast enhancement has been intensified during the last years. Basically two approaches have been considered: Improvement of the laser chain itself or the cleaning of the pulse after it has been compressed. Electro-optical methods (e.g. Pockels Cells) are capable of suppressing pre-pulses on a ns time scale [99] as well saturable absorbers [100]. More advanced concepts use a double CPA [101] with additional elements based on cross-polarized wave generation (XPW) [102] or Optical Parametrical CPA (OPCPA) with short pulse (fs-ps) pump lasers [103].

Self-induced plasma switches (Plasma Mirrors (PM)) for contrast enhancement were first demonstrated with glass targets in 1991 [104] and with liquid targets in 1993 [105]. In 1994 the contrast enhancement was measured by means of 2nd order autocorrelation [18], a full characterization of a single PM was given in 2004 [19, 20]. The demonstration of a Double Plasma Mirror (DPM) in 2006 [106]. In 2007 it was shown that a PM is also applicable for sub-10-fs lasers with a kHz repetition rate [107].

The PM technique is based on focussing a high intensity laser pulse on a transparent medium in a way that most of the ASE-pedestal is transmitted while the raising edge of the main pulse rapidly ionizes the surface of the medium. When the electron density reaches the critical density  $n_c$  (cf. Eq. 2.5), the reflectivity increases abruptly. To achieve the highest possible reflectivity for the main pulse, the incident intensity has to be adjusted in a way that the PM is triggered at the raising edge of the main pulse. At the same time it has to be assured that the reflecting surface is still planar, i. e. to prevent a long-scale pre-plasma. The contrast enhancement  $C$  is simply given by the ratio of the reflection coefficients from the overcritical plasma surface  $n_p$  and from the undisturbed *cold* medium  $n_m$ :

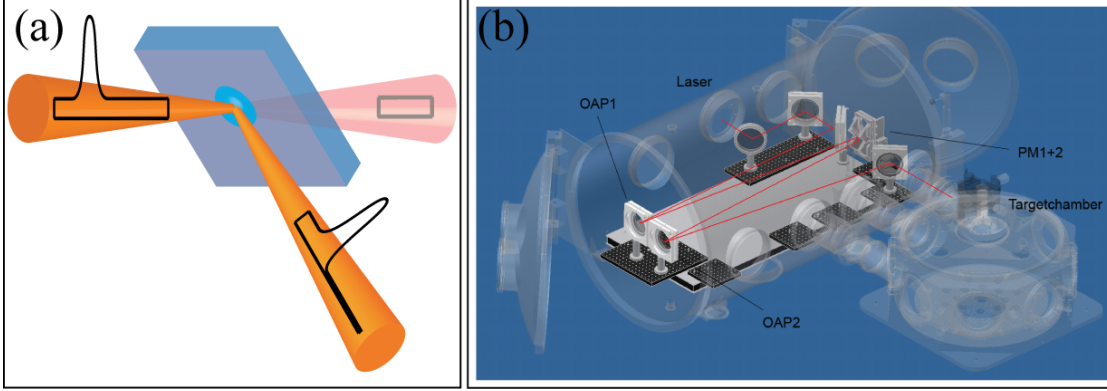


Figure 5.7: (a) A laser beam is focused on an anti-reflection coated medium, in a way that most of the pedestal energy is transmitted. With increasing of the intensity in time, electrons are excited in the medium. If the electron-density reaches the critical density  $n_c$  the reflectivity increases abruptly, the laser pulse is reflected. (b) The first off-axis parabolic mirror (OAP1) focuses the incoming beam between the two Plasma Mirrors (PM1+2). The pulse is then re-collimated by the second OAP (OAP2) and afterwards directed to the final target chamber.

$$C = \frac{n_p}{n_m} \quad (5.5)$$

Thus, the contrast enhancement is principally given by the quality of the anti-reflection coating of the used PM substrates. The *cold* reflectivity is specified by the vendor of the plasma mirror substrates to be  $n_m < 0.5\%$  [108]. Then the contrast enhancement by two successive PM is better than 4 orders of magnitude.

To be of any practical use, the reflected beam quality should show no degradation relative to the incident beam. Consequently the PM surface must remain flat compared to the laser wavelength. The plasma expansion time has to be restricted, resulting in an upper limit  $\Delta t$  that can elapse between plasma formation and the arrival of the main peak. A tolerable expansion of the critical surface of  $\lambda/4$  is assumed. Thus, the inequality

$$c_s \Delta t < \frac{\lambda}{4} \quad (5.6)$$

has to be fulfilled. Here  $c_s$  is the sound speed of the expanding plasma surface. It has been measured from the blue-shift of the laser spectrum reflected off the PM surface and is quantified to  $\approx 5 \times 10^7 \text{ cm s}^{-1}$  for an incident intensity of  $10^{16} \text{ W/cm}^2$  [18, 20]. This results in  $\Delta t \approx 400 \text{ fs}$ .

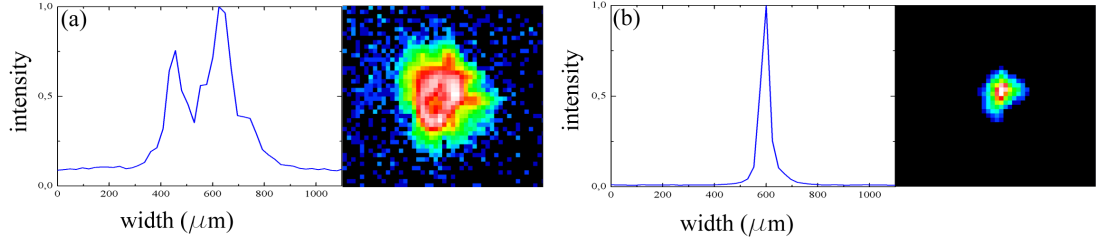


Figure 5.8: (a) Beam profile incident on PM1, showing the near field modulations 100 mm out of focus, with  $I \approx 3 \times 10^{16} \text{ W/cm}^2$  and (b) on PM2, 1 mm out of focus with  $I \approx 10^{18} \text{ W/cm}^2$ .

For the present pulse shape (cf. Fig. 5.6b) this suggests the use of a focussing optic with a focal length of 10 m in order to lower the focus intensity to values  $< 10^{17} \text{ W/cm}^2$ . Since this is unpractical, off-axis parabolic mirrors (OAPs) with a focal length of 1.5 m are used in this setup, what results in a focal intensity of  $10^{18} \text{ W/cm}^2$ . Hence, the first PM substrate has to be placed in near field of the incident beam to lower the intensity on the PM surface. This may result in a distortion of wave-front since the near-field exhibits modulation, but it has been shown that the profile of the reflected pulse is hardly disturbed and that the beam is still very well focusable [20, 109].

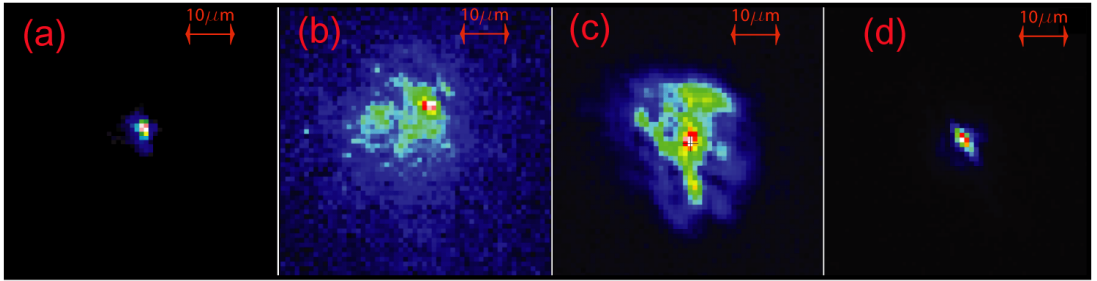


Figure 5.9: (a) The imaged back-reflections (CCD2 Fig. 7.1) for 3 different contrast ratios were recorded with a 16-bit CCD camera at the same zoom level and full dynamic range compared to a low-energy shot without plasma generation (a): (b) initial contrast: without DPM ( $D = 30 \text{ nm}$ )  $C=5 \times 10^{-8}$ , (c) high contrast: uncoated BK7 ( $D = 5.3 \text{ nm}$ )  $C=10^{-10}$  and (d) ultra-high contrast: ( $D = 5.3 \text{ nm}$ )  $C=10^{-12}$ .

The second substrate is placed in the focus (or slightly after in the expanding

beam) since the contrast here has been increased already and the 2nd PM thereby acts as spatial filter [110]. The corresponding beam profiles are shown in Fig. 5.8.

The PMs are situated, both with an  $45^\circ$  angle of incidence, at distance variable between 5 mm and 20 mm. Computer-controlled translation stages move the Plasma Mirrors in 3 dimensions: (i) parallel to their surfaces ( $x$ ) to provide a clean surface for each shot, (ii) on the beam-axis ( $z$ ), to find the best focal position, (iii) and for alignment purposes in ( $y$ ) and ( $\Delta y$ ) to vary the distance between the two surfaces.

It has been shown [20] that the reflectivity of a single PM suddenly increases when the laser intensity reaches the collisionless regime ( $I > 10^{15} \text{ W/cm}^2$ , Ch. 2.3). To exclude Resonance- and Brunel Absorption s-Polarization with respect to the PM surfaces was used. For that reason the reflectivity raises until relativistic absorption effects (cf. Ch. 2.3) become significant and/or the reflected beam quality is degraded by deformations of the critical surface due to the radiation pressure (Ch. 2.3.3).

To control the high spectral reflectivity near- and far-field of the reflected beam is monitored by CCD1+2 (Fig. 7.1). The near-field camera is also capable to measure the overall reflectivity from the DPM-system, since it has been cross-calibrated with a calorimeter in the main beam path (Fig. 5.10). By monitoring the far-field by means of the backscattered light from the final target it is also assured that the main laser pulse interacts with an intact target (Fig. 5.9).

The overall reflectivity of the DPM system is shown in Fig. 5.10. For the shots with negative shot numbers the intensity on the PM surfaces was adjusted by varying their positions relative the the laser focus i. e. the intensity on the surfaces. For the shots 1 – 23 the intensities were kept constant. The linear decrease of the reflectivity from 65% to 50% is attributed to the accumulated debris originating from the plasma expansion. To minimize this effect a ceramic aperture was placed between the two PM surfaces (Fig. 7.1).

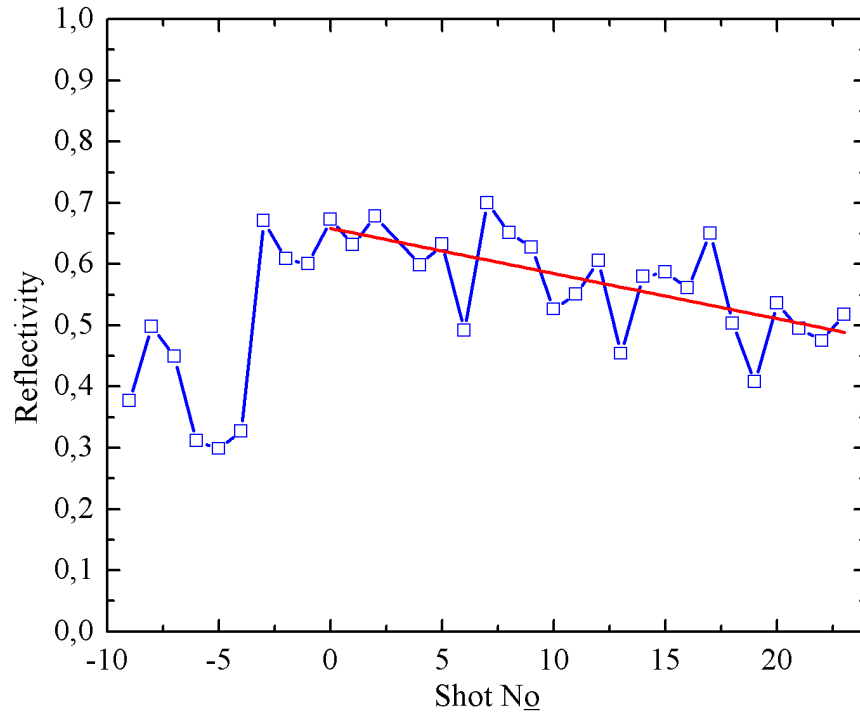


Figure 5.10: Overall reflectivity of the DPM system: The negative shot numbers mark the alignment procedure, where the intensities on the PM substrates was varied. After optimizing (positive shot numbers), the intensities were kept constant. The linear decrease of the reflectivity due to accumulated debris is emphasized by a linear fit (red line).



# Chapter 6

## Diagnostics

## 6.1 Thomson Spectrometer

The spectral properties as well as the number of accelerated proton and ions can be measured with a Thomson Spectrometer. It consists of a pinhole and a magnet combined with electric field plates such as their field lines are parallel to each other and placed perpendicular to the direction of propagation of the ions and particle detector [111]. Technical details of the used spectrometer can be found in [112].

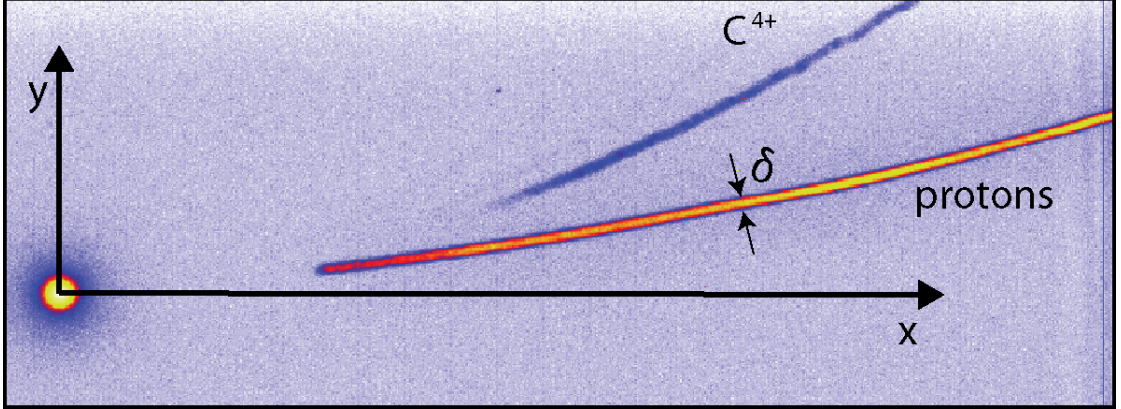


Figure 6.1: *CCD image of the illuminated phosphor screen coupled to the MCP from a  $5\mu\text{m}$  Titanium foil. The zero point determines the projection of the pinhole without any deflection.*

A small ion beamlet propagating in  $z$ -direction through the pinhole is deflected by the magnetic field  $B_y$

$$x = \frac{QB_y l L}{m_i v}. \quad (6.1)$$

The different ion species, i.e. particles with different  $Q/m_i$  are separated by the deflection of the electric field  $E_y$

$$y = \frac{QE_y l L}{m_i v^2}, \quad (6.2)$$

where  $Q$  is the charge of the ion and  $m_i$  its mass,  $l$  the effective extension of the electric and magnetic field and  $L$  the distance between magnet and detector. For particles with the same  $Q/m_i$ , the parabolic equation can be obtained by combining Eq. 6.1 and 6.2

$$y = \frac{m_i E_y}{QB_y^2 l L} x^2, \quad (6.3)$$

which has its vertex in the zero point. It has to be denoted that Eq. 6.1-6.3 are only valid for small angles of deflections. The particles are detected with a Multi-Channel Plate (MCP) with a diameter of 80 mm coupled to a phosphor screen and an attached CCD camera. The resulting counts of the CCD image were calibrated with the detection sensitivity of the MCP, by using 5.48 MeV particles emitted from a  $^{241}\text{Am}$  source [112].

In Fig. 6.1 a typical picture of an ion spectrum from a Titanium foil with a thickness of  $5\text{ }\mu\text{m}$  as target is shown. The energy resolution of the Thomson Spectrometer is given by the width of the parabolic trace  $\delta$  [113] which can be extracted from the CCD image (Fig. 6.1).

The energy uncertainty  $\Delta E$  is estimated by

$$\frac{\Delta E}{E} \approx \frac{\delta}{x}, \quad (6.4)$$

where  $x$  is the magnetic deflection (Eq. 6.1) and is defined by the spectrometer setup:

$$\Delta E \approx \frac{\delta}{a}, \quad a = \frac{QB_y l L}{\sqrt{2m_i}}. \quad (6.5)$$

In the used setup the detected solid angle is  $114 \times 10^{-9} \text{ sr}$  and the energy is resolution  $\Delta E/E \approx 3\%$ .

## 6.2 XUV-Spectrometer

For the detection of the harmonic radiation presented in Ch.9 a modified version of a commercially available *Acton Research VM-502* has been used. It is a compact 20 cm focal length normal incidence vacuum spectrometer designed for measurements ranging from UV down to the XUV spectral range. Due to the normal incidence geometry the reflectivity of the concave, iridium coated (1200 lines/mm) grating limits the detectable wavelength to  $> 50$  nm, i.e. a harmonics up to the order of 16.

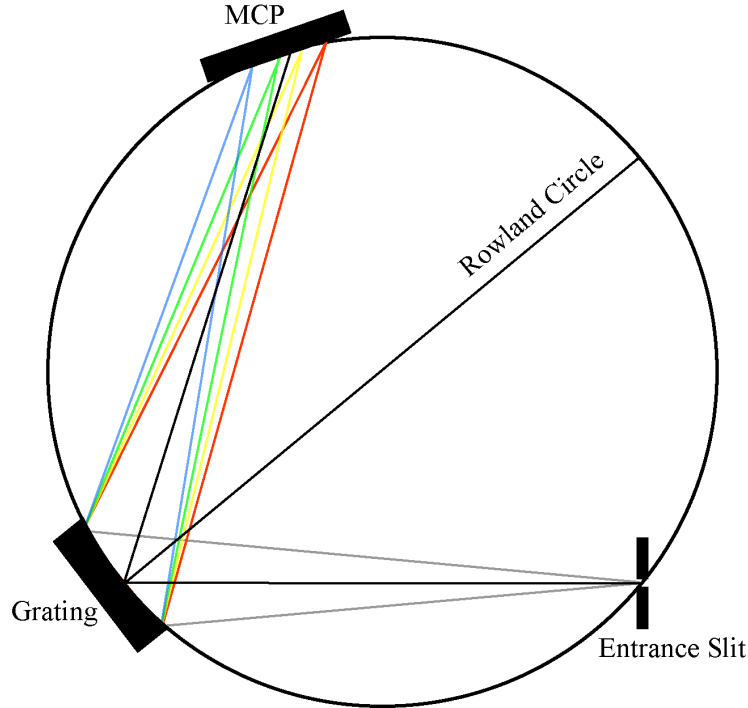


Figure 6.2: *Schematic drawing of the modified Acton Research VM-502.*

The principle setup is shown in Fig.6.2. The concave grating images the entrance slit onto the detector on the Rowland Circle [114] in a Seya-Namioka Geometry [115]. The detector consists of a CsI-coated Multi-Channel Plate (MCP) coupled to a phosphor screen which is imaged using a fiber taper and a 16-bit CCD camera. The wavelength incident on the MCP can be adjusted by rotating the grating which is realized by an external wavelength-calibrated controller. Thereby, different wavelength are imaged to different positions on the MCP. By the use of a large area MCP a spectral range of 50 nm can be acquired in a single shot, through the expense of the spectral resolution, since the MCP is flat and therefore does not

account for imaging on the Rowland circle. Nevertheless, the spectral resolution is still sufficient to obtain high quality spectra of the individual harmonics.



# Part III

## Experiments





# Chapter 7

## Ion Acceleration with linearly polarized Laser Pulses

In this chapter experiments on ion acceleration from ultra-thin foils of thicknesses ranging from  $5\text{ }\mu\text{m}$  down to  $2.9\text{ nm}$  are presented. The targets were irradiated by linear polarized pulses of  $45\text{ fs}$  FWHM duration focussed to a peak intensity of up to  $5 \times 10^{19}\text{ W/cm}^2$ . Additionally, the spectral properties of the transmitted laser pulse are analyzed. Parts of the results presented in this chapter have been published in [10].

### 7.1 Experimental Setup

The experiments were performed at the MBI - TW Ti:sapph laser of central wavelength  $810\text{ nm}$  delivering  $1.2\text{ J}$  in  $45\text{ fs}$  FWHM pulses with an ASE contrast ratio smaller than  $10^{-7}$  up to  $\sim 10\text{ ps}$  prior to the arrival of the main peak. By means of a re-collimating DPM 5.3, this contrast was increased by estimated four orders of magnitude (Ch. 5.3), which is essential for the suppression of pre-heating and expansion due to the pulse background. The energy throughput of this DPM system was in the order of  $60\text{--}65\%$ , resulting in pulse energies of  $0.7\text{ J}$ . Finally, the laser pulse was focused on Diamond-Like-Carbon (DLC) target with a  $f/2.5$  parabolic mirror down to  $6\text{ }\mu\text{m}$  diameter and is diffraction limited by  $30\%$  under normal incidence. This corresponds to a peak intensity of  $2.6 \times 10^{19}\text{ W/cm}^2$  or a normalized vector potential of  $a_0 = 3.6$ . For a second set of experiments the focussing procedure was improved, leading to a focus diameter of  $3.6\text{ }\mu\text{m}$  and therefore a peak intensity of  $5 \times 10^{19}\text{ W/cm}^2$  or  $a_0 = 5$ . The resulting ions were detected with a MCP coupled to a Thomson-Parabola as described in Ch. 6.1. Additionally, the transmitted laser pulse was registered with a 12-bit optical grating spectrometer.

DLC targets of thicknesses ranging from  $2.9\text{--}50\text{ nm}$  were used, having a density

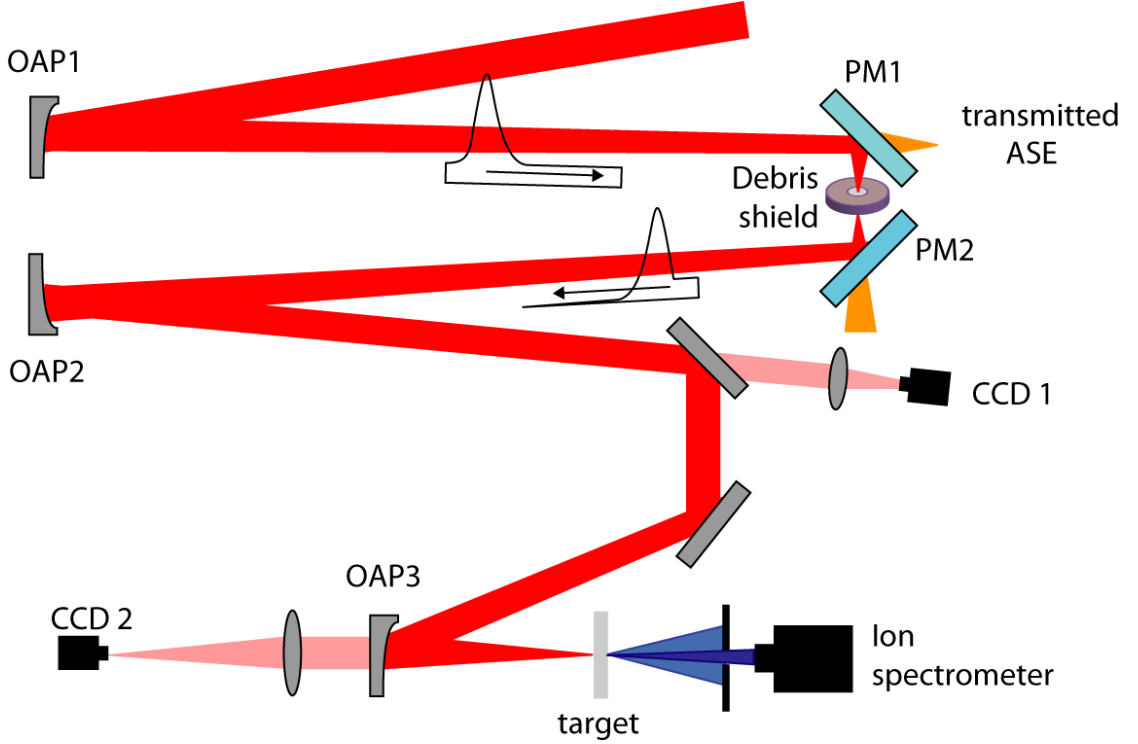


Figure 7.1: *Setup of the experiment: The first off-axis parabolic mirror (OAP1) focuses the incoming beam (red) between the two plasma mirrors (PM1, 2). Then it is re-collimated by OAP2. Afterwards it is directed to the final target chamber, where it is focussed by OPA3 on the target. The emerging ion beam (blue) is analyzed and detected by a Thomson-Spectrometer and a MCP (Ch. 6.1).*

of  $2.7 \text{ g/cm}^3$ . Owing to the high fraction of  $\text{sp}^3$ -, i.e. diamond-like bonds of  $\sim 75\%$ , DLC offers unique properties for the production of mechanically stable, ultra-thin, free standing targets, such as exceptionally high tensile strength, hardness and heat resistance. The thickness of the DLC foils was characterized by means of an atomic force microscope (AFM), including the hydrocarbon contamination layer on the target surface which was present during the experiments [116]. In addition, in order to precisely determine the structure of the contamination layer, the depth-dependend composition of the foil was measured via Elastic Recoil Detection Analysis (ERDA) [116]. From these measurements we obtain a thickness of  $\sim 1 \text{ nm}$  for the hydrocarbon contamination layer. In the following the combined thickness of bulk and surface layer as it appears in the actual ion acceleration experiment presented is referred.

## 7.2 Transition from TNSA to Enhanced TNSA

As discussed in Ch. 3.1 the transition from the *TNSA* to the *enhanced TNSA* regime is characterized by a symmetric ion acceleration for both, front- and rear side of the target and by a dependence of the maximum ion energy from the target thickness. This dependence on the target thickness has been experimentally demonstrated by several groups exhibiting an optimum thickness around the Debye length  $\lambda_D$  (e.g. a few hundred nm) [21, 117–119]. The aspect of a symmetric acceleration lacks of an experimental proof so far and is the aim of the experiment presented in this chapter.

To record ion spectra simultaneously from the front- and the rear side of the target, the experimental setup (Ch. 7.1) had to be varied. The target was rotated to an angle of incidence of  $45^\circ$  and two ion spectrometers (Ch. 6.1) were placed in the target normal directions. Additionally, the incident intensity on the target was reduced to  $4 \times 10^{19} \text{ W/cm}^2$  ( $a_0 = 3.9$ ) for the shots without DPM and consequential to  $2.3 \times 10^{19} \text{ W/cm}^2$  ( $a_0 = 3.2$ ) with DPM. This enabled the use of Titanium targets as thin as  $1 \mu\text{m}$  without the use of the DPM.

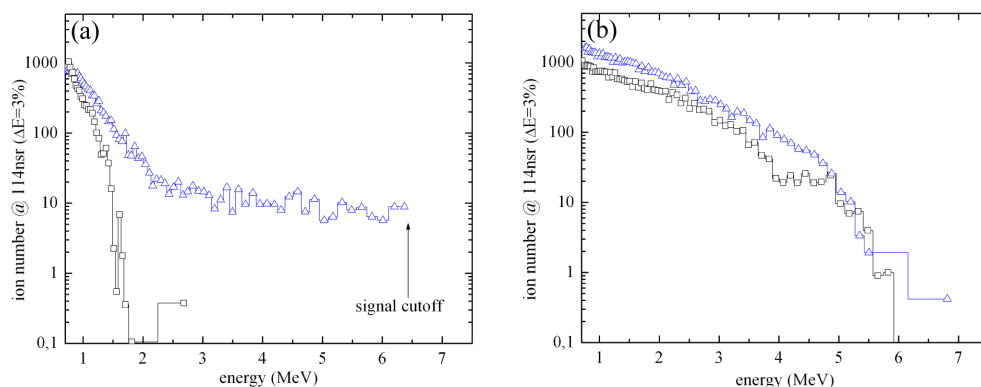


Figure 7.2: *Front side (black squares) and rear side (blue triangles) proton spectra obtained from laser driven  $1 \mu\text{m}$  Ti- foils when the intense driving laser pulse has a medium contrast (a) and an ultra-high contrast (b).*

In Fig. 7.2 typical front- and rear side proton spectra are shown. Obviously, the spectra obtained without DPM show a strong asymmetry between front- and rear side with a cut-off energy of  $< 2 \text{ MeV}$  for the front- and  $6.5 \text{ MeV}$  for the rear side. The rear side spectrum also consists of a plateau region between  $2 - 6 \text{ MeV}$  which approximately begins at an energy where the front-side spectrum has its

energy cut-off. On the other hand, the spectra recorded with the use of the DPM look almost identical concerning their maximum energy of 6 MeV and their overall spectral shape. Their difference in the number of ions is in the order of calibration of the used spectrometer setup itself (Ch. 6.1).

Together with measurement of the optimum thickness, obtained earlier [21, 109] this measurement undoubtedly represents the first experimental demonstration of ion acceleration in the *enhanced TNSA* regime.

### 7.3 Nonlinear Laser Pulse Transmission of a Thin Plasma Layer

Since the partial transmission of the intense laser pulse through an expanding target plays a decisive role to determine the dominant regime of ion acceleration [120–122], the opaqueness of the used foils is examined.

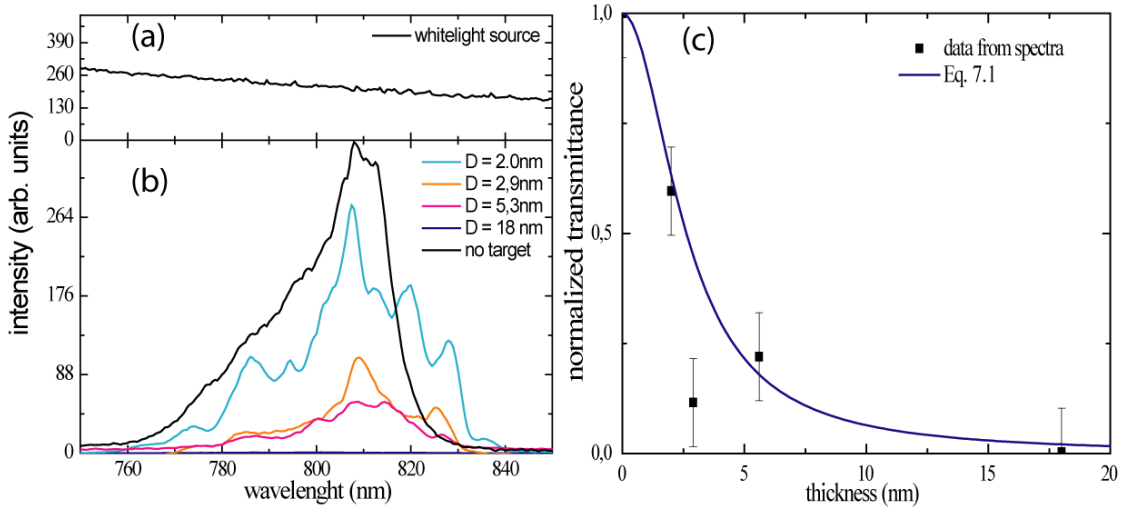


Figure 7.3: (b) Measured, calibrated laser pulse spectra in transmittance of the DLC foils. (a) shows the signal of a constant white light source used for calibration of the optical path. (d) The resulting transmittance ( $a_0 = 5$ ) of the DLC targets as a function of the target thickness obtained by numerical integrating the spectra of (b), compared to the analytical formula Eq. 7.1. The errorbars are given by the average shot-to-shot fluctuation.

For the experiments presented in this chapter the target rear side was imaged to a 12-bit optical grating spectrometer to (i) measure the transmittance of the

laser pulse through the foil and (ii) obtain the spectral properties of this nonlinear process. For calibration of the optical path and the spectrometer a commercial white light source delivering a constant intensity over a significant spectral range was introduced in the setup. In Fig. 7.3a the white light spectrum is shown which was used for calibrating the spectra shown in Fig. 7.3b.

Finally these calibrated spectra were numerically integrated to obtain the transmittance of the foils. To have an absolute measure of the transmittance, the shots were normalized to a shot without target. The experimental results for the transmission  $T$  are plotted along with the values expected by the analytical formula, here approximated for linear polarization [74, 123]:

$$T \cong 1/[1 + (\sigma/\bar{\gamma})^2]. \quad (7.1)$$

The experimental results are in agreement with the analytical model.

To decrease the target thickness below 2.9 nm, they were heated by a cw-laser with a powers in the range of 100 – 500 mW for several seconds resulting in foil temperatures of 1000 – 3000 K. Thereby it is assured that the water and hydrocarbon contamination layer is completely removed from the DLC foils. In fact, the ion spectra measured from these targets do not show any protons. Since the thickness of the contamination layer was determined to  $\sim 1$  nm, the obtainable minimum thickness was  $\sim 2$  nm.

The situation changes drastically when these pre-heated targets were used in the experiment. The targets are getting highly transparent and the spectrum (Fig. 7.3b) exhibits a strong modulation and is broadened significantly. To have a closer look at this feature, in Fig. 7.4 several spectra, obtained for a thickness of  $\sim 2$  nm are plotted. They demonstrate the whole bandwidth of the modulation and broadening at this thickness. The spectral broadening gives rise to the onset of pulse-shortening due to the non-linear interaction: The transmittance Eq. 7.1 is a function of the laser amplitude  $a_0$  and hence of the intensity. Thus, a small fraction associated with the most intense part of the laser pulse is transmitted, the rest reflected or absorbed. The transmitted pulse can therefore be much shorter than the incident pulse [124].

## 7.4 Maximum Ion Energies and Spectral Shape

The maximum detectable energy/nucleon ( $E_{\max}$ ) obtained for protons and fully ionized carbon ions  $C^{6+}$  is plotted as a function of the target thickness in Fig. 7.5 for two different laser intensities. The cut-off energies for both ion species exhibit a strong dependence on target thickness. In case of protons and  $a_0 = 5$ ,  $E_{\max}$  increases from around 7.5 MeV for a 40 nm foil up to 13 MeV for a 5.3 nm foil, while for  $C^{6+}$  the maximum energy rises from 26 MeV for use of a 40 nm foils

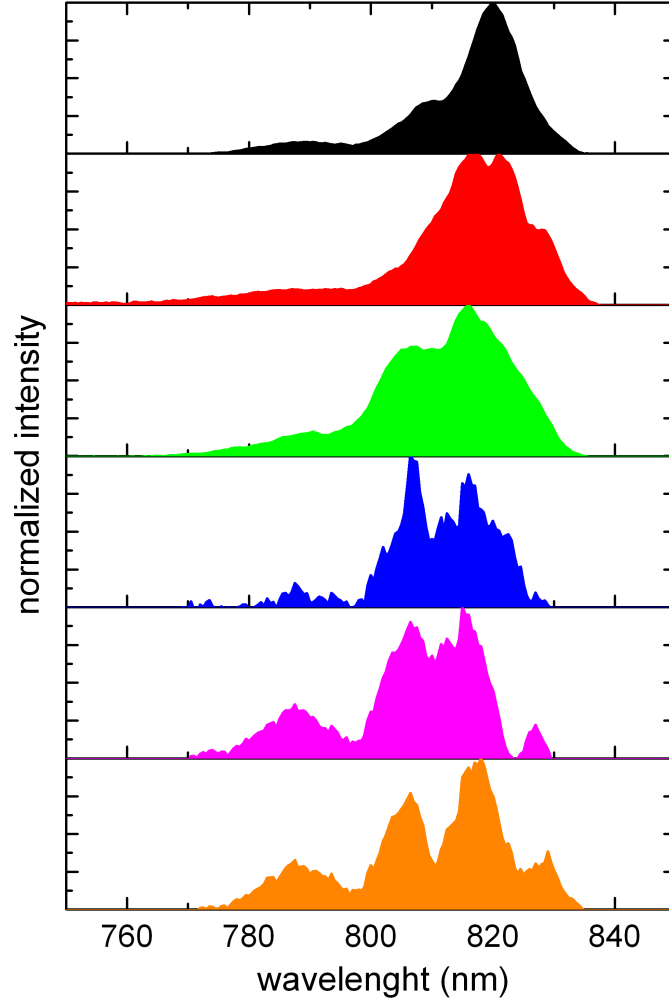


Figure 7.4: (b) Measured, calibrated laser pulse spectra in transmittance of the DLC foils with  $\approx 2\text{nm}$  thickness revealing a huge bandwidth of strong modulation and spectral broadening.

to 71 MeV for 5.3 nm. Taking into account the different  $Z/m_i$  values for protons and  $\text{C}^{6+}$  ions, they are both accelerated to the same velocity. Further decrease of the target thickness down to 2.9 nm results in a steep drop of the observed ion energies. The energy distributions of all species are continuous as expected.

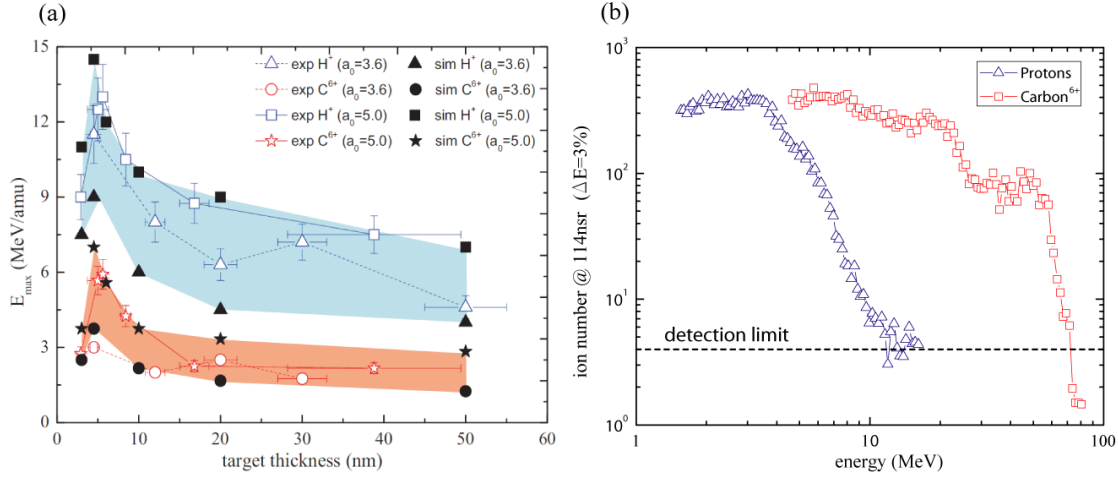


Figure 7.5: (a) Maximum energy per atomic mass unit for both protons and carbon ions plotted vs. foil thickness for a normalized laser vector potential of  $a_0 = 5$ . The experimental results are in excellent agreement with numbers deduced from 2D-PIC-simulations by X. Q. Yan<sup>1,2</sup>. (b) Typical ion spectrum obtained at a target thickness of 5.3 nm.

However, especially the observed carbon  $C^{6+}$  energy of 71 MeV reaches for the first time a range of values that were previously only accessible by large single shot Nd:glass laser systems with 30 – 50 J pulse energy [85, 125]. The shot-to-shot variations of 10 %, indicated by the error bars, arise mainly from fluctuations of the laser pulse itself and from macroscopic modulations of the target surface.

## 7.5 Conversion Efficiency

The conversion efficiency (Fig. 7.6b) was calculated by numerically convoluting the energy dependent divergence of the accelerated ion beam with the initially measured ( $a_0 = 5$ ) spectra. These values for the divergence (cf. inset in Fig. 7.6a) were extracted from PIC simulations and supported by experimentally obtained proton beam profiles using a stack of radiochromic film (RCF) layers. Comparing those to the divergencies of ion beams generated by other laser systems e.g. [126], the divergence is smaller and the linear dependence on the energy is reasonable in the considered high-energy part. The dependence of the CE on the target thickness is showing analogous characteristics to  $E_{\max}$  (Fig. 7.5). A sudden rise is observed

<sup>1</sup>Max-Planck-Institut für Quantenoptik, 85748 Garching, Germany

<sup>2</sup>State Key Lab of Nuclear Physics and Technology, Peking University, 100871 Beijing, China

when entering the laser transparency regime ( $D < l_s$ ) reaching 10.5 % for  $C^{6+}$  and 1.6 % for protons at the optimum thickness.

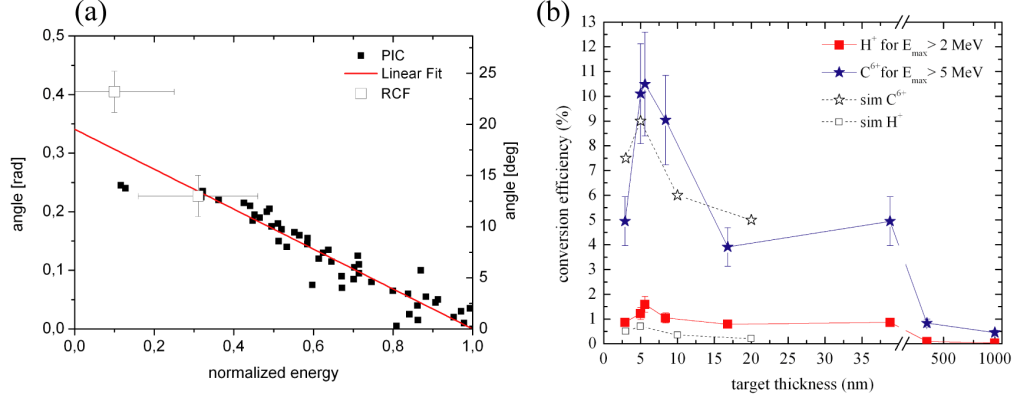


Figure 7.6: (b) Calculated CE for protons and  $C^{6+}$  ions as a function of the target thickness, based on a energy dependent divergence angle of the ion beam, which was extracted from PIC simulations by X. Q. Yan<sup>1,2</sup> and supported by measured beam profiles (a). The experimental data are in good agreement with the values of the CE obtained from PIC simulations.

The CE drops down to below 1% when the targets thickness reaches the TNSA dominated regime [39, 118].

## 7.6 Simulation

The experiments were compared to 2D-PIC simulations, where the laser pulse was modeled by a Gaussian shape in time with a FWHM of 16 laser cycles, a Gaussian intensity distribution in the focus with a FWHM spot size of  $4 \mu\text{m}$  and an  $a_0 = 5$  ( $a_0 = 3.6$ ). It interacts with a rectangular shaped plasma of initial density  $n_e = 500 \times n_c$  consisting of 90 % carbon ions and 10 % protons (in number density) to account for the presence of a contamination layer. The simulation box is composed of  $1200 \times 10000$  cells with 1000 particles per cell and a total size of  $(10 \times 20) \mu\text{m}^2$ . The total simulation time  $\tau$  given in laser cycles is 120 relative to  $\tau = 0$  when the laser pulse reaches the initial position of the target ( $x = 3\lambda$ ).

Fig. 7.5a shows that the simulated maximum proton energies as well as the carbon energies are in excellent agreement with the experimental data. In par-

<sup>1</sup>Max-Planck-Institut für Quantenoptik, 85748 Garching, Germany

<sup>2</sup>Sate Key Lab of Nuclear Physics and Technology, Peking University, 100871 Beijing, China



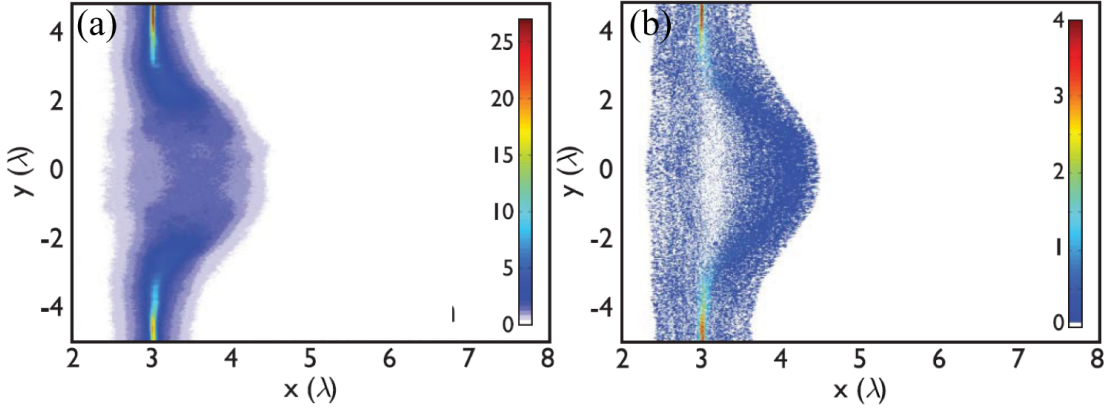


Figure 7.7: *Electron (a) and carbon ion (b) density distribution vs.  $x$  at time  $t = 40\tau$ . (Simulation courtesy of X. Q. Yan<sup>1,2</sup>)*

ticular, the optimum target thickness of 5.3 nm is reproduced. This thickness for the peak ion energy is consistent with the thickness given by the empirical relation  $\sigma_{opt} \approx 3 + 0.4 \times a_0$  that was found in multiparametric PIC-simulation studies by Esirkepov *et al.* [34]. For foil thicknesses below the optimum ( $\sigma < \sigma_{opt}$ ), the plasma becomes increasingly transparent (Fig. 7.3b) and the pulse is more transmitted than absorbed. Due to the low number of electrons in the focal volume ( $\sim 10^{11}$ ) their electric current is no longer sufficient to (i) reflect the laser pulse and (ii) to establish an effective longitudinal charge separation field. This results in a sudden drop in ion energies and 50 % of the CE (the same amount as the reduction of the target thickness), as it was observed in the experiment (Fig. 7.5+7.6). In case of  $\sigma > \sigma_{opt}$ , the laser intensity is not sufficient to generate the maximum possible displacement of all electrons within the focal volume which gives rise to a decrease in the longitudinal charge separation field. Note that the optimum thickness for ion acceleration predicted theoretically and observed experimentally is much smaller than previously used target thicknesses.

To illustrate the underlying ion acceleration mechanism in Fig. 7.7a,b detailed electron and carbon densities after 40 laser cycles as a function of the laser propagation direction  $x$  and the transverse coordinate  $y$  in units of the laser wave length  $\lambda_L$  are depicted. It is immediately striking that ions are accelerated strongly asymmetric, heavily favoring the direction of laser propagation. This is in strong contrast to the model based on the self-consistent solution of the Poisson equation presented in [61] which predicts a symmetric acceleration that happens primarily

<sup>1</sup>Max-Planck-Institut für Quantenoptik, 85748 Garching, Germany

<sup>2</sup>State Key Lab of Nuclear Physics and Technology, Peking University, 100871 Beijing, China

after the end of the laser pulse. From Fig. 7.7a,b it can be seen that the carbon ions are accompanied by co-moving electrons which accelerate the ions in forward direction.

## 7.7 Summary and Discussion

In summary, the experiments using laser pulses of ultra-high contrast presented in this chapter demonstrate increased values for the highest ion energies, two times in case of protons (13 MeV) and 20 times for carbon ions (71 MeV) if comparing to experiments performed with approximately the same laser parameters. It shall be noted that for the generation of 70 MeV carbon ions so far huge single shot Nd:glass laser facilities with pulse energies of (20–50) J were needed. And although conducted in single-shot mode, the limitation of repetition rate is principally given by the laser system which operates with 10 Hz.

Additionally the conversion efficiency from laser- to kinetic energy of the accelerated ions was improved more than 3 – 10 times for protons (1.6 %) and  $\approx 100$  times for carbon ions (10%).

A strong dependence of the resulting maximum energies on target thickness was primarily observed experimentally, with a pronounced optimum for an initial foil extension of 5.3 nm which is in good agreement with empirical scaling laws (Eq. 3.2) reduced from PIC simulation [34]. The experimental results are in excellent agreement with 2D-PIC simulations which also reveal that the ions are accelerated strongly asymmetric, heavily favoring the direction of laser propagation in contradiction to the regime of *enhanced TNSA*.

In addition, previously published *TNSA* scaling laws based on analytical models fail to interpret these results: The isothermal fluid model [39] does not predict an optimum target thickness, moreover it only predicts an maximum ion energy of  $\sim 1$  MeV for our parameters. More generally in the *TNSA* scheme, a dependence on the target thickness is only given due to the transversal spreading of the electrons at the rear side of the foil [40]. This is neglectable if comparing foil thicknesses between 2 – 50 nm. The model of *enhanced TNSA* (Ch. 3.1) [61] predicts also an optimum thickness but fails to explain the results on the maximum ion energy and its position with respect to the target thickness and the nature of the sharpness of the maximum around several nm, when the target becomes transparent for the incident laser.

Furthermore, the opaqueness of the used foils were examined. Here, the measured transmission is in good agreement with the values calculated analytically [74]. The spectral shape of the transmitted light includes strong modulations and exhibits a significant spectral broadening and hence the beginning of the generation of ultra-short transmitted pulses [124] suggesting the use of double targets [127].

In conclusion, the results of the experiments with linear polarization constitute the onset of the laser radiation pressure participating in the acceleration process which is indicated by:

- (i) Protons and  $C^{6+}$ -ions are accelerated to the same velocities.
- (ii) The spectral shape of the  $C^{6+}$ -ion at the optimum thickness shows signatures of modulation.
- (iii) The acceleration is strongly asymmetric favouring the laser propagation direction.
- (iv) The measured maximum ion energies and the conversion efficiency as well as the position of the peak energies with respect to the target thickness can not be explained by any theoretical model in the *TNSA* scheme.

To reveal the influence of the radiation pressure on ion acceleration, experiments with circular polarization were carried out and are presented in Ch. 8.



# Chapter 8

## Ion Acceleration in the Radiation Pressure Dominated Regime

In order to emphasize the influence of the laser radiation pressure on the ion acceleration process the laser polarization is changed to circular [35, 63–69, 128, 129]. As discussed in detail in Ch. 3.2 the absence of the longitudinally oscillating component in the Lorentz force (Ch. 1) leads to a suppression of electron heating. Instead, the electrons are compressed to a highly dense electron layer piling up in front of the laser pulse which in turn accelerates ions. By choosing the laser intensity, target thickness and density such that the radiation pressure equals the restoring force given by the charge separation, i.e. the conditions given by Eq. 3.12, the whole target foil in the focal volume propagates ballistically as a quasineutral plasma bunch. This *flying mirror* (Ch. 3.2.2) is gaining less momentum in favor of more energy from the laser field as it is accelerated. As long as the electron temperature is kept low, the acceleration can be maintained, and the process is expected to lead to very high conversion efficiencies and ion energies scaling linearly with laser intensity in contrast to TNSA where the ion energy is proportional to the square root of the laser intensity. In this scenario, all particle species are accelerated to the same velocity, which intrinsically results in a monochromatic spectrum with the energy given by Eq. 3.21. The results have been published in [11].

### 8.1 Experimental Setup

The experiments described in this chapter were also carried out at the MBI - TW Ti:sapph laser system as introduced in detail in Ch. 5. DLC foils of thicknesses  $D = 2.9 - 40$  nm were placed in the focal plane at normal incidence. Furthermore, the experimental setup shown in Fig. 7.1 was extended by a mica crystal operating as

$\lambda/4$  plate placed into the beam path behind the plasma mirror to change the laser polarization from linear to circular. In addition, a magnetic electron spectrometer with a solid angle of  $\sim 2 \times 10^{-4}$  sr equipped with Fujifilm BAS-TR image plates was positioned behind the target at an angle of  $22.5^\circ$  with respect to the laser axis.

## 8.2 Maximum Ion Energies and Spectral Shape

The obtained maximum ion energies per atomic mass unit plotted over the target thickness  $D$  are shown in Fig.8.1a. Compared to linearly polarized irradiation, the maximum energies of proton and carbon are lower but a dependence on the initial foil thickness is still observable, with an optimum at  $D = 5.3$  nm with maximum energies for protons and carbon ions of 10 MeV respectively 45 MeV. The theoretically obtained optimum foil thickness  $D = 2$  nm, given by Eq.3.12 was reproduced experimentally by the same order of magnitude.

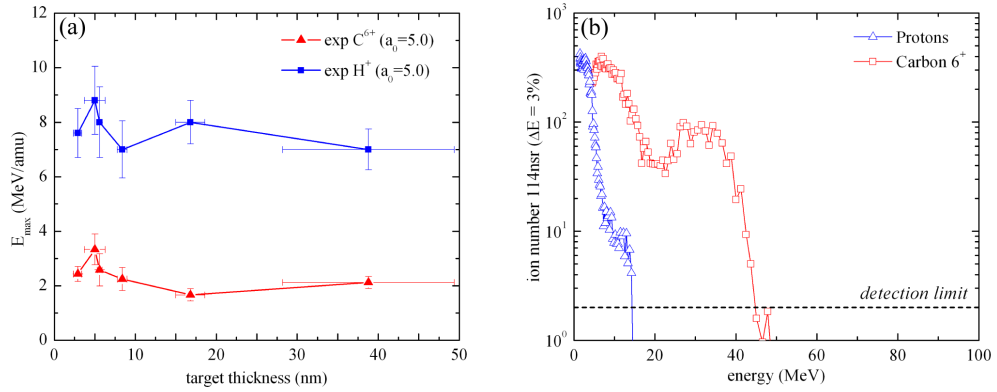


Figure 8.1: (a) Experimentally observed maximum proton (blue) and carbon  $C^{6+}$  (red) energies per atomic mass unit over target thickness for circular polarization and (b) the spectra corresponding to a thickness of  $D = 5.3$  nm.

The corresponding electron spectra for  $D = 5.3$  nm are shown in Fig.8.2. It can be clearly seen that circularly polarized irradiation results in a pronounced reduction in the number of highly energetic electrons as expected. To illustrate the consequent impact on the acceleration of ions, experimentally observed proton and carbon spectra are plotted in Fig.8.1b at the experimentally observed optimum foil thickness. A monotonically decaying spectrum is obtained for protons comparable to the case of linear polarization in Fig.7.5. In contrast, in case of circular polarization the spectrum of fully ionized carbon reveals two components.

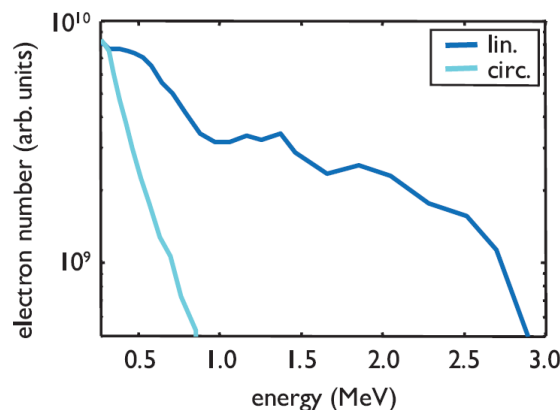


Figure 8.2: *Measured electron spectra at the optimum target thickness  $D = 5.3$  nm showing a strong reduction in electron heating for circularly polarized irradiation.*

In addition to the continuously decreasing low energetic ion population reaching up to  $\sim 20$  MeV, a distinct peak is observable around  $\sim 30$  MeV. To compare the experimental findings to the model approximations in Ch. 3.2.2 the target thickness of  $(5.3 \pm 1)$  nm has to be introduced into Eq. 3.2, and Eq. 3.23 and Eq. 3.21 have to be evaluated, resulting in an energy of  $E = (20 \pm 10)$  MeV. This is in agreement with the experimentally observed value. If only the thickness of the DLC is considered (without contamination), i.e.  $D = 4.3$  nm the resulting energy is in excellent agreement with the experimental data.

This spectral peak experimentally only occurs at a thickness of  $D = 5.3$  nm and circular polarization, whereas the the shape of the proton spectrum was not affected.

## 8.3 Simulations

To substantiate the experimental results further, two-dimensional PIC simulations were carried out. The parameters were the same as described in Ch. 7.6 but the polarization was changed to circular.

To account for the small solid angle of the Thomson spectrometer (cf. 6.1), only particles propagating in forward direction with a cone of half angle 0.01 rad were considered for simulated spectra of Fig. 8.3. An isolated quasi-monoenergetic peak emerges at the end of the laser target interaction at  $t = 45$  fs.

The corresponding carbon ion phase space shows a significant amount of particles located in a discrete area, constituting a rotating structure. The series of loops originate from the continuing front side acceleration and ballistic evolution of the

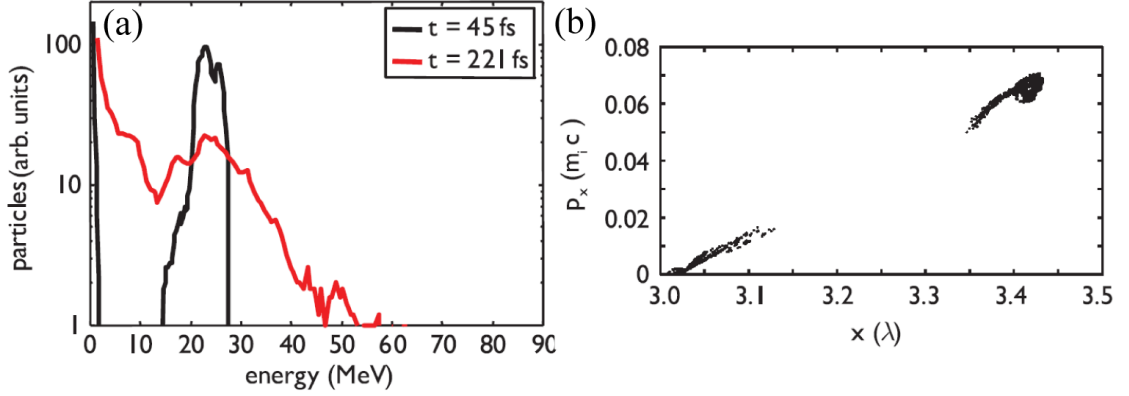


Figure 8.3: (a) Temporal evolution of the  $C^{6+}$  ion spectrum in case of circular polarized irradiation of a 5.3 nm thickness DLC foil obtained from 2D PIC simulation (Simulation courtesy of X. Q. Yan<sup>1,2</sup>.)

target and thus giving a clear evidence of radiation pressure being the dominant acceleration force [35, 64–67] as described in Ch. 3.2.1.

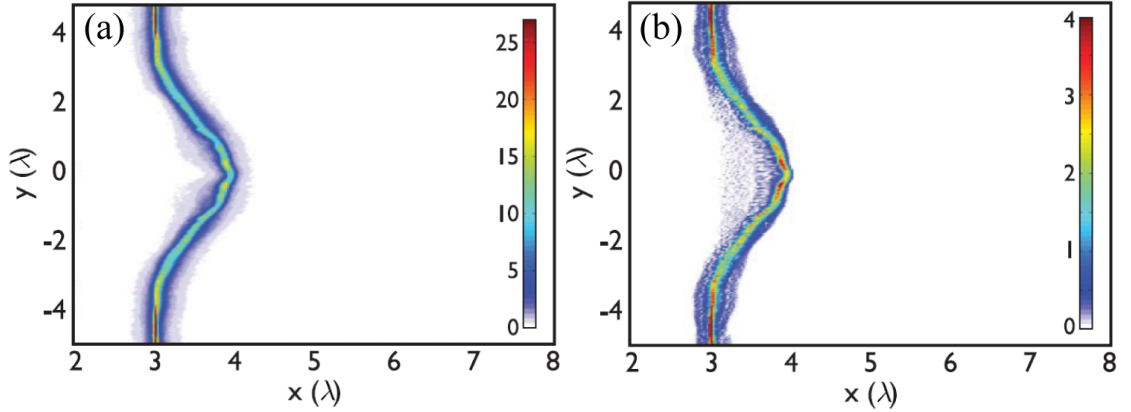


Figure 8.4: Electron (a) and carbon ion (b) density distribution vs.  $x$  at time  $t = 40\tau$  (Simulation courtesy of X. Q. Yan<sup>1,2</sup>.)

The difference becomes striking when comparing the acceleration dynamics by examining the electron and carbon density distributions observed in the simulation (Fig. 8.4) and comparing them to the ones obtained with linear polarization

<sup>1</sup>Max-Planck-Institut für Quantenoptik, 85748 Garching, Germany

<sup>2</sup>State Key Lab of Nuclear Physics and Technology, Peking University, 100871 Beijing, China



(Fig. 7.7). In the case of circular polarization, the electron population maintains in its structure as a thin layer of high density being pushed by the laser in forward direction. Consequently, the carbon ions co-propagate with the compressed electrons and the whole focal volume is accelerated as a quasi-neutral dense plasma bunch by the laser radiation pressure.

However, the isolated quasi-monoenergetic peak in the carbon spectrum at the end of the laser-target interaction does not preserve its shape upon further propagation (Fig. 8.3). Even though the apex energy stays constant, the spectral shape is broadened and partially merges with the low energy ion population which still gains energy after the end of the laser pulse (Ch. 3.1). This results in a spectral shape comparable to the one observed experimentally (Fig. 8.1). This is attributed to the considerable deformation of the foil plasma by the focussed Gaussian laser (Fig. 8.4). Therefore, the laser is incident on a bent surface, particularly at the end of the interaction. Thus, electric field components perpendicular to this moved surface are present. Those efficiently heat the electrons in those regions (Ch. 2.3) and cause the peak in the carbon spectrum to broaden as well as the energy gain of the ions at the low energy part of the spectrum. Additionally, this makes the detection of the peak in the proton spectrum which is, since all ions move at the same velocity expected around 2.5 MeV, impossible since it vanishes in the low energy part of the spectrum.

## 8.4 Summary and Discussion

In this chapter experimental investigations on ion acceleration from nanometer thin DLC foils irradiated by circularly polarized, highly intense laser pulses were presented. A strong reduction in number and energy of hot electrons was observed when compared to linear polarization. As a result a pronounced peak in the carbon  $C^{6+}$  centered around 30 MeV at the optimum foil thickness of 5.3 nm was observed. The measured optimum thickness is on the same order as the one predicted analytically by Eq. 3.12. The central energy of the peak is in good agreement with analytical result taking into account the partial transmittance of the target (Eq. 3.23). Two-dimensional PIC simulations give a clear evidence that those ions are for the first time dominantly accelerated by the laser radiation pressure. Being recently widely studied in theory, the comparative measurements provide the first experimental proof of the feasibility of radiation-pressure acceleration to become the dominant mechanism for ion acceleration when circular polarization is used. Additionally, a strong denting of the target foil during the interaction was observed which results in a spectral broadening of the peak in the carbon spectrum in time and a late energy gain of the ions in the low energy part of the spectrum. In the near future, this might be compensated by properly shaping the laser focal spot

distribution [130] or by shaping of the foil targets itself [131].

However, this is the approach for the next chapter, where the denting and the expansion of the target is examined by analyzing the generated harmonic radiation in the interaction process.

## Chapter 9

# High-Harmonic Generation in Ultra-Thin Foils

In this chapter, the dynamics of foil targets with thicknesses on the nanometer scale irradiated with laser pulses of relativistic intensities is examined by means of the generation of surface high harmonics (SHHG). Their analysis allows the in-situ extraction of the electron density at times when the peak of laser pulse interacts with the plasma target, which is of utmost interest for laser ion acceleration in the RPA regime as presented in Ch. 8. The key to efficient RPA is to suppress the heating of the target electrons and carefully control the targets areal density. It will be shown that the SHHG on the front surface of a nm-scale foil detected in transmission, allows detailed studies of the crucial interaction parameters such as target deformation and plasma density when the peak of the driving laser pulse interacts with the target, i.e. while the ion acceleration takes place. In addition, the first observation of odd-numbered relativistic harmonics is verifying a predicted property of harmonics originating from solid targets [24] and thereby advance the understanding of the harmonic generation process itself.

As discussed above two distinct mechanisms capable of generating high-order harmonics in transmittance of nm-scale foils have been identified [86]. For sub- and weakly relativistic intensities corresponding to a normalized vector potential  $a_0$  below or on the order of unity harmonics are generated via CWE (Ch. 4) in the density gradient on the rear side of the foil. These plasma waves are excited indirectly by attosecond-electron bursts propagating up the rear side plasma density gradient. For higher intensities ( $a_0 \gg 1$ ) harmonic radiation can also be emitted by plasma electrons close to the critical density which oscillate coherently with velocities close to the speed of light in the driving laser field [23, 24, 80]. In the case of very thin targets this mechanism can also generate harmonics emitted in the forward direction that propagate in forward- (laser propagation-) direction [85, 86]. To determine the predominant mechanism in a specific experiment one can ana-

lyze the characteristics of the detected harmonic spectrum. The main differences are: (i) Relativistic harmonics exhibit an spectral cut-off that is dependant on the laser intensity, while the CWE harmonic cut-off is determined by the maximum density in the target. (ii) CWE harmonics require oblique incidence, while in contrast relativistic harmonics can be also generated under normal incidence so that  $2\omega$  electron oscillations are driven by the  $\mathbf{v} \times \mathbf{B}$  component of the driving force (Ch.1). Parts of the results presented in this chapter have submitted for publication [12].

## 9.1 Experimental Setup

For the detection of the high harmonic radiation in laser propagation direction, a spherical mirror with unprotected gold coating was positioned under an angle of 45 degrees behind the DLC targets ranging from 5.3 to 30 nm in thickness, which were irradiated in the same setup as described in Ch.7.1 with an intensity of  $2.6 \times 10^{19}$  W/cm<sup>2</sup> or a normalized vector potential of  $a_0 = 3.6$ . The resulting line focus was placed on the entrance slit of a normal incidence ACTON VM-502 VUV spectrometer equipped with a MCP detector and a fiber-coupled CCD-camera (Ch.6.2). The spectrometer allowed the detection of radiation from 140 down to 50 nm corresponding to harmonics 7 to 16 of the fundamental laser wavelength.

## 9.2 Dynamics of Nanometer-Scale Foil Targets

In Fig.9.1 typical, normalized harmonic spectra obtained from targets with different thicknesses are plotted. They show odd and even harmonics with a pronounced enhancement of the odd harmonics (7th and 9th) independent of the initial target thickness. The spectra exhibit a strong dependance of the highest harmonic generated on the initial target thickness. While the spectrum from the thinnest (5.3 nm) targets has a cut-off at the 9th harmonic order, harmonics up to the 15th were generated from the 16 nm targets.

Actually, the cut-off in case of 30 nm targets was not resolvable with the used spectrometer setup, i.e. is  $> 16$ th order (not shown here).

These spectral properties suggest that the harmonics are generated by two different mechanisms, one generating predominantly odd harmonics originating from the central part of the focal region and one producing all harmonics from regions off central where the laser intensity is lower: The dependance of the harmonic cut-off on the target thickness and moderate intensities on the sides of the Gaussian focus give rise to a generation of this part of the spectrum by CWE as described in Ch.4. This means that the target has to be dented significantly to facilitate

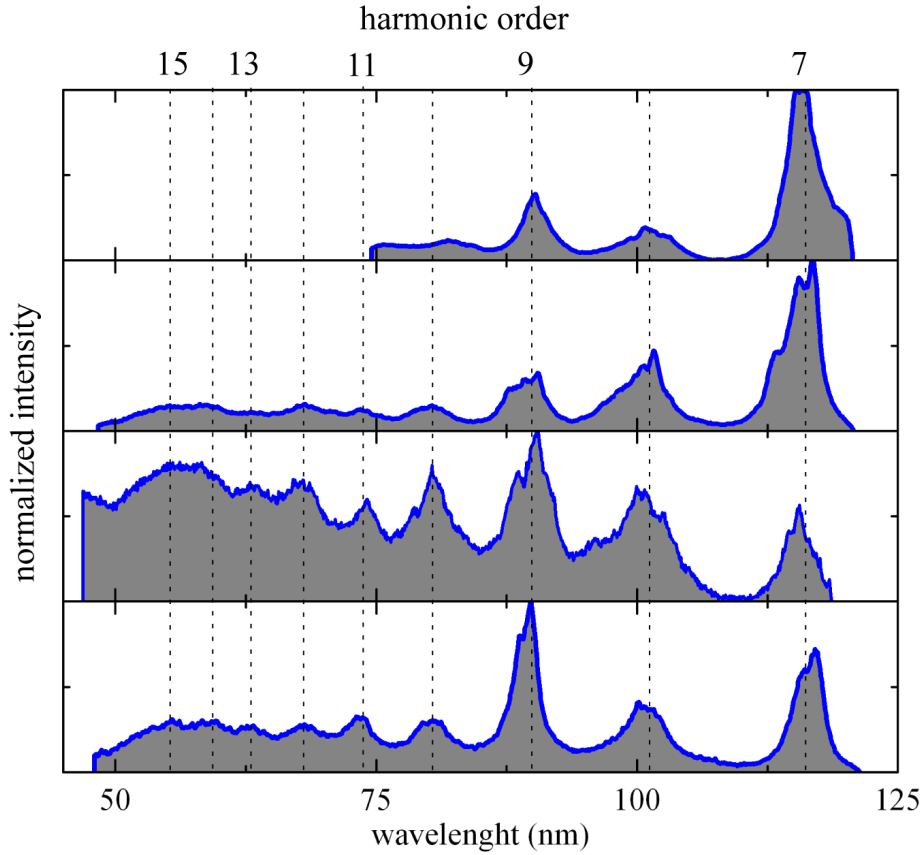


Figure 9.1: *Measured high harmonic spectra with linear laser polarization from targets with different thicknesses. From top to bottom: 5.3 nm, 8 nm, 12 nm and 16 nm.*

motion of the plasma electrons in and out of the surface in the electric field of the laser, i.e. to provide a surface which is perpendicular to the electric field of the laser and hence fulfil the requirements for the generation of CWE harmonics.

The fact that higher order CWE harmonics are generated from thicker targets corresponds to an expansion of the target, since the harmonic cut-off is determined by the the peak electron density (Eq. 4.1). In Fig. 9.2b the cut-off harmonic order and the corresponding peak electron density are plotted versus the original thickness of the target foil. The peak density in the interaction region as inferred from the harmonic generation during the most intense phase of the interaction, increases with the initial target thickness.

To model the expansion of the foil after ionization, a uniform energy deposition in the foil is assumed [21]. The ion sound velocity rapidly increases over a time

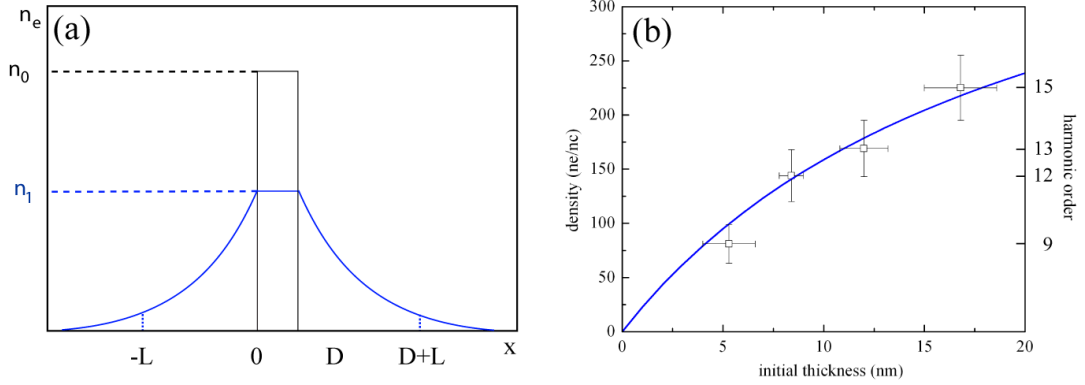


Figure 9.2: (a) Model of an exponential foil expansion and the resulting densities and cut-off harmonics as a function of the target thickness (b). The blue lines corresponds to the density expected from an exponential expansion with a scale length of 16 nm on each side.

of 70 fs to approximately  $c_{s,peak} = 5 \times 10^7$  cm/s corresponding to a hot electron temperature of  $T_e \approx 5$  keV [14] at which the plasma becomes non-collisional under the given experimental conditions (Ch. 2.3). The average sound velocity is then  $c_{s,mean} = 2.2 \times 10^7$  cm/s which results in an exponential expansion with a scale length of  $L = 15.4$  nm. The corresponding electron density  $n_1$  calculates to

$$n_1(D) = n_0 D \left( D + 2 \int_0^L e^{-x/L} dx \right)^{-1}, \quad (9.1)$$

where  $n_0 = 480 \times n_c$  is the initial density of the DLC targets. In Fig. 9.2  $n_1(D)$  is plotted along with the experimental data demonstrating a good agreement. Thus, in addition to the determination of the target density, the experiment gives information about the target heating prior to the relativistic interaction and demonstrates a fundamental limitation of the nm-foil density at the instance of the interaction with the peak of the laser pulse which can be crucial when even thinner targets are employed.

The information about the target heating can be used to further substantiate the argumentation of a reduction of the electron heating when the laser polarization is changed to circular (Ch. 8), which has been proven by comparing the electron spectra of both polarizations. In Fig. 9.3 a typical harmonic spectrum from a target with a thickness of 5.3 nm and circular polarization is shown. The density

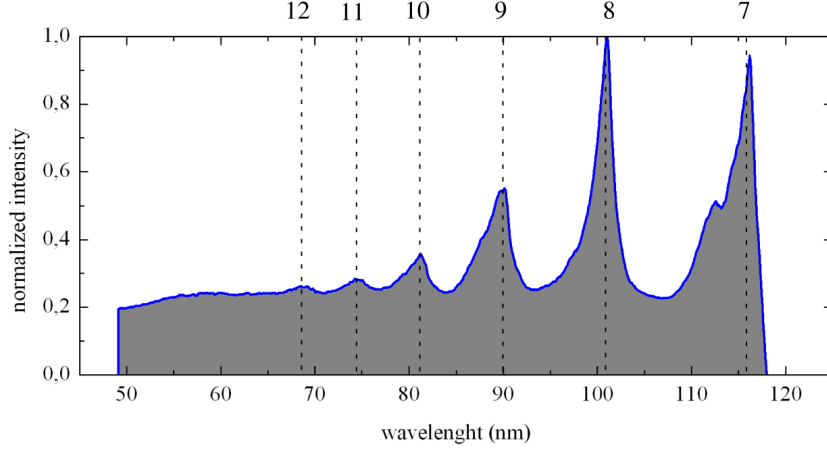


Figure 9.3: *Measured high harmonic spectrum with circular laser polarization from targets with a thickness of 5.3 nm in laser propagation direction. The 7th harmonic is already on the edge of the detector.*

corresponding to the highest harmonic (12th) is approximately two times higher compared to linear polarization. Additionally, the spectrum does not show an enhancement of the odd harmonic order 7 and 9 which certainly is attributed to the absence of  $\mathbf{v} \times \mathbf{B}$  component.

### 9.3 Simulations

To verify the argumentation that the pronounced enhancement of the odd harmonics (7th and 9th) independent of the initial target thickness is attributed to the  $\mathbf{v} \times \mathbf{B}$  component of the driving force, i.e. to a relativistic driver 2D PIC simulation were conducted by S. Rykovanov<sup>1</sup> using the code PIGWIG [132].

As discussed above even for ultra-clean Gaussian laser pulses, nm-scale targets expand during the rising edge of the 45 fs pulse with an  $a_0 = 3.6$ . Hence, the simulations were initialized using a triangular density profile with a peak intensity of  $n_e = 100 \times n_c$  and a linear ramp of 25 nm on each side. This corresponds to solid target with a thickness of 5 nm and a density of  $n_e = 480 \times n_c$ . The laser pulse was Gaussian both in space and time with a spot size of  $3 \mu\text{m}$  FWHM and a duration of 15 laser cycles FWHM and is incident normally onto the target. The size of the simulation box was  $6 \lambda$  in laser propagation and  $15 \lambda$  in polarization direction. The time step was  $\tau/400$  in laser propagation direction, where  $\tau$  is the period of the driving laser.

The results of the simulation shown in Fig. 9.4a where the electron density near

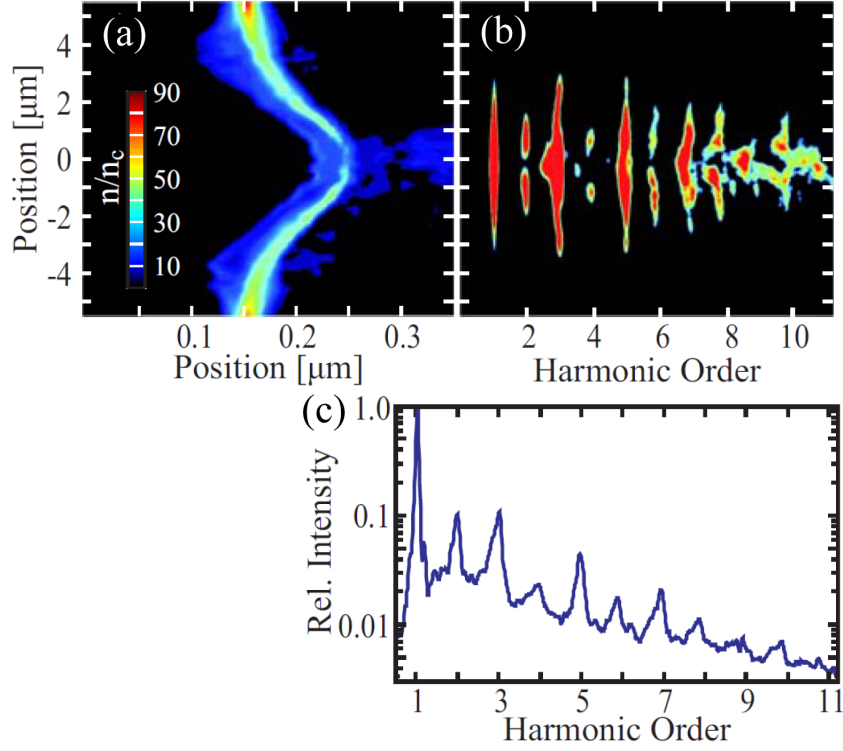


Figure 9.4: *Results of 2D PIC simulations by S. G. Rykovanov<sup>1</sup>. The electron density distribution (a) at the instance when the peak of the laser arrives at the initial target position and the time integrated harmonic spectrum (b) emitted in forward direction. The radially integrated spectra of (b) are shown in (c).*

the instance when the peak of the pulse interacts with the target is shown together with the resulting spectrum. The integrated spectrum contains all harmonic orders but an enhancement of odd harmonics originating from the center of the generation region is visible constituting a signature of relativistic harmonic generation on axis.

## 9.4 Summary and Discussion

In conclusion the experiments presented in this chapter constitute the first experimental demonstration of High Harmonic Generation in transmittance of nm-scale foils targets irradiated at normal incidence. High harmonics were generated by two different mechanisms in different regions of the laser focus. A denting of the

<sup>1</sup>Fakultät für Physik, Ludwig-Maximilians-Universität München, 80333 München, Germany



target leads to effectively oblique incidence of the driving laser on the sides of the laser focus and the generation of all harmonics. Only odd-numbered harmonics are generated exactly on the laser axis, which constitutes the first demonstration of relativistic harmonic generation at normal incidence, a feature which disappears as expected when circular laser polarization is used. In the regions of oblique incidence the harmonics are generated by Coherent Wake Emission. This allows the determination of the instantaneous target density of the foil at times where the relativistic interactions start to be significant. The obtained densities are in good agreement with a one dimensional expansion of the foil targets and are reduced by a factor of two when the laser polarization is changed to circular.

Hence, the experiments demonstrate that this method is a powerful diagnostic which can be employed in many experimental scenarios, e.g. laser particle acceleration as described in Ch. 7 and 8, without any changes in the existing particle acceleration experiments.



# Summary and Outlook

During the course of this thesis, novel, improved approaches for ion acceleration with high intensity laser pulses were explored and characterized. Laser pulses with relativistic intensities and an ultra-high contrast enabled the employment of targets with thicknesses below the skin-depth of the laser and hence, transparent targets. The first experimental results together with their theoretical interpretations of *Ion Acceleration in the Laser Transparency Regime* mark an important step towards future applications of laser accelerated ion beams.

The presented results extend the common regime of *Target Normal Sheath Acceleration* (TNSA) where the laser energy is transferred to kinetic energy of a hot electron population at the front side of thick ( $\mu\text{m}$ ), opaque laser irradiated solid targets. These electrons traverse the target and set up a quasi-static electric field, that accelerates the ions. Due to the lateral spreading of the hot electrons, the conversion efficiency (CE) of ion acceleration in the TNSA regime is very low (typically  $\sim 1\%$ ) and their energy spectra exhibit an exponential shape as an imprint of the hot electron population. These properties make the ion beams accelerated within the TNSA regime inappropriate for most applications where a high number of ions in a tailored energy spectrum are required.

One possibility to overcome the limitations of TNSA is the use of targets with a limited mass. Inspired by PIC simulations [34] that predict an optimum foil thickness of only a few nanometer for the laser parameters available at the Max-Born Institut which is as well close to the optimum thickness for a dominant *Radiation Pressure Acceleration* (RPA) [66] if the laser polarization is changed to circular, free-standing *Diamond-Like-Carbon* (DLC) foils were employed as targets. They were developed and characterized by collaboration partners within the Transregio SFB TR18 at the Ludwig-Maximilians-Universität München (LMU) and were available with thicknesses ranging from 2.9 – 50 nm. DLC offers unique properties for the production of mechanical stable, ultra-thin, free-standing targets, such as exceptionally high tensile strength, hardness and heat resistance.

To apply DLC foils as targets for the ion acceleration in the first place, the inherent laser pulse contrast, i. e. the intensity relation between the peak and the background of the laser pulse had to be enhanced significantly to suppress

pre-heating and expansion of the target. This nanosecond background of the femtosecond pulse originates mainly from *Amplified Spontaneous Emission* (ASE) in the amplifier crystals and was measured to be  $< 10^{-7}$  up to  $\sim 10$  ps prior to the main pulse.

In the frame of this work a re-collimating Double-Plasma-Mirror system was developed that is capable of increasing the contrast by estimated four orders of magnitude, while at the same time preserving the quality of the wavefront so that the laser pulse is focusable to a diameter of  $3.6 \mu\text{m}$ . The energy throughput was quantified to 60–65% resulting in pulse energies of 0.7 J and focus peak intensities of  $5 \times 10^{19} \text{ W/cm}^2$  at a pulse duration of 45 fs.

In contrast to thick foils typically employed for ion acceleration experiments within the TNSA regime, DLC foils of nanometer thickness become transparent under the interaction with an intense laser pulse and hence, the whole target in the focal volume is participating in the acceleration.

Besides the first experimental characterization of the non-linear transmittance of the relativistic laser pulses through the DLC targets that is in good agreement with the values calculated analytically [74], the major findings of this work are:

In case of linear laser polarization and normal incidence an optimum for ion acceleration was observed at a target thickness of 5.3 nm, accompanied by increased values for the highest ion energies: two times in case of protons (13 MeV) and 20 times for carbon ions (71 MeV) if comparing to experiments performed with approximately the same laser parameters. Additionally, the conversion efficiency from laser- to kinetic energy of the accelerated ions was improved  $\sim 100$  times for carbon ions (10%). Nevertheless, the spectral shape of the accelerated ion beam exhibits an exponential slope as an imprint of the hot electron population generated by the longitudinally oscillating component of the Lorentz force.

To suppress this electron heating, circular laser polarization was used in a second set of experiments. Then, the plasma electrons are piled-up to an equilibrium ahead of the laser pulse acting as a mirror that gains less momentum in favor of more energy when being accelerated as long as the electron heating is suppressed. The ions are therefore accelerated by a co-moving electric field to an intrinsically mono-energetic spectrum. This so-called *Radiation Pressure Accelerations* (RPA) has been explored in reams of publications during the last years by means of Particle-in-Cell simulations but lacked an experimental demonstration. The first experimental verification has been given by the experiments presented in this thesis. A strong reduction in number and energy of hot electrons was observed when compared to linear polarization. As a result a pronounced peak in the carbon  $C^{6+}$  centered around 30 MeV at the optimum foil thickness of 5.3 nm

was observed. Two-dimensional PIC simulations (by X. Q. Yan<sup>1,2</sup>) giving a clear evidence that those ions are for the first time dominantly accelerated by the laser radiation pressure. Moreover, a strong denting of the target foil was observed in the simulations which in turn is called to account for the exponential, low energy parts of the spectra obtained in the experiment.

To quantify this denting and the dynamics of the interaction experimentally, the high harmonic content of the transmitted laser radiation was examined for the first time. The high harmonics were generated by two different mechanisms in different regions of the laser focus. A denting of the target leads to effectively oblique incidence of the driving laser on the sides of the laser focus and therefore to the generation of all harmonics. Only odd-numbered harmonics are generated exactly on the laser axis, which constitutes the first demonstration of relativistic harmonic generation at normal incidence, a feature which disappears as expected when circular laser polarization is used. In the regions of oblique incidence the harmonics are generated by *Coherent Wake Emission*. This allows the determination of the instantaneous target density of the foil at times where the relativistic interactions start to be significant. The obtained densities are in good agreement with a one-dimensional expansion of the foil targets and are reduced by a factor of two when the laser polarization is changed to circular.

To avoid this denting will be in the focus of future investigations of ion acceleration in the Laser Transparency Regime. Since the denting has been quantified with the help of the experiments presented in this thesis, target fabrication labs will provide pre-shaped targets that are supposed to compensate the observed denting and hence sustain the RPA for longer times, resulting in higher ion energies. On the other hand *flat-top*, in favor of *Gaussian* spatial intensity distribution would be capable to avoid the denting as well. In addition, the mechanical target and plasma mirror engineering have to be improved to exploit the repetition of the laser system and hence, to pave the way for first applications. Since, number and energy of the accelerated ions presented in this thesis are sufficient, the repetition rate is the last obstacle for the exposure of cells (e. g. cancer cells).

Furthermore, experiments with the new dual beam line (30 TW + 100 TW at the Max-Born Institut will provide unique possibilities to conduct *Proton Imaging* experiments that will give a more detailed picture of the acceleration process in the Laser Transparency Regime as well as a whole variety of pump-probe experiments.

---

<sup>1</sup>Max-Planck-Institut für Quantenoptik, 85748 Garching, Germany

<sup>2</sup>State Key Lab of Nuclear Physics and Technology, Peking University, 100871 Beijing, China



# List of Figures

1.1	Laser interaction with a free electron . . . . .	8
2.1	Collisional Absorbtion . . . . .	14
3.1	Initial stage of RPA . . . . .	24
3.2	RPA 1D PIC Simulation . . . . .	25
3.3	Maximum ion energies is the Light Sail Regime . . . . .	28
5.1	Principle of CPA . . . . .	35
5.2	MBI TW Ti:sapph Laser . . . . .	37
5.3	Simulated Interferogram and its Fourier Transform . . . . .	38
5.4	Principle of the SPIDER . . . . .	39
5.5	SPIDER Measurement . . . . .	40
5.6	Contrast measurement with the 3rd order cross Correlator . . . . .	41
5.7	Double Plasma Mirror setup . . . . .	43
5.8	Incident beam profiles on the DPM surfaces . . . . .	44
5.9	Far-field Diagnostic of the DPM . . . . .	44
5.10	Reflectivity of the DPM system . . . . .	46
6.1	Typical ion spectrum from $5\mu\text{m}$ Titanium . . . . .	48
6.2	Acton Research VM-503 . . . . .	50
7.1	Experimental Setup . . . . .	56
7.2	Comparison between front- and rear side ion acceleration . . . . .	57
7.3	Transmittance of DLC targets . . . . .	58
7.4	Spectral properties of a laser transmitted through a DLC target . . . . .	60
7.5	Maximum ion energies for linear polarization . . . . .	61
7.6	Conversion efficiency . . . . .	62
7.7	Evolution of electron and ion densities for linear polarization . . . . .	63
8.1	Maximum ion energies for circular polarization . . . . .	68
8.2	Comparison of electron spectra . . . . .	69

---

8.3	Simulated electron spectrum and ion phase space plot . . . . .	70
8.4	Evolution of electron and ion densities for circular polarization . . .	70
9.1	HHG with linear laser polarization . . . . .	75
9.2	Exponential foil expansion and the resulting densities . . . . .	76
9.3	High harmonic spectrum with circular laser polarization . . . . .	77
9.4	Simulation of HHG from thin foils . . . . .	78



# Bibliography

- [1] T. H. Maiman. Stimulated optical radiation in ruby. *Nature*, 187:493, 1960.
- [2] D. Strickland and G. Mourou. Compression of amplified chirped optical pulses. *Optics Communications*, 56:219, 1985.
- [3] V. Yanovsky, V. Chvykov, G. Kalinchenko, P. Rousseau, T. Planchon, T. Matsuoka, A. Maksimchuk, J. Nees, G. Cheriaux, G. Mourou, and K. Krushelnick. Ultra-high intensity-300-tw laser at 0.1 hz repetition rate. *Optics Express*, 16:2109, 2008.
- [4] V. I. Veksler. Coherent principle of acceleration of charged particles. In *CERN Symposium on High Energy Accelerators and Pion Physics*, volume 1, page 80, Geneva, 1956.
- [5] G. J. Budker. Relativistic stabilized electron beam. In *CERN Symposium on High Energy Accelerators and Pion Physics*, volume 1, page 68, Geneva, 1956.
- [6] J. M. Dawson. Nonlinear electron oscillations in a cold plasma. *Physical Review*, 113:383, 1959.
- [7] T. Tajima and J. M. Dawson. Laser electron accelerator. *Physical Review Letters*, 43:267, 1979.
- [8] W. P. Leemans, B. Nagler, A. J. Gonsalves, C. Toth, K. Nakamura, C. G. R. Geddes, E. Esarey, C. B. Schroeder, and S. M. Hooker. GeV electron beams from a centimetre-scale accelerator. *Nature Physics*, 2:696, 2006.
- [9] R. A. Snavely, M. H. Key, S. P. Hatchett, T. E. Cowan, M. Roth, T. W. Phillips, M. A. Stoyer, E. A. Henry, T. C. Sangster, M. S. Singh, S. C. Wilks, A. MacKinnon, A. Offenberger, D. M. Pennington, K. Yasuike, A. B. Langdon, B. F. Lasinski, J. Johnson, M. D. Perry, and E. M. Campbell. Intense high-energy proton beams from petawatt-laser irradiation of solids. *Physical Review Letters*, 85:2945, 2000.

- [10] S. Steinke, A. Henig, M. Schnuerer, T. Sokollik, P. V. Nickles, D. Jung, D. Kiefer, R. Hoerlein, J. Schreiber, T. Tajima, X. Q. Yan, M. Hegelich, J. Meyer-ter Vehn, W. Sandner, and D. Habs. Efficient ion acceleration by collective laser-driven electron dynamics with ultra-thin foil targets. *Laser and Particle Beams*, 28:215, 2010.
- [11] A. Henig, S. Steinke, M. Schnuerer, T. Sokollik, R. Hoerlein, D. Kiefer, D. Jung, J. Schreiber, B. M. Hegelich, X. Q. Yan, J. Meyer-ter Vehn, T. Tajima, P. V. Nickles, W. Sandner, and D. Habs. Radiation-pressure acceleration of ion beams driven by circularly polarized laser pulses. *Physical Review Letters*, 103:245003, 2009.
- [12] R. Hoerlein, S. Steinke, A. Henig, S. Rykovanov, M. Schnuerer, T. Sokollik, D. Kiefer, D. Jung, T. Tajima, J. Schreiber, B. M. Hegelich, P. V. Nickles, M. Zepf, G. D. Tsakiris, W. Sandner, and D. Habs. Dynamics of nanometer-scale foil targets irradiated with relativistically intense laser pulses. <http://arxiv.org/abs/1009.1582>, 2010.
- [13] J. C. Maxwell. *A treatise on electricity and magnetism*, volume 1. Oxford : Clarendon Press, 1873.
- [14] P. Gibbon. *Short Pulse Laser Interactions with Matter - An Introduction*. Imperial College Press, 2005.
- [15] E. Lefebvre and G. Bonnaud. Transparency/opacity of a solid target illuminated by an ultrahigh-intensity laser pulse. *Physical Review Letters*, 74:2002, 1995.
- [16] S. Eliezer. *The Interaction of High-Power Lasers with Plasmas*. Institute of Physics Publishing, 2002.
- [17] H. Hora. Theory of relativistic self-focusing of laser radiation in plasmas. *J. Opt. Soc. Am.*, 65:882, 1975.
- [18] D. M. Gold. Direct measurement of prepulse suppression by use of a plasma shutter. *Optics Letters*, 19:2006, 1994.
- [19] G. Doumy, F. Quere, O. Gobert, M. Perdrix, P. Martin, P. Audebert, J. C. Gauthier, J. P. Geindre, and T. Wittmann. Complete characterization of a plasma mirror for the production of high-contrast ultraintense laser pulses. *Physical Review E*, 69:026402, 2004.
- [20] B. Dromey, S. Kar, M. Zepf, and P. Foster. The plasma mirror - a sub-picosecond optical switch for ultrahigh power lasers. *Review of Scientific Instruments*, 75:645, 2004.

- [21] A. A. Andreev, S. Steinke, T. Sokollik, M. Schnurer, S. Ter Avetsiyan, K. Y. Platonov, and P. V. Nickles. Optimal ion acceleration from ultrathin foils irradiated by a profiled laser pulse of relativistic intensity. *Physics of Plasmas*, 16:013103, 2009.
- [22] S. Gordienko, A. Pukhov, O. Shorokhov, and T. Baeva. Relativistic doppler effect: Universal spectra and zeptosecond pulses. *Physical Review Letters*, 93:115002, 2004.
- [23] T. Baeva, S. Gordienko, and A. Pukhov. Theory of high-order harmonic generation in relativistic laser interaction with overdense plasma. *Physical Review E*, 74:046404, 2006.
- [24] G. D. Tsakiris, K. Eidmann, J. Meyer-ter Vehn, and F. Krausz. Route to intense single attosecond pulses. *New Journal of Physics*, 8:19, 2006.
- [25] B. Quesnel and P. Mora. Theory and simulation of the interaction of ultra-intense laser pulses with electrons in vacuum. *Physical Review E*, 58:3719, 1998.
- [26] C. I. Moore, J. P. Knauer, and D. D. Meyerhofer. Observation of the transition from thomson to compton scattering in multiphoton interactions with low-energy electrons. *Physical Review Letters*, 74:2439, 1995.
- [27] W. L. Kruer. *The Physics of Laser Plasma Interactions*. 2003.
- [28] D. W. Forslund, J. M. Kindel, and K. Lee. Theory of hot-electron spectra at high laser intensity. *Physical Review Letters*, 39:284, 1977.
- [29] F. Brunel. Not-so-resonant, resonant absorption. *Physical Review Letters*, 59:52, 1987.
- [30] S. C. Wilks, W. L. Kruer, M. Tabak, and A. B. Langdon. Absorption of ultra-intense laser pulses. *Physical Review Letters*, 69:1383, 1992.
- [31] M. P. Kalashnikov, P. V. Nickles, Th. Schlegel, M. Schnuerer, F. Billhardt, I. Will, W. Sandner, and N. N. Demchenko. Dynamics of laser-plasma interaction at  $10^{18}$  W/cm<sup>2</sup>. *Physical Review Letters*, 73:260, 1994.
- [32] W. L. Kruer and Kent Estabrook. J x b heating by very intense laser light. *Physics of Fluids*, 28:430, 1985.
- [33] T. Esirkepov, M. Borghesi, S. V. Bulanov, G. Mourou, and T. Tajima. Highly efficient relativistic-ion generation in the laser-piston regime. *Physical Review Letters*, 92:175003, 2004.

- [34] T. Esirkepov, M. Yamagiwa, and T. Tajima. Laser ion-acceleration scaling laws seen in multiparametric particle-in-cell simulations. *Physical Review Letters*, 96:105001, 2006.
- [35] A. Macchi, F. Cattani, T. V. Liseykina, and F. Cornolti. Laser acceleration of ion bunches at the front surface of overdense plasmas. *Physical Review Letters*, 94:165003, 2005.
- [36] S. C. Wilks, A. B. Langdon, T. E. Cowan, M. Roth, M. Singh, S. Hatchett, M. H. Key, D. Pennington, A. MacKinnon, and R. A. Snavely. Energetic proton generation in ultra-intense laser-solid interactions. *Physics of Plasmas*, 8:542, 2001.
- [37] P. Mora. Plasma expansion into a vacuum. *Physical Review Letters*, 90:185002, 2003.
- [38] B. J. Albright, L. Yin, B. M. Hegelich, Kevin J. Bowers, T. J. T. Kwan, and J. C. Fernández. Theory of laser acceleration of light-ion beams from interaction of ultrahigh-intensity lasers with layered targets. *Physical Review Letters*, 97:115002, 2006.
- [39] J. Fuchs, P. Antici, E. D’Humieres, E. Lefebvre, M. Borghesi, E. Brambrink, C. A. Cecchetti, M. Kaluza, V. Malka, M. Manclossi, S. Meyroneinc, P. Mora, J. Schreiber, T. Toncian, H. Pepin, and R. Audebert. Laser-driven proton scaling laws and new paths towards energy increase. *Nature Physics*, 2:48, 2006.
- [40] J. Schreiber, F. Bell, F. Gruener, U. Schramm, M. Geissler, M. Schnuerer, S. Ter-Avetisyan, B. M. Hegelich, J. Cobble, E. Brambrink, J. Fuchs, P. Audebert, and D. Habs. Analytical model for ion acceleration by high-intensity laser pulses. *Physical Review Letters*, 97:045005, 2006.
- [41] G. Malka, J. Fuchs, F. Amiranoff, S. D. Baton, R. Gaillard, J. L. Miquel, H. Pépin, C. Rousseaux, G. Bonnaud, M. Busquet, and L. Lours. Suprathermal electron generation and channel formation by an ultrarelativistic laser pulse in an underdense preformed plasma. *Physical Review Letters*, 79:2053, 1997.
- [42] K. B. Wharton, S. P. Hatchett, S. C. Wilks, M. H. Key, J. D. Moody, V. Yanovsky, A. A. Offenberger, B. A. Hammel, M. D. Perry, and C. Joshi. Experimental measurements of hot electrons generated by ultraintense ( $>10^{19}$  W/cm<sup>2</sup>) laser-plasma interactions on solid-density targets. *Physical Review Letters*, 81:822, 1998.

- [43] F. Amiranoff. Fast electron production in ultra-short high-intensity laser-plasma interaction and its consequences. *Measurement Science and Technology*, 12:1795, 2001.
- [44] S. P. Hatchett, C. G. Brown, T. E. Cowan, E. A. Henry, J. S. Johnson, M. H. Key, J. A. Koch, A. B. Langdon, B. F. Lasinski, R. W. Lee, A. J. Mackinnon, D. M. Pennington, M. D. Perry, T. W. Phillips, M. Roth, T. C. Sangster, M. S. Singh, R. A. Snavely, M. A. Stoyer, S. C. Wilks, and K. Yasuike. Electron, photon, and ion beams from the relativistic interaction of petawatt laser pulses with solid targets. *Physics of Plasmas*, 7:2076, 2000.
- [45] E. L. Clark, K. Krushelnick, M. Zepf, F. N. Beg, M. Tatarakis, A. Machacek, M. I. K. Santala, I. Watts, P. A. Norreys, and A. E. Dangor. Energetic heavy-ion and proton generation from ultraintense laser-plasma interactions with solids. *Physical Review Letters*, 85:1654, 2000.
- [46] A. Maksimchuk, S. Gu, K. Flippo, D. Umstadter, and V. Y. Bychenkov. Forward ion acceleration in thin films driven by a high-intensity laser. *Physical Review Letters*, 84:4108, 2000.
- [47] M. Allen, P. K. Patel, A. Mackinnon, D. Price, S. Wilks, and E. Morse. Direct experimental evidence of back-surface ion acceleration from laser-irradiated gold foils. *Physical Review Letters*, 93:265004, 2004.
- [48] M. Borghesi, A. J. Mackinnon, D. H. Campbell, D. G. Hicks, S. Kar, P. K. Patel, D. Price, L. Romagnani, A. Schiavi, and O. Willi. Multi-mev proton source investigations in ultraintense laser-foil interactions. *Physical Review Letters*, 92:055003, 2004.
- [49] T. E. Cowan, J. Fuchs, H. Ruhl, A. Kemp, P. Audebert, M. Roth, R. Stephens, I. Barton, A. Blazevic, E. Brambrink, J. Cobble, J. Fernández, J. C. Gauthier, M. Geissler, M. Hegelich, J. Kaae, S. Karsch, G. P. Le Sage, S. Letzring, M. Manclossi, S. Meyroneinc, A. Newkirk, H. Pépin, and N. Renard-LeGalloudec. Ultralow emittance, multi-mev proton beams from a laser virtual-cathode plasma accelerator. *Physical Review Letters*, 92:204801, 2004.
- [50] J. Schreiber, M. Kaluza, F. Gruner, U. Schramm, B. M. Hegelich, J. Cobble, M. Geissler, E. Brambrink, J. Fuchs, P. Audebert, D. Habs, and K. Witte. Source-size measurements and charge distributions of ions accelerated from thin foils irradiated by high-intensity laser pulses. *Applied Physics B-Lasers and Optics*, 79:1041, 2004.

- [51] T. Sokollik, M. Schnuerer, S. Ter-Avetisyan, P. V. Nickles, E. Risse, M. Kalashnikov, W. Sandner, G. Priebe, M. Amin, T. Toncian, O. Willi, and A. A. Andreev. Transient electric fields in laser plasmas observed by proton streak deflectometry. *Applied Physics Letters*, 92:091503, 2008.
- [52] M. Hegelich, S. Karsch, G. Pretzler, D. Habs, K. Witte, W. Guenther, M. Allen, A. Blazevic, J. Fuchs, J. C. Gauthier, M. Geissel, P. Audebert, T. Cowan, and M. Roth. Mev ion jets from short-pulse-laser interaction with thin foils. *Physical Review Letters*, 89:085002, 2002.
- [53] P. McKenna, K. W. D. Ledingham, J. M. Yang, L. Robson, T. McCanny, S. Shimizu, R. J. Clarke, D. Neely, K. Spohr, R. Chapman, R. P. Singhal, K. Krushelnick, M. S. Wei, and P. A. Norreys. Characterization of proton and heavier ion acceleration in ultrahigh-intensity laser interactions with heated target foils. *Physical Review E*, 70:036405, 2004.
- [54] B. M. Hegelich, B. J. Albright, J. Cobble, K. Flippo, S. Letzring, M. Paffett, H. Ruhl, J. Schreiber, R. K. Schulze, and J. C. Fernandez. Laser acceleration of quasi-monoenergetic mev ion beams. *Nature*, 439:441, 2006.
- [55] S. Ter-Avetisyan, M. Schnuerer, P. V. Nickles, M. Kalashnikov, E. Risse, T. Sokollik, W. Sandner, A. Andreev, and V. Tikhonchuk. Quasimonoenergetic deuteron bursts produced by ultraintense laser pulses. *Physical Review Letters*, 96:145006, 2006.
- [56] T. Sokollik, M. Schnuerer, S. Steinke, P. V. Nickles, W. Sandner, M. Amin, T. Toncian, O. Willi, and A. A. Andreev. Directional laser-driven ion acceleration from microspheres. *Physical Review Letters*, 103:135003, 2009.
- [57] T. Sokollik, T. Paasch-Colberg, K. Gorling, U. Eichmann, M. Schnuerer, S. Steinke, P. V. Nickles, A. A. Andreev, and W. Sandner. Laser-driven ion acceleration using isolated mass-limited spheres. *New Journal of Physics*, 12:113013, 2010.
- [58] H. Schwoerer, S. Pfotenhauer, O. Jackel, K. U. Amthor, B. Liesfeld, W. Ziegler, R. Sauerbrey, K. W. D. Ledingham, and T. Esirkepov. Laser-plasma acceleration of quasi-monoenergetic protons from microstructured targets. *Nature*, 439:445, 2006.
- [59] S. M. Pfotenhauer, O. Jackel, A. Sachtleben, J. Polz, W. Ziegler, H. P. Schlenvoigt, K. U. Amthor, M. C. Kaluza, K. W. D. Ledingham, R. Sauerbrey, P. Gibbon, A. P. L. Robinson, and H. Schwoerer. Spectral shaping of laser generated proton beams. *New Journal of Physics*, 10:033034, 2008.

- [60] M. Murakami and M. M. Basko. Self-similar expansion of finite-size non-quasi-neutral plasmas into vacuum: Relation to the problem of ion acceleration. *Physics of Plasmas*, 13:012105, 2006.
- [61] A. A. Andreev, A. Lévy, T. Ceccotti, C. Thaury, K. Platonov, R. A. Loch, and Ph Martin. Fast-ion energy-flux enhancement from ultrathin foils irradiated by intense and high-contrast short laser pulses. *Physical Review Letters*, 101:155002, 2008.
- [62] Y. Sentoku, H. Ruhl, K. Mima, R. Kodama, K. A. Tanaka, and Y. Kishimoto. Plasma jet formation and magnetic-field generation in the intense laser plasma under oblique incidence. *Physics of Plasmas*, 6:2855, 1999.
- [63] X. Zhang, B. Shen, X. Li, Z. Jin, and F. Wang. Multistaged acceleration of ions by circularly polarized laser pulse: Monoenergetic ion beam generation. *Physics of Plasmas*, 14:073101, 2007.
- [64] O. Klimo, J. Psikal, J. Limpouch, and V. T. Tikhonchuk. Monoenergetic ion beams from ultrathin foils irradiated by ultrahigh-contrast circularly polarized laser pulses. *Physical Review Special Topics-Accelerators and Beams*, 11:031301, 2008.
- [65] A. P. L. Robinson, M. Zepf, S. Kar, R. G. Evans, and C. Bellei. Radiation pressure acceleration of thin foils with circularly polarized laser pulses. *New Journal of Physics*, 10:013021, 2008.
- [66] X. Q. Yan, C. Lin, Z. M. Sheng, Z. Y. Guo, B. C. Liu, Y. R. Lu, J. X. Fang, and J. E. Chen. Generating high-current monoenergetic proton beams by a circularly polarized laser pulse in the phase-stable acceleration regime. *Physical Review Letters*, 100:135003, 2008.
- [67] B. Qiao, M. Zepf, M. Borghesi, and M. Geissler. Stable gev ion-beam acceleration from thin foils by circularly polarized laser pulses. *Physical Review Letters*, 102:145002, 2009.
- [68] A. Macchi, S. Veghini, and F. Pegoraro. "light sail" acceleration reexamined. *Physical Review Letters*, 103:085003, 2009.
- [69] A. Macchi, S. Veghini, T. V. Liseykina, and F. Pegoraro. Radiation pressure acceleration of ultrathin foils. *New Journal of Physics*, 12:045013, 2010.
- [70] G. Marx. Interstellar vehicle propelled by terrestrial laser beam. *Nature*, 211:22, 1966.

- [71] D. Kiefer, A. Henig, D. Jung, D. C. Gautier, K. A. Flippo, S. A. Gaillard, S. Letzring, R. P. Johnson, R. C. Shah, T. Shimada, J. C. Fernández, V. Kh Liechtenstein, J. Schreiber, B. M. Hegelich, and D. Habs. First observation of quasi-monoenergetic electron bunches driven out of ultra-thin diamond-like carbon (DLC) foils. *The European Physical Journal D - Atomic, Molecular, Optical and Plasma Physics*, 55:427, 2009.
- [72] J. L. Redding. Interstellar vehicle propelled by terrestrial laser beam. *Nature*, 213:588, 1967.
- [73] J. F. L. Simmons and C. R. McInnes. Was marx right? or how efficient are laser driven interstellar spacecraft? *American Journal of Physics*, 61:205, 1993.
- [74] V. A. Vshivkov, N. M. Naumova, F. Pegoraro, and S. V. Bulanov. Nonlinear electrodynamics of the interaction of ultra-intense laser pulses with a thin foil. *Physics of Plasmas*, 5:2727, 1998.
- [75] N. H. Burnett, H. A. Baldis, M. C. Richardson, and G. D. Enright. Harmonic generation in CO<sub>2</sub> laser target interaction. *Applied Physics Letters*, 31:172, 1977.
- [76] R. L. Carman, D. W. Forslund, and J. M. Kindel. Visible harmonic emission as a way of measuring profile steepening. *Physical Review Letters*, 46:29, 1981.
- [77] B. Bezzerides, R. D. Jones, and D. W. Forslund. Plasma mechanism for ultraviolet harmonic radiation due to intense CO<sub>2</sub> light. *Physical Review Letters*, 49:202, 1982.
- [78] U. Teubner, K. Eidmann, U. Wagner, U. Andiel, F. Pisani, G. D. Tsakiris, K. Witte, J. Meyer-ter Vehn, T. Schlegel, and E. Foerster. Harmonic emission from the rear side of thin overdense foils irradiated with intense ultrashort laser pulses. *Physical Review Letters*, 92:185001, 2004.
- [79] F. Quéré, C. Thaury, P. Monot, S. Dobosz, Ph Martin, J. P. Geindre, and P. Audebert. Coherent wake emission of high-order harmonics from overdense plasmas. *Physical Review Letters*, 96:125004, 2006.
- [80] S. V. Bulanov, N. M. Naumova, and F. Pegoraro. Interaction of an ultrashort, relativistically strong laser pulse with an overdense plasma. *Physics of Plasmas*, 1:745, 1994.



- [81] B. Dromey, S. Kar, C. Bellei, D. C. Carroll, R. J. Clarke, J. S. Green, S. Kneip, K. Markey, S. R. Nagel, P. T. Simpson, L. Willingale, P. McKenna, D. Neely, Z. Najmudin, K. Krushelnick, P. A. Norreys, and M. Zepf. Bright multi-keV harmonic generation from relativistically oscillating plasma surfaces. *Physical Review Letters*, 99:085001, 2007.
- [82] A. Tarasevitch, K. Lobov, C. Wuensche, and D. von der Linde. Transition to the relativistic regime in high order harmonic generation. *Physical Review Letters*, 98:103902, 2007.
- [83] U. Teubner and P. Gibbon. High-order harmonics from laser-irradiated plasma surfaces. *Reviews of Modern Physics*, 81:445, 2009.
- [84] Y. Nomura, R. Hoerlein, P. Tzallas, B. Dromey, S. Rykovanov, Z. Major, J. Osterhoff, S. Karsch, L. Veisz, M. Zepf, D. Charalambidis, F. Krausz, and G. D. Tsakiris. Attosecond phase locking of harmonics emitted from laser-produced plasmas. *Nature Physics*, 5:124, 2009.
- [85] K. Krushelnick, E. L. Clark, F. N. Beg, A. E. Dangor, Z. Najmudin, P. A. Norreys, M. Wei, and M. Zepf. High intensity laser-plasma sources of ions-physics and future applications. *Plasma Physics and Controlled Fusion*, 47:B451, 2005.
- [86] H. George, F. Quere, C. Thaury, G. Bonnaud, and P. Martin. Mechanisms of forward laser harmonic emission from thin overdense plasmas. *New Journal of Physics*, 11:113028, 2009.
- [87] M. Tatarakis, I. Watts, F. N. Beg, E. L. Clark, A. E. Dangor, A. Gopal, M. G. Haines, P. A. Norreys, U. Wagner, M. S. Wei, M. Zepf, and K. Krushelnick. Laser technology: Measuring huge magnetic fields. *Nature*, 415:280, 2002.
- [88] B. Dromey, D. Adams, R. Horlein, Y. Nomura, S. G. Rykovanov, D. C. Carroll, P. S. Foster, S. Kar, K. Markey, P. McKenna, D. Neely, M. Geissler, G. D. Tsakiris, and M. Zepf. Diffraction-limited performance and focusing of high harmonics from relativistic plasmas. *Nat Phys*, 5:146, 2009.
- [89] H. C. Barr, T. J. M. Boyd, G. A. Gardner, and R. Rankin. Inverse resonance absorption in an inhomogeneous magnetized plasma. *Physics of Fluids*, 28:16, 1985.
- [90] Z. M. Sheng, K. Mima, J. Zhang, and H. Sanuki. Emission of electromagnetic pulses from laser wakefields through linear mode conversion. *Physical Review Letters*, 94:095003, 2005.

- [91] C. Thaury, F. Quere, J. P. Geindre, A. Lévy, T. Ceccotti, P. Monot, M. Bougeard, F. Reau, P. D'Oliveira, P. Audebert, R. Marjoribanks, and P. H. Martin. Plasma mirrors for ultrahigh-intensity optics. *Nature Physics*, 3:424, 2007.
- [92] R. Hoerlein, Y. Nomura, J. Osterhoff, Z. Major, S. Karsch, F. Krausz, and G. D. Tsakiris. High harmonics from solid surfaces as a source of ultra-bright xuv radiation for experiments. *Plasma Physics and Controlled Fusion*, 50:124002, 2008.
- [93] K. Varju, Y. Mairesse, B. Carre, M. B. Gaarde, P. Johnsson, S. Kazamias, R. Lopez-Martens, J. Mauritsson, K. J. Schafer, P. H. Balcou, A. L'Huillier, and P. Salieres. Frequency chirp of harmonic and attosecond pulses. *Journal of Modern Optics*, 52:379, 2005.
- [94] C. Iaconis and I. A. Walmsley. Spectral phase interferometry for direct electric-field reconstruction of ultrashort optical pulses. *Opt. Lett.*, 23:792, 1998.
- [95] S. Luan, M. H. R. Hutchinson, R. A. Smith, and F. Zhou. High dynamic-range 3rd-order correlation-measurement of picosecond laser-pulse shapes. *Measurement Science and Technology*, 4:1426, 1993.
- [96] A. Lévy, T. Ceccotti, P. D'Oliveira, F. Reau, M. Perdrix, F. Quere, P. Monot, M. Bougeard, H. Lagarde, P. Martin, J. P. Geindre, and P. Audebert. Double plasma mirror for ultrahigh temporal contrast ultraintense laser pulses. *Optics Letters*, 32:310, 2007.
- [97] A. Stingl, C. Spielmann, F. Krausz, and R. Szipoecs. Generation of 11-fs pulses from a ti:sapphire laser without the use of prisms. *Opt. Lett.*, 19:204, 1994.
- [98] G. Cheriaux, P. Rousseau, F. Salin, J. P. Chambaret, Barry Walker, and L. F. Dimauro. Aberration-free stretcher design for ultrashort-pulse amplification. *Opt. Lett.*, 21:414, 1996.
- [99] M. Nantel, G. Ma, S. Gu, C. Y. Cote, J. Itatani, and D. Umstadter. Pressure ionization and line merging in strongly coupled plasmas produced by 100-fs laser pulses. *Physical Review Letters*, 80:4442, 1998.
- [100] J. Itatani, J. Faure, M. Nantel, G. Mourou, and S. Watanabe. Suppression of the amplified spontaneous emission in chirped-pulse-amplification lasers by clean high-energy seed-pulse injection. *Optics Communications*, 148:70, 1998.

- [101] M. P. Kalashnikov, E. Risse, H. Schonagel, A. Husakou, J. Herrmann, and W. Sandner. Characterization of a nonlinear filter for the front-end of a high contrast double-CPA Ti : sapphire laser. *Optics Express*, 12:5088, 2004.
- [102] A. Jullien, O. Albert, F. Burgy, G. Hamoniaux, L. P. Rousseau, J. P. Chambaret, F. Auge-Rochereau, G. Cheriaux, J. Etchepare, N. Minkovski, and S. M. Saltiel.  $10^{-10}$  temporal contrast for femtosecond ultraintense lasers by cross-polarized wave generation. *Optics Letters*, 30:920, 2005.
- [103] A. Dubietis, G. Jonusauskas, and A. Piskarskas. Powerful femtosecond pulse generation by chirped and stretched pulse parametric amplification in bbo crystal. *Optics Communications*, 88:437, 1992.
- [104] H. C. Kapteyn, M. M. Murnane, A. Szoke, and R. W. Falcone. Prepulse energy suppression for high-energy ultrashort pulses using self-induced plasma shuttering. *Optics Letters*, 16:490, 1991.
- [105] S. Backus, H. C. Kapteyn, M. M. Murnane, D. M. Gold, H. Nathel, and W. White. Prepulse suppression for high-energy ultrashort pulses using self-induced plasma shuttering from a fluid target. *Optics Letters*, 18:134, 1993.
- [106] T. Wittmann, J. P. Geindre, P. Audebert, R. S. Marjoribanks, J. P. Rousseau, F. Burgy, D. Douillet, T. Lefrou, K. T. Phuoc, and J. P. Chambaret. Towards ultrahigh-contrast ultraintense laser pulses-complete characterization of a double plasma-mirror pulse cleaner. *Review of Scientific Instruments*, 77:083109, 2006.
- [107] Y. Nomura, L. Veisz, K. Schmid, T. Wittmann, J. Wild, and F. Krausz. Time-resolved reflectivity measurements on a plasma mirror with few-cycle laser pulses. *New Journal of Physics*, 9:9, 2007.
- [108] J. Borchers. private communications. *LENS-Optics GmbH, Buergermeister-Neumeyr-Strasse 7, 85391 Allershausen*.
- [109] S. Steinke. Entwicklung eines Doppel-Plasmaspiegels zur Erzeugung hochenergetischer Ionen mit ultra-dünnen Targets. [http://edocs.fu-berlin.de/docs/receive/FUDOCs\\_document\\_000000000603](http://edocs.fu-berlin.de/docs/receive/FUDOCs_document_000000000603), 2007.
- [110] N. Kent Moncur. Plasma spatial filter. *Appl. Opt.*, 16:1449, 1977.
- [111] J. J. Thomson. Rays of positive electricity. *Philosophical Magazine*, 6:225, 1911.

- [112] S. Ter-Avetisyan, M. Schnuerer, and P. V. Nickles. Time resolved corpuscular diagnostics of plasmas produced with high-intensity femtosecond laser pulses. *Journal of Physics D-Applied Physics*, 38:863, 2005.
- [113] R. F. Schneider, C. M. Luo, and M. J. Rhee. Resolution of the thomson spectrometer. *Journal of Applied Physics*, 57:1, 1985.
- [114] M. Born and E. Wolf. *Pinciples of optics*. Cambridge University Press, 7 edition, 1999.
- [115] T. Namioka. Theory of the concave grating. iii. seya-namioka monochromator. *J. Opt. Soc. Am.*, 49:951, 1959.
- [116] A. Henig and J. Schreiber. private communications. *Max-Planck-Institut für Quantenoptik, 85748 Garching, Germany*.
- [117] A. J. Mackinnon, Y. Sentoku, P. K. Patel, D. W. Price, S. Hatchett, M. H. Key, C. Andersen, R. Snavely, and R. R. Freeman. Enhancement of proton acceleration by hot-electron recirculation in thin foils irradiated by ultraintense laser pulses. *Physical Review Letters*, 88:215006, 2002.
- [118] D. Neely, P. Foster, A. Robinson, F. Lindau, O. Lundh, A. Persson, C. G. Wahlstrom, and P. McKenna. Enhanced proton beams from ultrathin targets driven by high contrast laser pulses. *Applied Physics Letters*, 89:021502, 2006.
- [119] T. Ceccotti, A. Levy, H. Popescu, F. Reau, P. D'Oliveira, P. Monot, J. P. Geindre, E. Lefebvre, and P. Martin. Proton acceleration with high-intensity ultrahigh-contrast laser pulses. *Physical Review Letters*, 99:185002, 2007.
- [120] E. d'Humieres, E. Lefebvre, L. Gremillet, and V. Malka. Proton acceleration mechanisms in high-intensity laser interaction with thin foils. *Physics of Plasmas*, 12:062704, 2005.
- [121] L. Yin, B. J. Albright, B. M. Hegelich, and J. C. Fernandez. GeV laser ion acceleration from ultrathin targets: The laser break-out afterburner. *Laser and Particle Beams*, 24:291, 2006.
- [122] B. J. Albright, L. Yin, Kevin J. Bowers, B. M. Hegelich, K. A. Flippo, T. J. T. Kwan, and J. C. Fernandez. Relativistic buneman instability in the laser breakout afterburner. *Physics of Plasmas*, 14:094502, 2007.
- [123] X. Q. Yan, T. Tajima, M. Hegelich, L. Yin, and D. Habs. Theory of laser ion acceleration from a foil target of nanometer thickness. *Applied Physics B: Lasers and Optics*, 98, 2009.

- [124] L. L. Ji, B. F. Shen, X. M. Zhang, F. C. Wang, Z. Y. Jin, C. Q. Xia, M. Wen, W. P. Wang, J. C. Xu, and M. Y. Yu. Generating quasi-single-cycle relativistic laser pulses by laser-foil interaction. *Physical Review Letters*, 103:215005, 2009.
- [125] A. Henig, D. Kiefer, K. Markey, D. C. Gautier, K. A. Flippo, S. Letzring, R. P. Johnson, T. Shimada, L. Yin, B. J. Albright, K. J. Bowers, J. C. Fernandez, S. G. Rykovanov, H. C. Wu, M. Zepf, D. Jung, V. Kh Liechtenstein, J. Schreiber, D. Habs, and B. M. Hegelich. Enhanced laser-driven ion acceleration in the relativistic transparency regime. *Physical Review Letters*, 103:045002, 2009.
- [126] F. Nuernberg, M. Schollmeier, E. Brambrink, A. Blazevic, D. C. Carroll, K. Flippo, D. C. Gautier, M. Geissel, K. Harres, B. M. Hegelich, O. Lundh, K. Markey, P. McKenna, D. Neely, J. Schreiber, and M. Roth. Radiochromic film imaging spectroscopy of laser-accelerated proton beams. *Review of Scientific Instruments*, 80:033301, 2009.
- [127] T. Kluge, W. Enghardt, S. D. Kraft, U. Schramm, Y. Sentoku, K. Zeil, T. E. Cowan, R. Sauerbrey, and M. Bussmann. Efficient laser-ion acceleration from closely stacked ultrathin foils. *Physical Review E*, 82:016405, 2010.
- [128] S. G. Rykovanov, J. Schreiber, J. Meyer-Ter-Vehn, C. Bellei, A. Henig, H. C. Wu, and M. Geissler. Ion acceleration with ultra-thin foils using elliptically polarized laser pulses. *New Journal of Physics*, 10:113005, 2008.
- [129] T. V. Liseykina, M. Borghesi, A. Macchi, and S. Tuveri. Radiation pressure acceleration by ultraintense laser pulses. *Plasma Physics and Controlled Fusion*, 50:124033, 2008.
- [130] M. Chen, A. Pukhov, Z. M. Sheng, and X. Q. Yan. Laser mode effects on the ion acceleration during circularly polarized laser pulse interaction with foil targets. *Physics of Plasmas*, 15:113103, 2008.
- [131] M. Chen, A. Pukhov, T. P. Yu, and Z. M. Sheng. Enhanced collimated gev monoenergetic ion acceleration from a shaped foil target irradiated by a circularly polarized laser pulse. *Physical Review Letters*, 103:024801, 2009.
- [132] S. G. Rykovanov, M. Geissler, J. Meyer-Ter-Vehn, and G. D. Tsakiris. Intense single attosecond pulses from surface harmonics using the polarization gating technique. *New Journal of Physics*, 10:025025, 2008.



# Acknowledgments

At this point I would like to thank all the people who have contributed to this work. Without your support, enthusiasm and friendship this work would have been impossible. Especially, the following people shall be recognized:

- Prof. Dr. W. Sander for supervising this work and the opportunity to work in this excellent research group.
- Prof. Dr. O. Willi for being the second referee of this thesis and for his wisdom as spokesman of TR18.
- Prof. Dr. P. V. Nickles for his visionary thoughts that paved the way towards the realization of this work from the very beginning and for the uncountable discussions.
- Dr. M. Schnürer for his unfailing support and mentoring with an outstanding competence.
- Dr. T. Sokollik for much more than his friendly support and many fruitful discussions.
- L. Ehrentraut and Dr. G. Priebe for peak performance.
- Prof. Dr. A. A. Andreev for patiently supporting me theoretically.
- Prof. Dr. D. Habs, Prof. Dr. T. Tajima, Dr. A. Henig, Dr. J. Schreiber, Dr. R. Hörlein, D. Kiefer for the very fruitful cooperation.
- All other administrative and technical employers: P. Friedrich, S. Szlapka, B. Becker, G. Kommol, J. Meißner, J. Gläsel and D. Rohloff.
- Last but not least, my family for their personal support during all the years and especially Marzena for backing me up all the time, no matter how many nights I spend in the lab.